STRONG-FIELD NUMERICAL RELATIVITY IN THE ERA OF GRAVITATIONAL WAVE ASTRONOMY

A Dissertation
Presented to
The Academic Faculty

By

Deborah Lynn Ferguson

In Partial Fulfillment
of the Requirements for the Degree
Doctor of Philosophy in the
School of Physics

Georgia Institute of Technology

December 2020

STRONG-FIELD NUMERICAL RELATIVITY IN THE ERA OF GRAVITATIONAL WAVE ASTRONOMY

Approved by:

Dr. Deirdre Shoemaker, Advisor
School of Physics
Georgia Institute of Technology

Dr. Tamara Bogdanović
School of Physics
Georgia Institute of Technology

Dr. Laura Cadonati
School of Physics
Georgia Institute of Technology

Dr. Pablo Laguna
Department of Physics
University of Texas at Austin

Dr. John Wise
School of Physics
Georgia Institute of Technology

Date Approved: October 13, 2020

There is a theory which states that if ever anyone discovers exactly what the Universe is for and why it is here, it will instantly disappear and be replaced by something even more bizarre and inexplicable.

Douglas Adams

ACKNOWLEDGEMENTS

This dissertation would not have been possible without the tremendous mentorship of my advisor, Deirdre Shoemaker. After my first visit to Georgia Tech, I knew I wanted to work with her; her enthusiasm as well as her remarkable impact on the field were inspiring. Without her expertise and encouragement, none of this research would have reached fruition.

I would also like to thank Pablo Laguna who has served as a sort of informal advisor. Pablo has been an unending source of questions to investigate, each more interesting than the last. Significant portions of this thesis began as conversations with Pablo.

I would like to thank Laura Cadonati, who encouraged me to expand my knowledge of the workings of LIGO. This has been essential for understanding the interplay between numerical relativity and gravitational wave detection. I also greatly appreciate the feedback and advice given by Tamara Bogdanović and John Wise.

Since I joined the group with no previous numerical relativity experience, Karan Jani, Juan Calderón Bustillo, Miguel Gracia, and Bhavesh Khamesra were pivotal in my onboarding. They taught me all the basics of numerical relativity and how to run the MAYA code. Chris Evans and Bhavesh Khamesra have been great partners throughout multiple projects, working with me to tackle questions from multiple perspectives. Additionally, without James Clark and Sudarshan Ghonge, I would have been at a loss when it came to working with LIGO data and tools and particularly BayesWave.

I am also sincerely grateful for Susan Gardner and Christopher Crawford whose guidance and support throughout my undergraduate studies helped me reach where I am today. Christopher Crawford gave me my first experience in research and helped prepare me for graduate school both as a professor and as a mentor. Susan Gardner provided me with the opportunity to conduct research in astrophysics, enabling me to publish my first paper.

The work in this thesis is supported by NSF grants PHY-1809572, PHY-1505824, PHY-

1839819 and NASA grant 8ONSSC19KO322. Simulations and computations were performed using resources provided by XSEDE TG-PHY120016, PACE at Georgia Tech, and LIGO supported by NSF grants PHY-0757058 and PHY-0823459.

TABLE OF CONTENTS

LIST OF TABLES

LIST OF FIGURES

SUMMARY

The detection of gravitational waves (GWs) has ushered in the era of GW astronomy, providing the strongest test to date of Einstein's theory of general relativity (GR). The detection and interpretation of these signals would be impossible without a strong understanding of the theory that best governs them, Einstein's theory of GR. Due to the complex, nonlinear nature of Einstein's equations, predicting the behavior of all but the simplest of cases in GR must be solved numerically. This can be accomplished with numerical relativity (NR), which solves Einstein's equations to simulate merging compact binary systems. From these simulations, we can obtain the predicted gravitational radiation. With the ability to both model and detect the GWs emitted by compact binary mergers, we now have a new way to observe and understand the universe.

The subject of this dissertation falls at this intersection between theory and observation, determining how best to use NR in order to maximize the scientific gain from each detection. I tackle this from two main perspectives: 1) how can we use NR to better understand the parameters of the merging systems currently being regularly observed, and 2) how can we best prepare NR for the GW observations of the future?

Chapter 1, "Introduction: Gravitational Wave Detection", provides an introduction to the detection of GWs. I begin with a brief description of GWs and the current and future observatories used to detect them. This is followed by a description of the search pipelines and parameter estimation techniques used to characterize the GWs and the sources that produce them.

Chapter 2, "Introduction: Numerical Relativity", introduces NR, beginning with a summary of the 3+1 decomposition of Einstein's equations and then describing the specific numerical techniques utilized to generate stable, accurate binary black hole (BBH) simulations. I then describe how to use the MAYA code to perform a BBH simulation, obtain the GWs, and prepare it for use with detector data.

In Chapter 3, “Infrastructure”, I describe the work I have done to improve our NR catalog and the infrastructure around it. A large part of my role as a member of the LIGO and Virgo Collaboration (LVC) has been to generate and maintain a catalog of NR waveforms to be used by the LVC community for data analysis, construction of models, etc. In this chapter, I also describe the development of several data analysis tools to be used with NR waveforms as well as with detector data. In addition to the work described in this dissertation, I also studied the evolution of apparent horizons (AHs) and marginally outer trapped surfaces (MOTSs) present during the merger of BBH systems. This chapter describes the modifications I made to the horizon finder in order to make this work possible. My study of AHs also led to the development of a visualization tool which is described in this chapter.

Chapter 4, “Predicting Remnant Spin”, seeks to answer the first key question of this dissertation, how we can use NR to better understand the parameters of BBH systems currently being observed. I describe a technique to predict the spin of the remnant black hole (BH) using only the information available from the GW during merger. Since the merger is the loudest part of a BBH coalescence, this gives a way of more accurately characterizing the remnant BH when very little inspiral is observed. It also provides a new consistency test, verifying whether the values of the remnant spin obtained from each stage of the coalescence are consistent. Until this paper, the final spin could only be computed from the inspiral or the ringdown, but with the introduction of this technique, the spin can now be computed from the merger.

The second question, how to prepare for GW observations of the future, is tackled in several individual but related steps. First, when using template waveforms to detect and understand an observed signal, the template needs to be accurate enough such that any systematic errors don’t impact the analysis. Preparing NR waveforms for use with detectors necessitates having an understanding of how accurate they need to be and whether those accuracies can be achieved with current NR codes. Chapter 5, “Numerical Relativity for Future Detectors”, explores this question for LIGO, ET, and LISA and presents a method to

determine the resolution necessary for finite differencing codes as a function of the signal-to-noise ratio (SNR) of a detection.

Once the necessary accuracy and resolutions are known, waveforms must be generated throughout the parameter space of BBHs. Chapter 6, "Optimizing Numerical Relativity Template Placement", presents methods to optimize how this parameter space is filled in. BBH systems are described by the masses and spin vectors of each BH, as well as the eccentricity of their orbit. This parameter space needs to be densely populated enough so as not to decrease detection rates or mischaracterize signals. However, with the high computational cost of generating waveforms, particularly at the necessary resolutions, these waveforms need to be placed strategically in the parameter space. One way to decrease the necessary coverage is to explore the relative impact of each parameter. A specific question addressed in this dissertation is, as mass ratio increases, how does the impact of the spin of the smaller BH change? Answering this question will prevent unnecessary simulations from being performed.

This can be generalized to the full parameter space using machine learning (ML) to help identify the most beneficial locations in parameter space to place new NR simulations. I present progress on a neural network (NN) which takes in the initial parameters of two binary systems and predicts the match (a measure of similarity) between the two resulting waveforms. By using this model with the initial parameters of proposed simulations, we can identify which would provide the most unique data.

NR and GW detectors have paired to provide us with the opportunity to study Einstein's theory in the strongest gravitational regimes. With future detectors coming online with higher sensitivities, NR will have to continue to improve alongside the detectors. This dissertation addresses how NR can be used and improved to obtain the most scientific return from each GW observation.

Introduction and Background

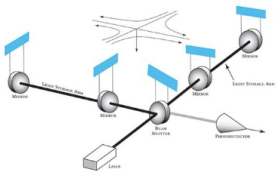

Chapter 1: Gravitational Wave Detection

Overview of current and future GW observatories and detection pipelines

Chapter 2: Numerical Relativity

Introduction to 3+1 decomposition and implementation of numerical relativity

Improving MAYA Infrastructure

Chapter 3: Infrastructure

Description of improvements made to the setup and post-processing of numerical relativity simulations

Utilizing NR to Understand Current Detections

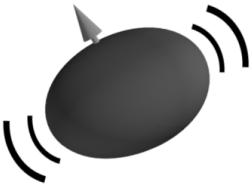

Chapter 4: Predicting Remnant Spin

New method to compute the spin of the remnant black hole from the gravitational radiation during merger

Preparing NR for Detections of the Future

Chapter 5: Numerical Relativity for Future Detectors

Assessment of the preparedness of numerical relativity for next generation observatories

Chapter 6: Optimizing Numerical Relativity Template Placement

Creation of neural network to predict similarity between numerical relativity simulations not yet performed

Conclusions

Chapter 7: Summary and Future Outlook

Overview and future steps

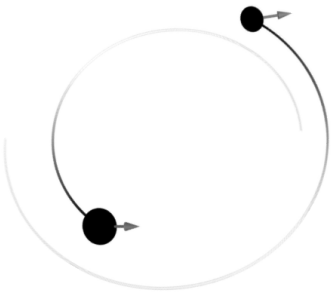

Figure 1: Diagram showing the flow of this dissertation.

CHAPTER 1

INTRODUCTION: GRAVITATIONAL WAVE DETECTION

In 1915, Einstein presented his theory of GR and introduced the world to what is now commonly referred to as Einstein's equations [1]. Until this point, Newton's theory of gravitation had been used to predict the motion of objects through space, and for most scenarios, this was sufficient. However, in areas with strong gravitational fields or when objects moved close to the speed of light, Newton's equations broke down. One of the first times this became apparent was with the precession of Mercury, which Einstein's theory was able to accurately describe.

Then, in 1916, Einstein predicted that the asymmetric acceleration of massive objects would lead to waves that propagate at the speed of light [2]. These GWs are revealed by linearizing the weak-field equations and expressing the spacetime metric as the flat spacetime metric with a perturbation, $g_{\mu\nu} = \eta_{\mu\nu} + h_{\mu\nu}$.

In the early 20th century, there was much debate about whether these waves truly existed. Evidence began to emerge in 1974 when Hulse and Taylor discovered the pulsar PSR B1913+16, a rapidly rotating neutron star (NS) which emits regular pulses of electromagnetic radiation [3]. Given the extreme consistency of these pulses, Hulse and Taylor deduced that the pulsar was in a binary system with another NS and were able to measure its orbital frequency. After observing the binary for decades, they saw that the orbit was decaying in precisely the way one would expect due to the emission of GWs [4, 5].

There have also been many experiments designed to directly observe GWs. Due to the many different types of GW sources, detectors have been designed to be sensitive to different frequency ranges in order to pick up specific types of sources. For example, pulsar timing arrays are sensitive to frequencies of 10^{-9} Hz to 10^{-6} Hz, allowing them to observe a background of supermassive black hole (SMBH) mergers. There are currently three pulsar

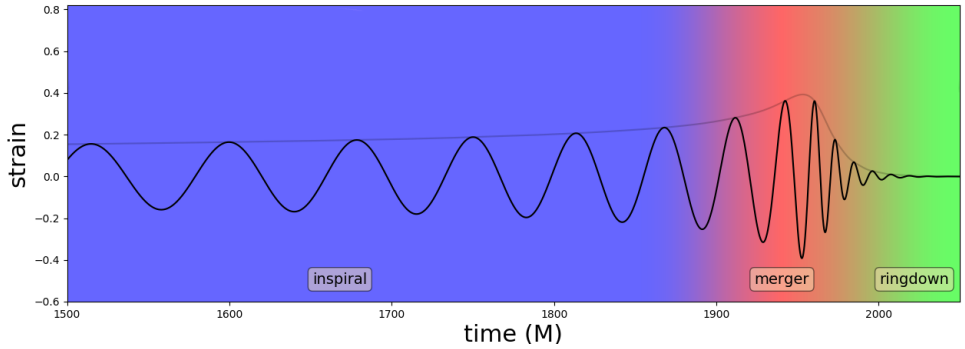

Figure 1.1: Gravitational radiation emitted by a BBH coalesence. The region in blue is the inspiral, red is the merger, and green is the ringdown. The stages are not well defined as shown by the gradients between the regions.

timing arrays gathering data as part of the International Pulsar Timing Array project [6]. We will primarily focus on the GWs observed by interferometer based GW detectors capable of detecting BBH mergers with total masses of a few $M_\odot$ to $10^8 M_\odot$.

1.1 Gravitational Waves from Binary Black Holes

BHs are the densest objects in the known universe, causing extreme spactime curvature, and when two BHs form a binary, they orbit at remarkable speeds. This immense acceleration causes BBH systems to be one of the most powerful sources of GWs. If GWs proved to be real and detectable, they would provide a way to study gravity in these most extreme regimes. The merger of BBH systems is often divided into three sections: inspiral, merger, and ringdown, although the boundaries between the sections are ill-defined. Inspiral describes the time during which the BHs orbit each other, with their separation gradually decreasing. Merger describes the highly non-linear regime during which the BHs make their final plunge and form a single BH. Ringdown refers to the time after the common horizon appears and the highly distorted remnant BH radiates away remaining energy until settling down to a single, isolated BH. Gravitational radiation is emitted during each of these stages, with a characteristic structure seen in Figure 1.1.

The form of the gravitational radiation is dependent upon parameters that describe the

source. BBH systems are described by 9 parameters: 2 masses (m_1 and m_2), 2 spin vectors ($\vec{a_1}$ and $\vec{a_2}$), and the eccentricity of the orbit (ϵ) which describes the deviation of the orbit from quasicircular. The shape of the GW simply scales with the total mass M, so we also introduce the mass ratio, $q = m_1/m_2 > 1$. A BH's dimensionless spin vector, $\vec{a}_i$, is obtained from the angular momentum as $\vec{a}_i = \vec{J}_i/m_i^2$, where the index i is used to distinguish between the BHs. In addition to the intrinsic parameters of the binary system, there are also extrinsic parameters including the inclination θ, the coalescence phase ϕ, and the distance D.

The gravitational strain can be expressed in terms of spherical harmonic modes:

$$h = \sum_{\ell=2}^{\infty} \sum_{m=-\ell}^{\ell} h_{\ell m -2} Y_{\ell m}(\theta, \phi)\,, \tag{1.1}$$

and changing the parameters of the system can change the relative impact of the modes. Generally, the $\ell = 2$, $m = 2$ mode is the most dominant. However, when q increases, or when the spins become highly precessing (not aligned with the angular momentum of the orbit), other modes can become more significant. This becomes more prominent when the binary is not observed face-on.

1.2 Detectors

Interferometer based detectors make use of interference patterns of light to measure very small changes in distance. Figure 1.2 shows the basic idea behind how these detectors work. Light from a laser is split and sent down two arms of a detector. It reflects back and recombines to be detected at the photodetector. When a GW passes through the detector, it compresses spacetime in one direction and stretches it in the other, causing the light from the laser to travel different distances in each arm of the detector. By observing the interference pattern at the photodetector, very precise measurements of this difference in distance can be made.

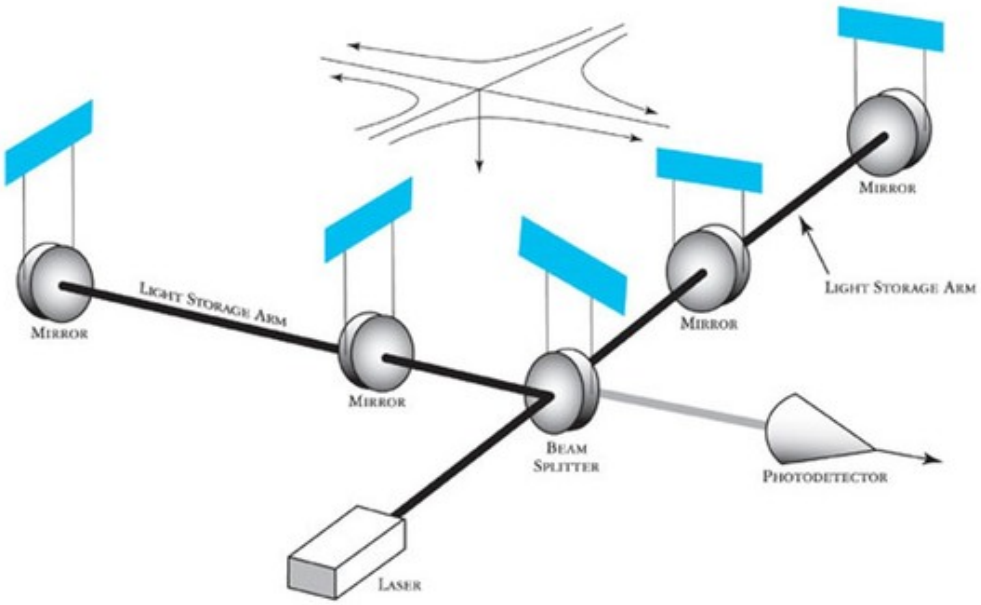

Figure 1.2: Basic design of an interferometer GW detector. The light from the laser is split at the beam splitter and sent down each arm of the detector, reflects back, and then recombines at the beam splitter and is detected at the photodetector. A GW passing through the detector changes the distance the light travels in each arm causing an interference pattern which can be used to measure the change in distance. Image credit: Caltech/MIT/LIGO Lab.

A number of interferometer based detectors have been designed and implemented over the years including GEO 600 [7], the Laser Interferometer Gravitational-wave Observatory (LIGO) [8], Virgo [9], and Kagra [10]. In the future, we expect to see the Laser Interferometer Space Antenna (LISA) and possible third-generation ground-based detectors such as the Einstein Telescope (ET) and Cosmic Explorer (CE). Since my work begins after a GW has been observed, I will not go in depth into the details of the construction of the interferometers themselves and will focus instead on the analyses used to characterize the detections. However, a brief overview of the detectors is useful for understanding how current and future detectors will vary.

1.2.1 Current Detectors

Laser Interferometer Gravitational-wave Observatory (LIGO)

The Advanced LIGO network consists of two detectors, one in Livingston, LA and one in Hanford, WA. With the current design, LIGO is able to detect frequencies as low as 10 Hz and is expected to see dozens of detections per year, consistent with the results of the second observing run (O2). These detectors consist of two 4 km arms set up as a modified Michelson interferometer. One of these modifications is a Fabry-Perot resonant cavity to multiply the phase change caused by the GW, greatly increasing the sensitivity. A power recycling mirror is also included to increase the effective power of the laser. Many additional techniques are in place to increase the sensitivity, extend the frequency range, and decrease noise [11]. The resulting sensitivity of the detectors are shown in Figure 1.3 [12].

Virgo

Advanced Virgo is a dual-recycled interferometer, consisting of 3 km arms, with Fabry-Perot cavities [9]. This makes it smaller than LIGO, but it uses similar techniques to amplify the signals, including utilizing recycled power to increase the strength of the laser. Figure 1.4 shows the sensitivity of Virgo during the second observing run.

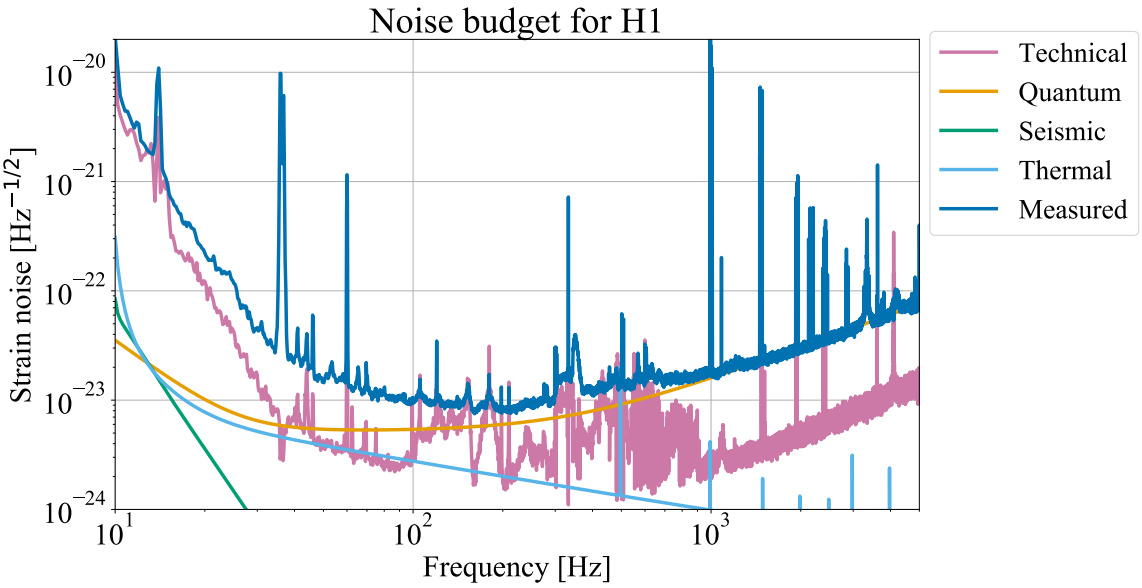

(a)

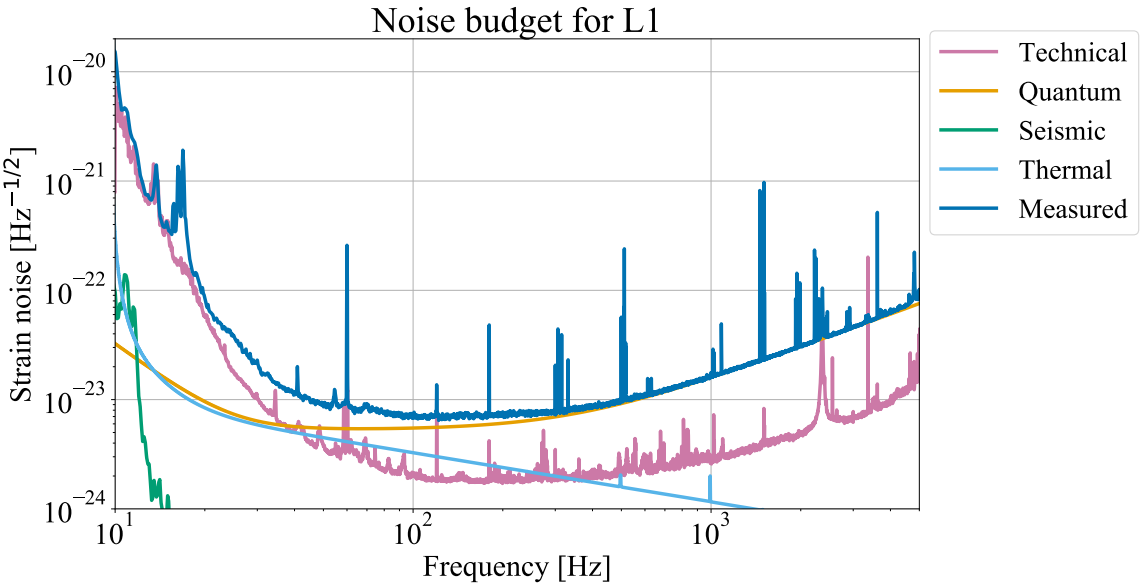

(b)

Figure 1.3: Sensitivity of Hanford and Livingston LIGO detectors during the second observing run. Image credit: [12].

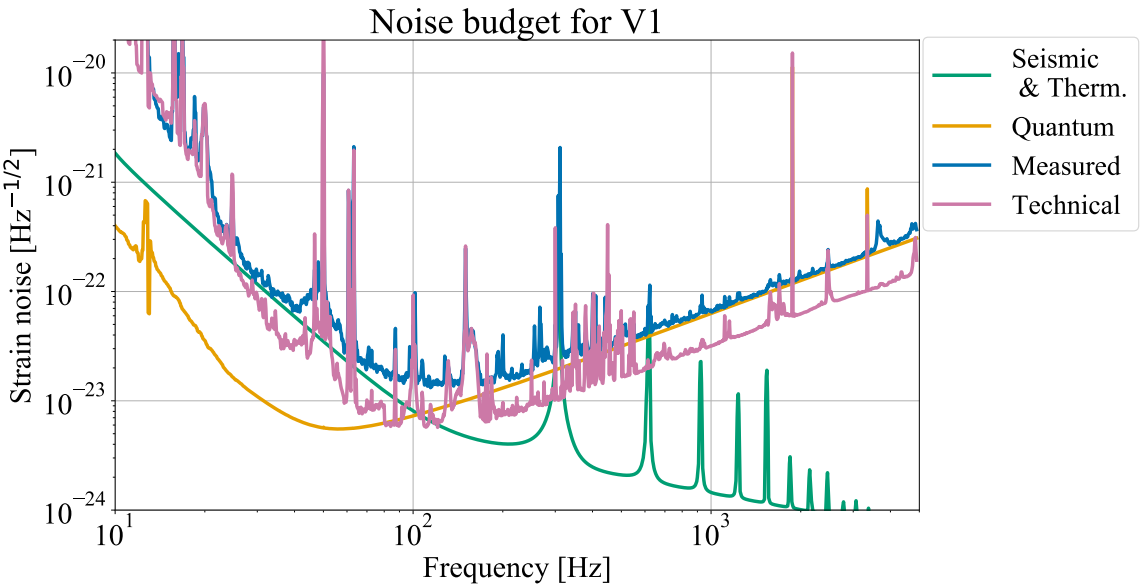

Figure 1.4: Sensitivity of Virgo during the second observing run. Image credit: [12].

By adding Virgo to the LIGO network of detectors, scientists are able to localize sources as well as make stronger statements about their intrinsic parameters. Together, LIGO and Virgo have published 50 GW signals from compact binary coalescences.

Kamioka Gravitational-Wave Detector (KAGRA)

Considered a 2.5 generation GW detector, the Kamioka Gravitational Wave Detector (KAGRA) is expected to join LIGO and Virgo in their search for GWs shortly. Located inside Mt. Ikenoyama, Kamioka, Gifu, Japan, KAGRA consists of two 3 km arms operating at cryogenic temperatures. These low temperatures improve the sensitivity in the 100 Hz region and are expected to play an important role in third-generation detectors.

Although now slightly outdated, Figure 1.5 shows the projected observing runs for each detector in the coming years [13]

1.2.2 Future Detectors

While the existing detectors have opened up the new field of GW astronomy, they are able to detect only a very specific set of sources. Future detectors look to expand the type

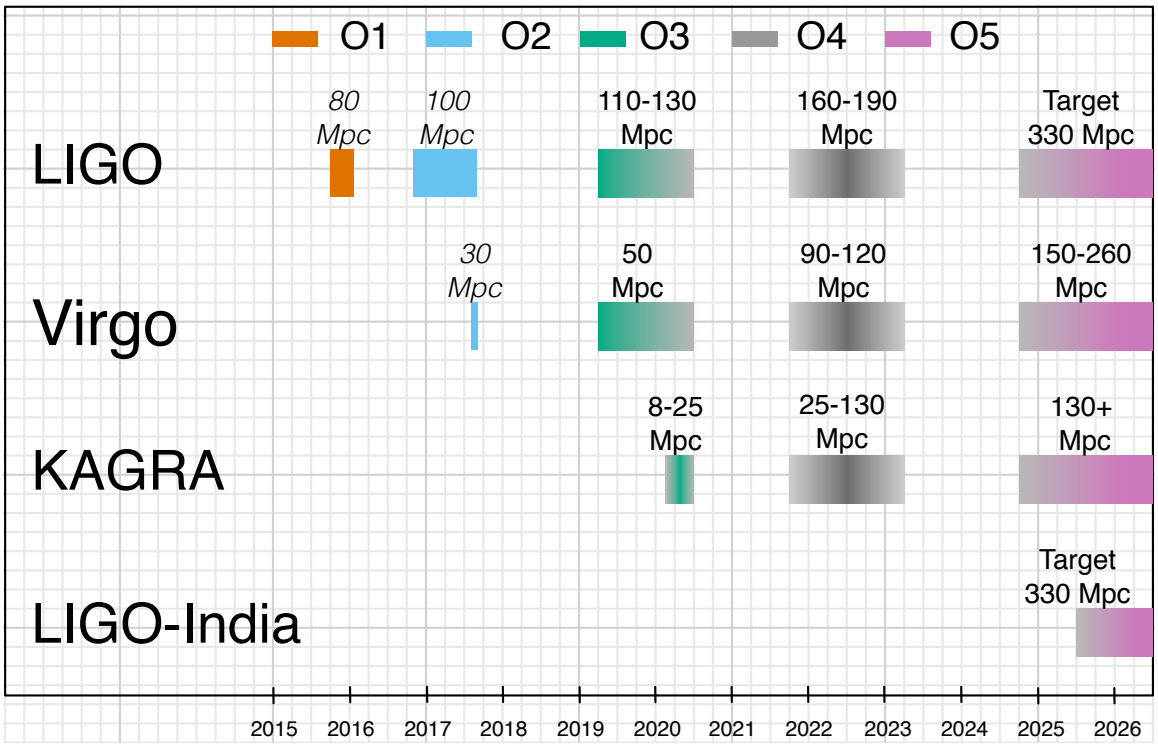

Figure 1.5: Expected observing runs for LIGO, Virgo, KAGRA, and LIGO India. Image credit: [13].

of sources able to be observed as well as increase the distance from which we are able to observe these sources. I will highlight ET and LISA here since they are used in later chapters.

Einstein Telescope (ET)

In order to improve upon the current, second-generation detectors, the European Commission began supporting institutions in the design of a new third-generation GW observatory, the Einstein Telescope (ET), currently expected to become operational sometime after 2032. They aim to improve the sensitivity of the current frequency range by a factor of 10 as well as push to lower frequencies [14]. ET is proposed to consist of three nested detectors creating an equilateral triangle, as shown in Figure 1.6. This is in stark contrast to the single "L" shaped detectors which comprise LIGO and Virgo. This new structure would allow ET to be sensitive to both polarizations of the GWs, and would also create a

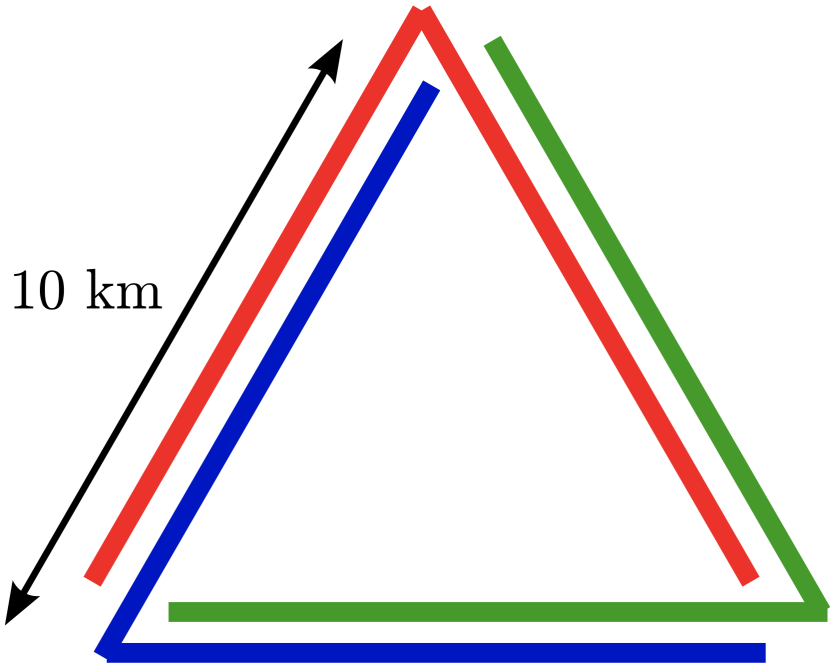

Figure 1.6: ET's triangular structure consisting of three nested detectors. Image credit: [15].

more isotropic antenna pattern. Each of these arms will be 10 km, a feature which is crucial to meeting the sensitivity goals of the mission. An important part of ET's mission is to build the infrastructure necessary to house multiple detectors, independent of the design of the detectors themselves. This infrastructure will allow it to be of use for decades, even while GW detectors are upgraded. In order to reduce seismic noise, which is particularly significant at low frequencies (3 Hz to 100 Hz), ET will be built underground at a depth of 100 m to 200 m.

Another critical design difference between ET and existing second-generation detectors is the xylophone configuration, which refers to having two interferometers as part of each detector. One interferometer is optimized to detect low-frequency signals, and the other is optimized for high-frequency signals. While the interferometer designed for high frequencies will operate at room temperature, the low-frequency interferometer will be run at cryogenic temperatures of 10K. This will greatly improve the sensitivity since at low

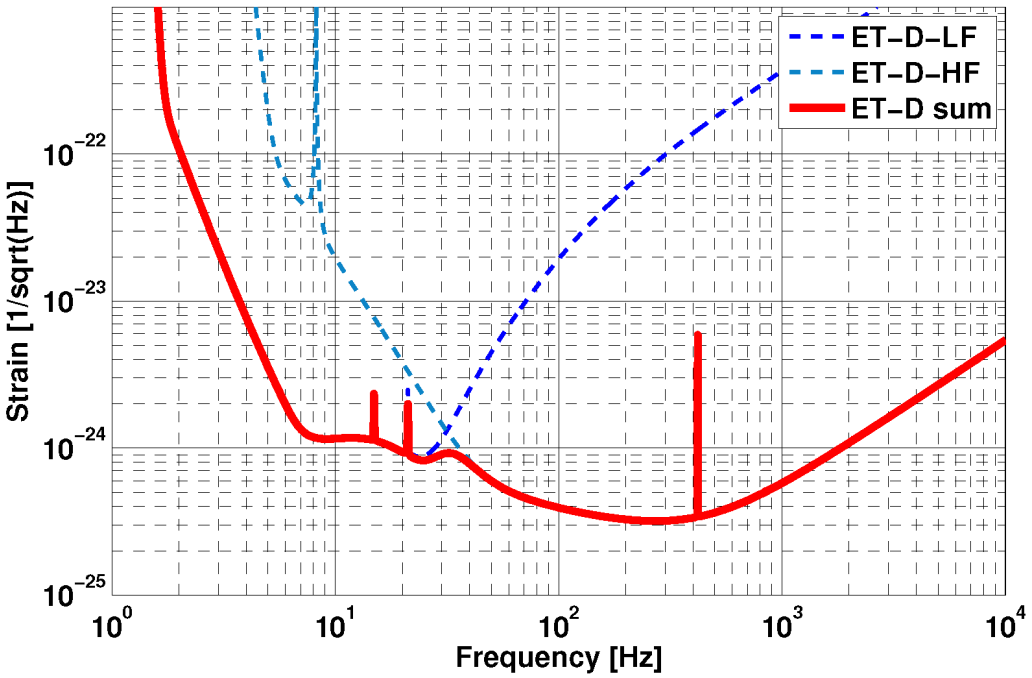

Figure 1.7: Sensitivity curves for ET, including both interferometers, one specialized for low frequency and one specialized for high frequency. Estimated using one single 90^o detector. Image credit: [15].

frequencies, suspension thermal noise is the main limiting factor [15].

The sensitivity curve of ET is the combined result of each of the interferometers and can be seen in Figure 1.7. However, this only shows the sensitivity for a single detector with arms separated by 90^o to allow for easy comparison with second-generation GW observatories. On average, the triple detector with 60^o between arms is slightly more sensitive [15].

Laser Interferometer Space Antenna (LISA)

In order to conduct the first survey of the milliherz GW band, the European Space Agency (ESA), with the National Aeronautics and Space Administration (NASA) as a junior partner, will launch LISA, a space-based GW observatory expected to fly in the early/mid 2030s. It will be a 4 year science mission with the possibility of an additional 6 year extension. The proposed schedule can be seen in Figure 1.8 [16]

This new observatory is expected to observe millions of binary systems, including

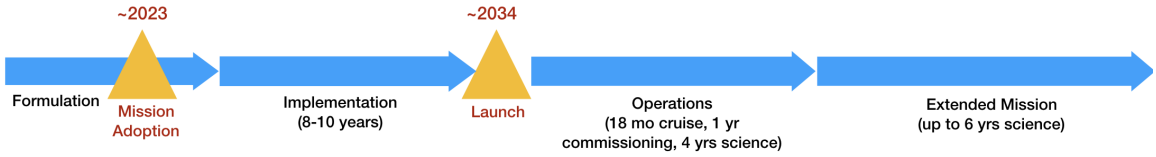

Figure 1.8: Expected schedule for the LISA mission. Image credit: [16].

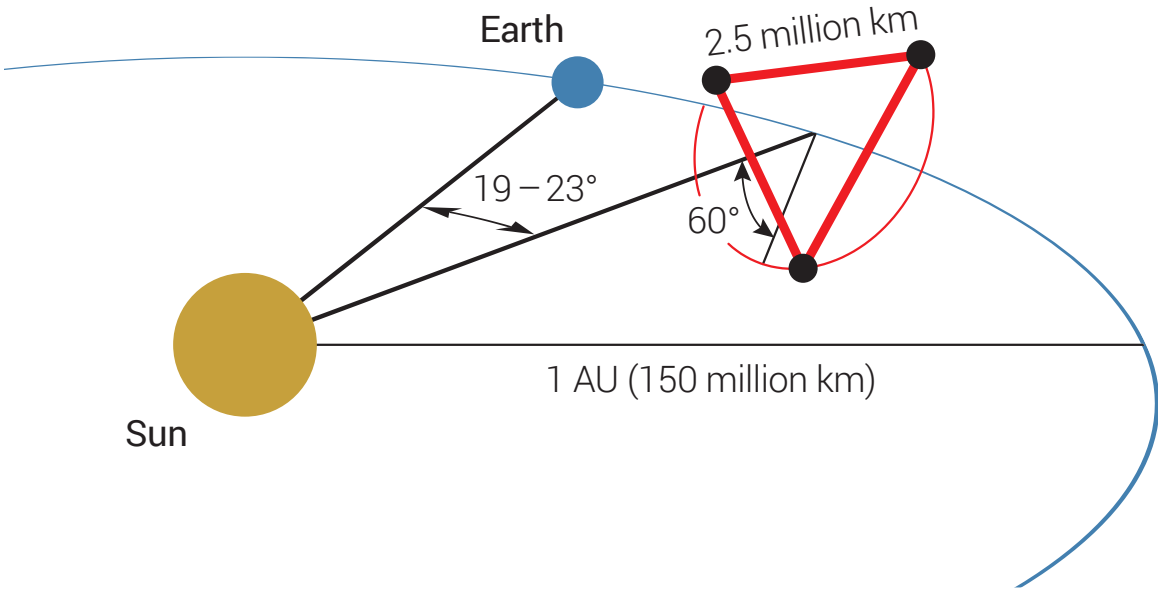

Figure 1.9: The LISA constellation, consisting of three spacecrafts in heliocentric orbits and maintaining a constant arm structure. Image credit: [16].

BBHs and galactic white dwarf binaries, tens of thousands of which will be able to be individually resolved. In order to reach the milliherz spectrum, the detector must be in space; ground based detectors are limited both by size and the gravitational coupling to seismic density fluctuations which limit the low frequency sensitivity. LISA will consist of three satellites constructed as an equilateral triangle inclined at 60^o to the orbital plane, with 2.5 Mkm sides. This three-arm structure will allow it to independently measure the polarization of the incoming gravitational radiation. LISA will follow a heliocentric orbit which will trail Earth by 20^o. This structure is shown in Figure 1.9 [16].

At each satellite sitting at a vertex of the triangle will be a pair of test masses and lasers. Thus, an interferometer which follows the same general principles as the current ground-based detectors will be centered at each satellite [16].

With its unprecedented sensitivity and reach, LISA will be able to observe at redshifts up to $z = 30$, allowing us to look beyond the epoch of reionization. It is expected to see a wide variety of sources, including hundreds of BBH systems with SNRs of $10 - 10^4$. BBH systems with total masses between $10 - 100 M_\odot$ may be seen in both LISA and ground-based detectors, with LISA observing inspiral and ground-based detectors catching the merger, providing a unique view into the merger process. SMBH observations will likely help us understand the co-evolution of galaxies and their central BHs [16] . Figure 1.10 shows the distances and redshifts at which LISA will be able to observe BBH systems of given total masses [16, 17] .

We also expect to see tens to hundreds of extreme mass ratio inspirals (EMRIs). A new multimessenger source may be the capture and disruption of white dwarfs by massive black holes (MBHs) in nearby galaxies. We may even be able to detect new sources such as inflationary fields and cosmic string cusps, which would have a significant impact on our understanding of cosmology and astrophysics. These new and exciting sources will help us study previously challenging subjects including the end state of stellar evolution and the birth process of MBHs [16] .

All of these sources are expected to be seen simultaneously in LISA and will be extracted using a global fit. Some will be individually characterizable, while others will make up the GW background and foreground. These sources are shown in Figure 1.11 in relation to the expected noise curve of LISA [16, 17] .

In order to compare these future detectors to LIGO, Figure 1.12 shows the characteristic strain for LISA, ET, and LIGO.

1.3 Detection Pipelines and Data Analysis

With detectors sensitive enough to react to the tiny changes caused by GWs, it's necessary to have the ability to analyze the data to identify GW signals and characterize them. The searches for GW signals can be classified into two categories: modeled and unmodeled.

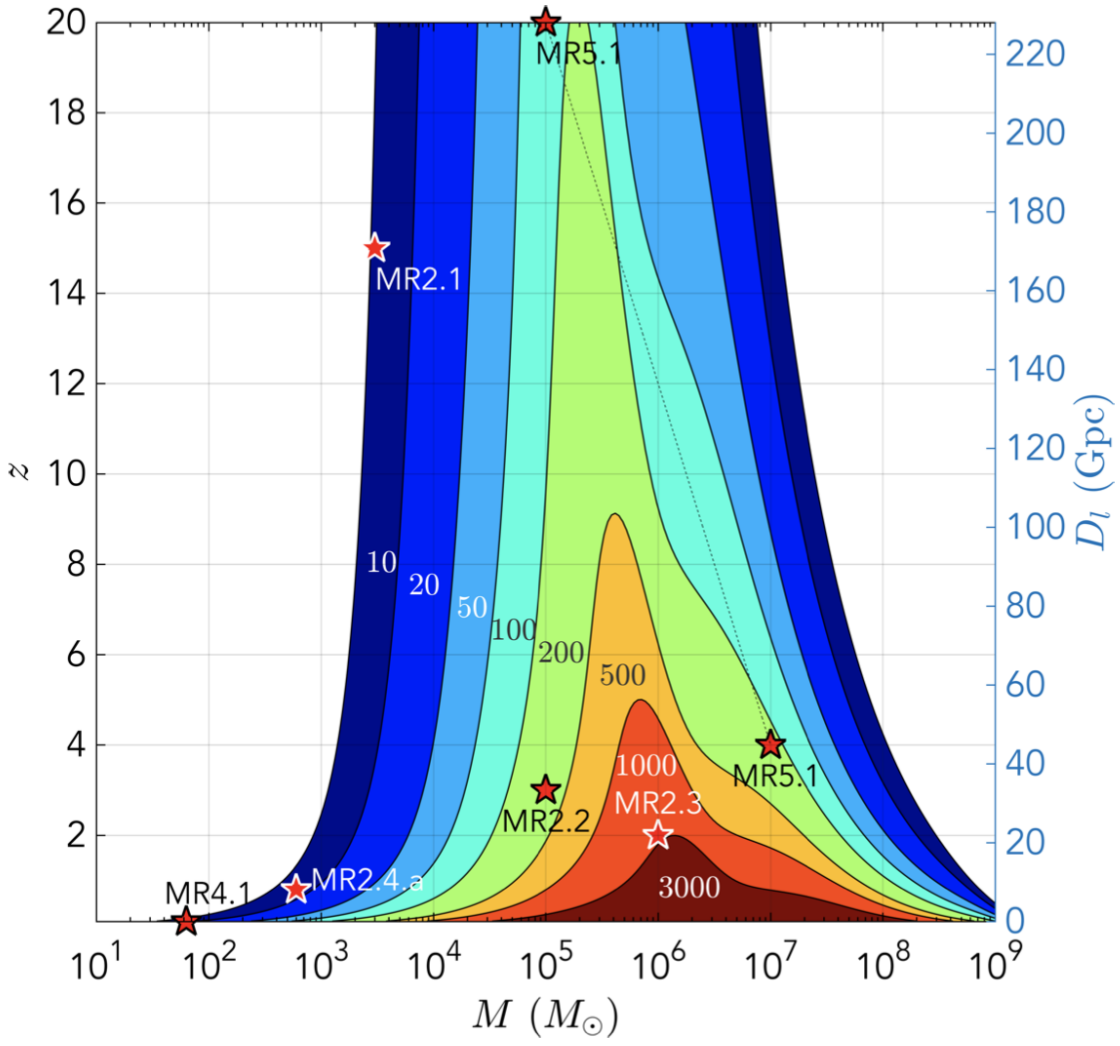

Figure 1.10: Redshifts and distances at which BBHs of given total mass are observable by LISA. The contours denote the expected SNR for such signals. Image credit: [17].

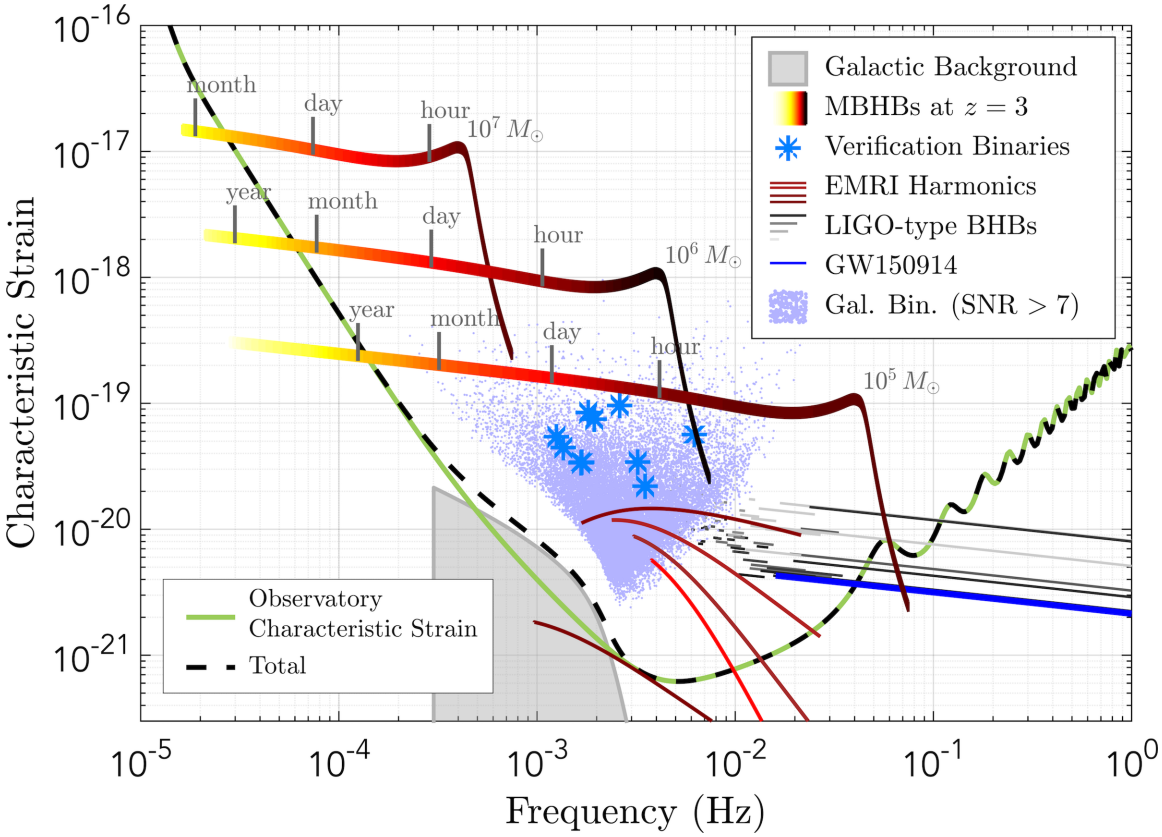

Figure 1.11: Expected sources in LISA as compared to the noise curve. Image credit: [17].

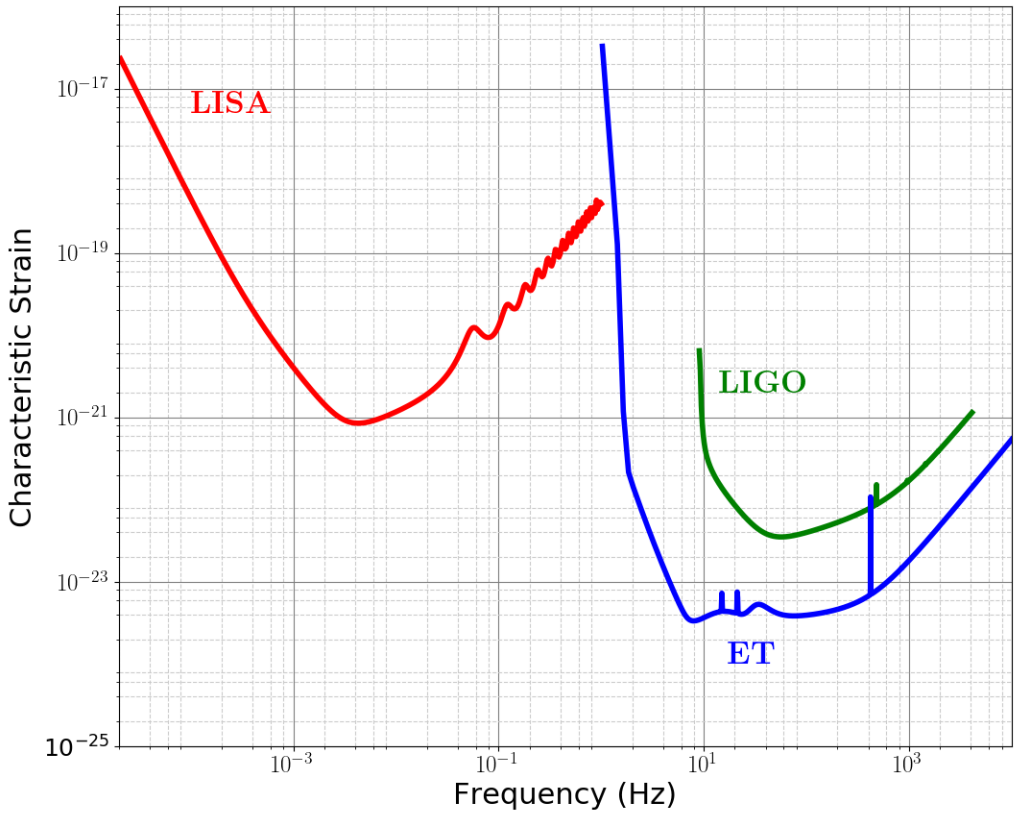

Figure 1.12: The amplitude spectral densities for LISA, ET, and Advanced LIGO at design sensitivity.

Modeled (CBC) searches use banks of theoretically generated signals of binary coalescences to match to the data, and unmodeled searches (burst) identify excesses of power within the detector.

1.3.1 Modeled Searches (CBC)

Modeled searches are referred to as such because they search the data for signals predicted by waveform models. The most theoretically motivated method for searching for signals within Gaussian data is matched filtering. While detector data is non-Gaussian, the technique still works well as the base method. The matched filtering is performed between the detector data and a bank of pregenerated waveform templates [18, 19, 20]. If a certain SNR threshold is met between the data and a template, it flags a detection.

The models used to generate the template banks are dependent upon the sources. Figure 1.13 shows the mass ratios and separations for which various approximation techniques are applicable for non-spinning binaries [21]. At large separations, Post-Newtonian (PN) models are the most applicable technique. Since the frequency of merger decreases with mass, for low mass binaries ($M < 12M_{\odot}$), LIGO is sensitive to only the inspiral, making PN models sufficient as template waveforms [22]. In cases with higher mass BHs, where the merger occurs in the frequency band, NR waveforms must be utilized. NR numerically solves Einstein's equations for the evolution and merger of BBH coalescences, generating the gravitational radiation predicted. Although NR can be used to simulate both BH and NS systems, I will only focus on BBH mergers. Chapter 2 will explore NR in more detail. NR simulations cover discrete points in the parameter space of BBHs, so analytic models are trained on NR waveforms to create continuous coverage of the space. To date, modeled searches have identified 50 GW signals from binary sources [23].

Before entering any of the search pipelines, time segments of the detector data are categorized according to the quality of the data. There are three categories: 1) the data has significant noise and must be discarded, 2) the data is clean enough to analyze and filter but

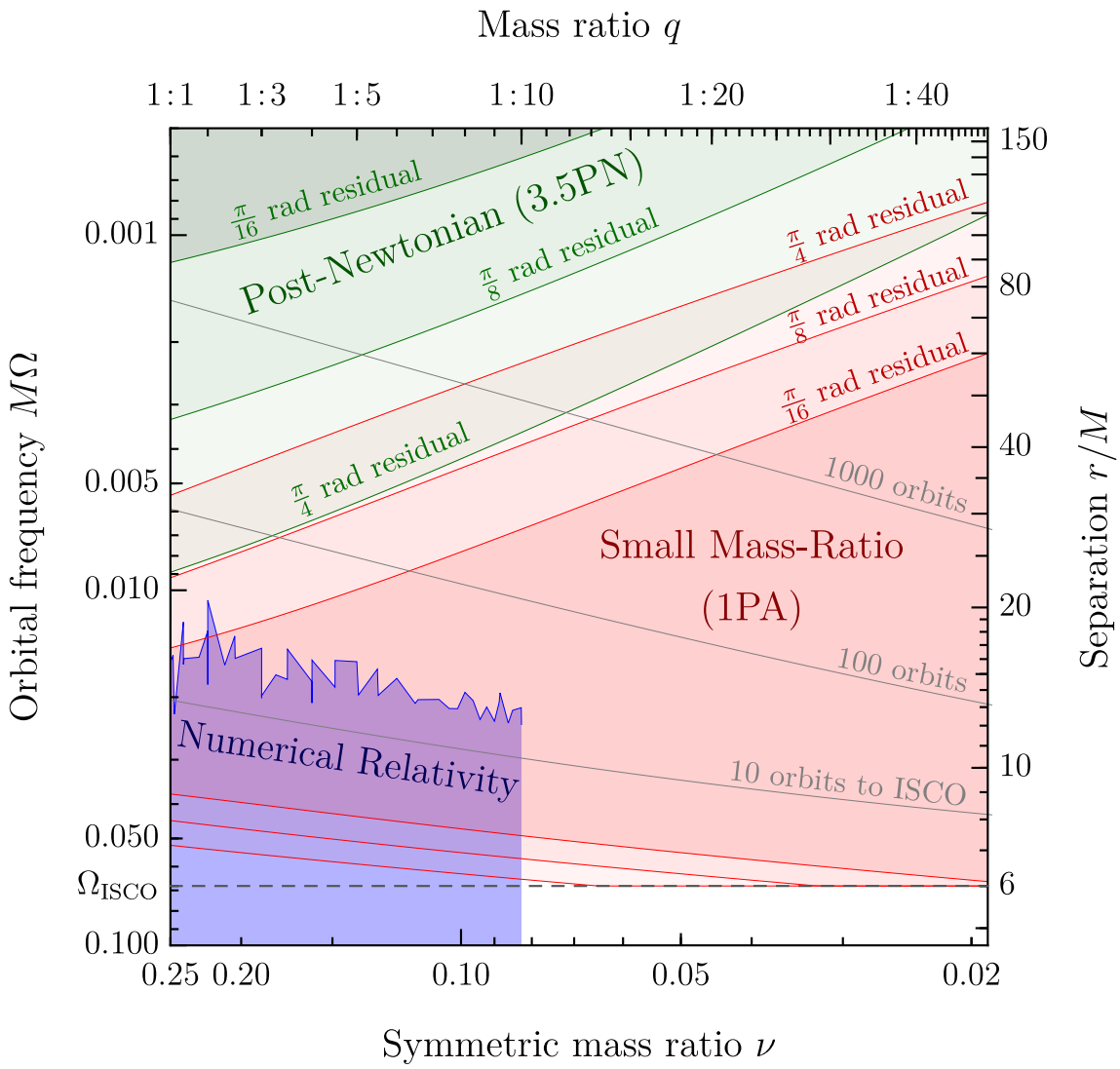

Figure 1.13: Mass ratios and separations for which various approximations are applicable for the modeling of nonspinning BBH systems. Image credit: [21].

some candidates may need to be vetoed due to noise transients, and 3) the data is suitable for all searches.

PyCBC

This search pipeline utilizes the PyCBC software framework [24] to conduct an all-sky search for compact binary coalescence (CBC) signals. It performs a matched-filtering analysis with a bank of template waveforms provided by models [25, 26]. A flowchart of this pipeline can be seen in Figure 1.14 [26]. The pipeline takes in calibrated strain data from the detector, already categorized based on data quality. This strain contains both stationary, Gaussian noise as well as non-stationary, non-Gaussian transients.

The pipeline then creates a template of waveforms to be used with all the detectors by creating a single power spectral density (PSD) averaged over time and over all the detectors. PSDs describe the power content as a function of frequency and, therefore, describe how sensitive the detector is at each frequency. The pipeline then constructs a template bank such that the loss of SNR due to the discrete nature of the templates is $< 3\%$. Using a single template bank for all detectors allows the pipeline to require that signals in different detectors be picked up by the same template.

The data from each of the detectors is then matched against the template bank using matched filtering maximized over sky location and orientation. The method of matched filtering used here is a modification of the FindChirp algorithm [27]. The data signal, $h(t)$, is projected into two orthogonal phases, h_{cos} and h_{sin}. The matched filter then utilizes a noise weighted inner product to solve for the SNR [26]:

$$\rho^2(t) = \frac{(s|h_{cos})^2 + (s|h_{sin})^2}{(h_{cos}|h_{cos})} \tag{1.2}$$

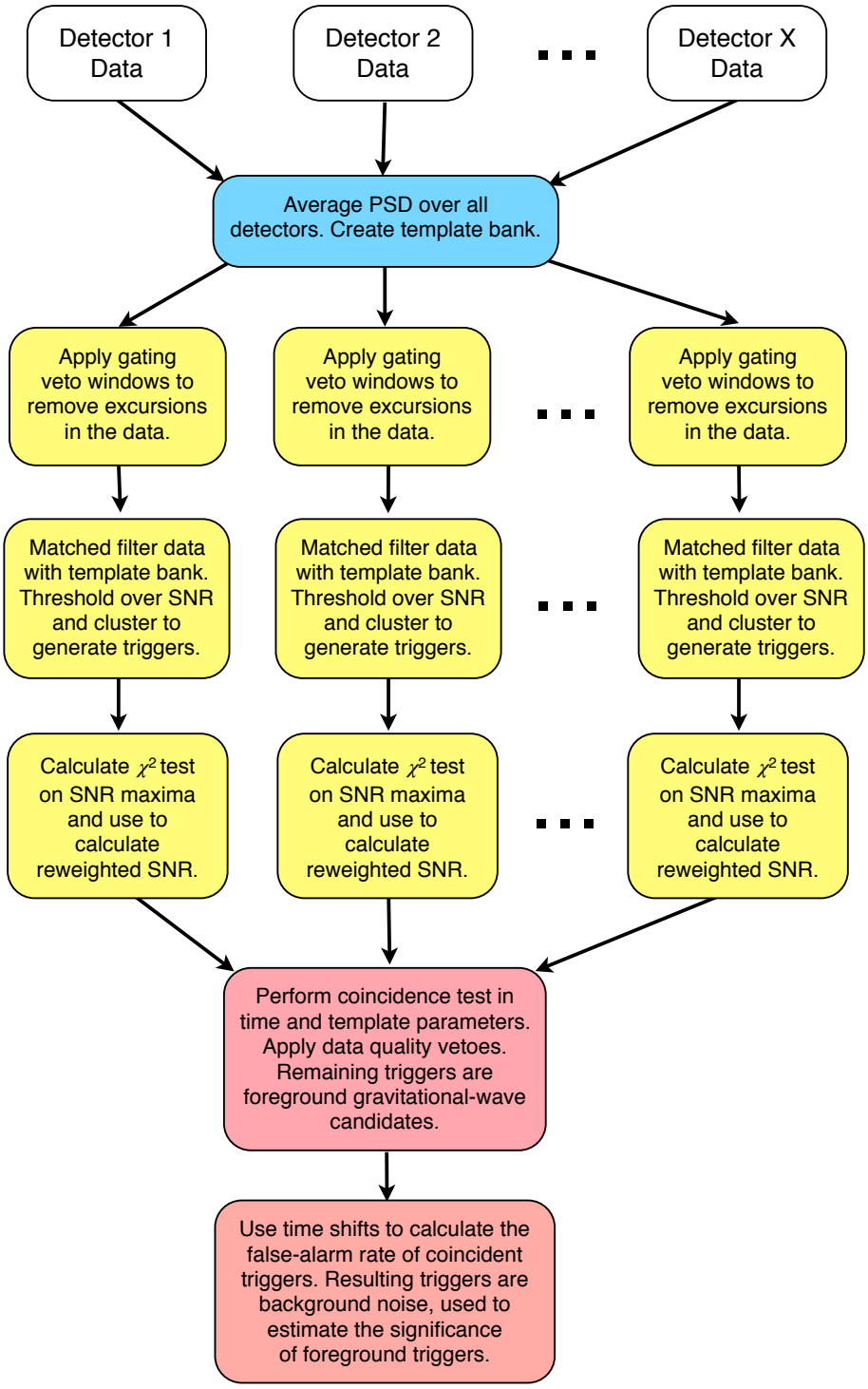

Figure 1.14: Flowchart of the PyCBC search pipeline. Image credit: [26].

with the inner product defined as [26]

$$(s|h)(t) = 4Re \int_{f_{low}}^{f_{high}} \frac{\tilde{s}(f)\tilde{h}^*(f)}{S_n(f)} e^{2\pi i f t} df. \tag{1.3}$$

$\tilde{s}(f)$ is the Fourier transform of the detector data, $\tilde{h}(f)$ is the Fourier transform of the template waveform, and $S_n(f)$ is the one-sided PSD of the detector.

The pipeline then identifies locations where the computed SNR goes above a certain threshold. A clustering algorithm then creates a set of *triggers*, times at which signals may have occurred.

Next, to weed out noise transients that may have been picked up as signals, a chi-squared test is performed to see how consistent the observed time frequency power distribution is with the expected distribution from the template. The value of the reduced chi-squared (χ_r^2) should be close to unity for a real signal. A high value of χ_r^2 implies a likely noise transient. A weighted SNR is computed using χ_r^2:

$$\hat{\rho} = \begin{cases} \rho \Big/ [(1 + (\chi_r^2)^3)/2]^{\frac{1}{6}}, & \text{if } \chi_r^2 > 1, \\ \rho, & \text{if } \chi_r^2 \leq 1. \end{cases} \tag{1.4}$$

This is then compared to a threshold value to remove likely noise transients.

As a result of having a network of detectors, consistency between detectors can be used as a requirement for identifying candidate events. The arrival time at each of the detectors must be consistent with the predicted speed of GWs within the uncertainty of detection time. For LIGO Hanford and LIGO Livingston, this requires that the detections occur within 15ms of one another. The template used to detect the signal must also be the same in each of the detectors. If a signal satisfies all of these requirements, it becomes a *candidate event*. These are then ranked by $\hat{\rho}_c$, the square-root of the sum of the squares of $\hat{\rho}$ in each individual detector.

The false-alarm-rate (FAR) within the search much be computed empirically. This is

done by time shifting the data within one detector compared to the other. The minimum time shift is greater than the maximum allowed travel time of GWs between the detectors, meaning no real coincident signals should be picked up. The coincidence test is then performed on the time-shifted data, searching for any coincidences between the detectors. Due to the time shift, any coincident signals observed must be false alarms. By performing numerous time shifts, the FAR for coincident signals can be estimated.

GstLAL

Another pipeline used heavily with LIGO data is GstLAL [28, 29, 30], a low-latency pipeline which identifies signals as well as the parameters which may describe them and determines event significance, making use of LALSuite [31]. When operating in low-latency mode, it can identify signals within seconds of detection. GstLAL also has an offline mode which analyzes arxived data with additional information. While the GstLAL pipeline is similar to the PyCBC pipeline in many ways, there a a few crucial differences. The primary difference is that GstLAL performs the match filtering and consistency tests in the time domain rather than the frequency domain. Additionally, it uses a different ranking statistic and method to estimate the FAR

As in the PyCBC pipeline, GstLAL performs matched filtering on a bank of templates, maximizing over both the intrinsic and extrinsic parameters of the system. These templates are constructed using PN or effective one body (EOB) models, which can be hybridized with waveforms generated by perturbation theory or NR to make full inspiral, merger, ringdown (IMR) templates. In O2, only aligned spin templates were included, meaning the extrinsic parameters only come in as an amplitude scaling or a shift in the phase. Similar to PyCBC, this template bank is constructed such that the mismatch between a signal and the nearest template is no more than 3%.

The SNR is computed in the time domain as [32]

$$x_i(t) = \int_{-\infty}^{\infty} d\tau \hat{h}_i(\tau)\hat{d}(\tau + t)\,, \tag{1.5}$$

where $\hat{d}(\tau)$ is the whitened data defined as

$$\hat{d}(\tau) = \int_{-\infty}^{\infty} df \frac{\tilde{d}(f)}{\sqrt{S_n(|f|)/2}} e^{2\pi f\tau}\,, \tag{1.6}$$

and $\hat{h}(\tau)$ is the whitened template. The subscript i runs over the template parameters.

The pipeline creates a complex SNR timeseries, where the real part corresponds to the SNR of the $+$ polarization and the imaginary part corresponds to the SNR of the $\times$ polarization. When maximizing the SNR over time and phase, the magnitude is considered.

Anything that passes the given SNR threshold is analyzed for signal consistency to remove potential glitches. If the template matched the signal exactly with no noise, the SNR timeseries of the data would identically match the SNR timeseries of the template. Therefore, the two SNR timeseries are compared and must be within a certain threshold. This is very similar to PyCBC but is performed in the time domain rather than the frequency domain.

Anything that passes this consistency test becomes a *trigger*. As in PyCBC, triggers in different detectors must be observed by the same template and must fall within a reasonable time window. Triggers which are not coincident across detectors are used to establish background noise for estimating FAR. The triggers are assigned log likelihood-ratios and a Monte Carlo algorithm is used to turn this into a FAR.

RIFT

The RIFT [33] parameter estimation pipeline allows for the use of NR waveforms directly in addition to models. This form of rapid parameter estimation is based upon Pankow *et. al* [34]. This pipeline enables the use of computationally expensive or unique models, as

well as mixed approximations, and can also be applied to NSs, allowing for estimations of equation of state.

The initial version of the pipeline compared each signal to a uniform grid of source parameters, producing an array of likelihood values, a process referred to as ILE. With this grid, they would interpolate to estimate the most likely source parameters of the system. This efficient computation of likelihood is the reason this method has been referred to as Rapid PE. RIFT takes this idea and expands upon it in several ways. It permits the use of an unstructured grid, particularly useful when using NR waveforms which are often speckled throughout parameter space. It also uses Gaussian processes [35] for the interpolation and introduces an iterative procedure. Each iteration produces a set of proposed posteriors which then inform the next iteration about where to search.

RIFT marginalizes over all the extrinsic parameters in order to isolate the intrinsic parameters of the system: masses and spins for the case of BBHs. They also make use of the effective spin to reduce the degrees of freedom [33]:

$$\chi_{eff} = (\boldsymbol{S_1}/m_1 + \boldsymbol{S_2}/m_2) \cdot \hat{L}/M \tag{1.7}$$

where they assume that the angular momentum $\hat{L} = \hat{z}$.

The RIFT pipeline creates an intrinsic posterior distribution and then utilizes adaptive Monte Carlo to construct samples. This produces a sequence of weighted points which characterize the posterior distribution. It then computes the likelihood, and utilizes this set to inform the next iteration where to search.

In order to make the search more efficient, it is also possible to perform the first few iterations with fewer degrees of freedom. For example, the algorithm can search for effective spin instead of all of the individual spin parameters. Additionally, the initial search grid can be established using parameter estimates provided by other search pipelines.

All of these search pipelines, as well as others I have not described, require banks

of template waveforms. The template banks for PyCBC and GstLAL are built using PN waveforms as well as waveform models trained on NR simulations, and RIFT often uses NR waveforms directly. This highlights the need for a bank of NR waveforms which spans the parameter space of BBHs. These waveforms must be well enough resolved that their error is insignificant in comparison to modeling errors and detector noise.

1.3.2 Unmodeled Searches (Burst)

In addition to performing modeled searches which look for particular sources of GWs, LIGO also performs unmodeled searches. These look for excess power in the detector data and can pick up signals generated by many different sources including binary mergers, supernovae, NS collapses, and pulsar glitches, among others. This type of search requires minimal assumptions about the sources and their morphology. To be considered an event, these searches set a FAR threshold of 1 per 100 years which corresponds to being roughly 3σ above the noise. Two end-to-end searches currently used are Coherent WaveBurst (cWB) and omicron-LIB (oLIB) and a followup pipeline is *BayesWave* (BW) [36, 37].

Coherent Waveburst (cWB)

The cWB pipeline searches for excess power consistent across multiple detectors in the time-frequency domain [36]. It begins by whitening the detector data and converting it into the time-frequency domain. Data from each of the detectors is combined to create a time-frequency power map. By identifying clusters of points within the map which have higher power than the threshold (which is established by the baseline noise), triggers can be identified. This is repeated for seven different frequency resolutions which range from 1 Hz to 64 Hz by powers of two. When clusters of excess power are maintained across the resolutions, this is classified as a *trigger*.

These triggers are analyzed to construct the waveform and identify the polarization and

sky location [38, 39]. The signals are then compared across the detectors, as it is crucial that they be consistent. Due to the similar structure of H1 and L1, the waveforms must look similar in each. To quantify how consistent the signals are across detectors, the network correlation coefficient is computed as $c_c = E_c/(E_c + E_n)$ where E_c is the normalized coherent energy and E_n is the normalized energy of the residual noise. Since a true signal should be coherent and should have minimal residual noise, any signal with $c_c < 0.7$ is discarded from the analysis. The signals are reconstructed over a uniform grid of sky locations and are selected to maximize the likelihood statistic $L = c_c E_s$, where E_s is the energy of the waveform. Remaining triggers are then ranked according to their coherent network SNR, $\eta_c = (2c_c E_c)^{1/2}$ [36, 40].

The data is then split into two frequency bands to perform further analysis and classification. All signals above 1024 Hz are classified together. Those in the low frequency band are split into three categories based upon their morphology. First, "blip glitches" are identified, and classified into $C1$. These are time symmetric and have no apparent frequency evolution. Also added to $C1$ are non-stationary narrow-band glitches. These are identified as any signal which has 80% of its energy localized to within 5 Hz. Next, in order to identify compact binary mergers, any signals with the appropriate frequency evolution, described by the parameter $\mathcal{M}$, are placed in $C3$. For the case of a compact binary coalescence, this parameter corresponds to the *chirp mass*. To compute $\mathcal{M}$, the following equation is fit to the time-frequency evolution [40]:

$$\frac{96}{5}\pi^{8/3}\left(\frac{G\mathcal{M}}{c^3}\right)^{5/3}\frac{3}{8}f^{-8/3} + C = 0\,. \tag{1.8}$$

If $\mathcal{M} > 1M_\odot$, the signal is placed in $C3$. The final class, $C2$, consists of all remaining signals which were not placed into $C1$ or $C3$.

To determine the FAR, a timeshift method very similar to the one described for the modeled searches is performed individually for each class. It can be noticed that the FAR

for $C3$ is much lower, meaning it is unlikely that cWB will recover a false chirping signal [40]. Figure 1.15 shows the cWB reconstruction along with the BW reconstruction (to be described in a later section) for GW150914 [40].

Omicron-LIB (oLIB)

The other end-to-end unmodeled search pipeline frequently used is oLIB [41], a hierarchical, low-latency search algorithm, which can produce results within 30 minutes of an event [40, 36]. It also has an offline mode which allows for further followup. The analysis is broken into two main steps.

First, "Omicron" is used to identify segments of data with excess power within each detector separately. This is done using a Q-transform, which could be considered similar to matched filtering with a bank of sine-Gaussian waveforms. These regions of excess power are then compared across the detector network to determine coincidence. In order to be considered, a signal must have the same frequency, f_0, and quality factor, Q, in each detector. The signals must also fall within 10ms of one another (when considering L1 and H1) to be designated as triggers. Events within 100ms of one another with the same frequency and quality factor are then combined. The events with the highest SNRs are selected until no remaining triggers fall within 100ms of one another [40]. Single detector events with SNR> 5 are considered.

All the triggers are then analyzed with LALInference Burst (LIB), a tool based on LALInference, used for parameter estimation and model selection. While LALInference assumes a compact binary coalescence as the source of the GW signal, LIB allows for more generic sources, modeled using sine-Gaussians, Gaussians, and damped sinusoids. The default for the oLIB pipeline is to use LIB to model the signals with a single sine-Guassian and produce posterior distributions for all 9 parameters, intrinsic and extrinsic. LIB also produces two bayes factors, which measure the evidence ratio between two scenarios: coherent GW signal versus Gaussian noise (BSN) and coherent GW signal versus

an incoherent noise transient (BCI) [41]. These are combined into a single scalar likelihood ratio, Λ.

The triggers with positive bayes factors are then divided into two categories based on the parameters of the sine-Gaussian. The "low-Q" category encompasses all triggers with $0.1 < Q < 2$ and is similar to cWB's $C1$ category, isolating likely glitches and noise. The "high-Q" category includes all triggers with $2 < Q < 108$ and resembles cWB's $C2$ and $C3$ categories, including all likely GW signals. The FAR and significance can be estimated by performing time shifts, creating an expected background distribution of the likelihood ratio, Λ.

BayesWave (BW)

For systems which are well modeled, signals can be pulled out of the noise even without strong noise characterization. However, when searching for unmodeled waveforms, accurately characterizing the noise becomes crucial. BW, a follow-up algorithm, models and characterizes both glitches and the GW signal as a variable number of sine-Gaussian wavelets and then computes the bayesfactor between the two [42, 43]. This leads to the name *BayesWave* as it is a combination of the terms "Bayesian" and "wavelets." BW's analysis is done in the frequency domain and is best for short duration signals such as core collapse supernovae and BBH mergers.

In order to choose the number of wavelets, the algorithm uses a Reversible Jump Markov Chain Monte Carlo (RJMCMC) [36]. This is done separately in each detector and the signal is reconstructed at a specific location, for example the center of the Earth. Using *BayesLine* to model the noise with a multi-component parameterized model, it produces a posterior distribution of the parameters for each model (signal and noise). For the signal, this includes the waveform itself as well as the source position. This can be used to create distributions of characteristics of the signal such as the duration and the central frequency. The reported detection statistic is dependent upon both the fit of the data as well

as the number of wavelets used. This favors more complex time frequency structure [40] and also prevents the risk of overfitting the data [42].

To summarize the properties of the gravitational waveform, h, BW uses the posterior distribution defined as [42]

$$p(\mathbf{h}|\mathbf{s}, M) = \frac{p(\mathbf{h}|M)p(\mathbf{s}|\mathbf{h}, M)}{p(\mathbf{s}|M)}\,, \tag{1.9}$$

where M is the model, and $\mathbf{s} = \mathbf{R} \star \mathbf{h} + \mathbf{n}$ is the data consisting of both noise and the signal. The noise is broken into two components, glitches, $\mathbf{g}$, and colored Gaussian noise, $\mathbf{n}_G$. The data can then be rewritten as $\mathbf{s} = \mathbf{R} \star \mathbf{h} + \mathbf{g} + \mathbf{n}_G$, where $\mathbf{R}$ accounts for the time delay between detectors. The likelihood function is defined as [42]

$$p(\mathbf{s}|\mathbf{h}, M) = \frac{\exp[-(\mathbf{r}^T \cdot \mathbf{C}^{-1} \cdot \mathbf{r})/2]}{((2\pi)^N \mathrm{det}\mathbf{C})^{1/2}} \tag{1.10}$$

where $\mathbf{C}$ is the noise correlation matrix and N is the length of $\mathbf{s}$ [42, 43].

Figure 1.15 shows the reconstruction of GW150914 from cWB and BW.

1.3.3 Future Data Analysis Challenges and Techniques

The most exciting aspects of future detectors such as LISA also create a unique data analysis challenge. LISA expects to see on order of 10^4 signals above the SNR threshold for detection, all observed simultaneously within the LISA data stream. While these overlapping signals do complicate the data analysis and parameter estimation, the longer signals have more cycles in LISA's frequency band which will aid in resolving and characterizing them [16].

In order to analyze the vast amounts of data that will be provided by LISA, scientists will need to draw on existing data analysis techniques (matched filtering, Markov Chain Monte Carlo (MCMC), etc) utilized by terrestrial detectors as well as create new tools to tackle the specific nature of LISA. In the late 2000's, the Mock LISA Data Challenges

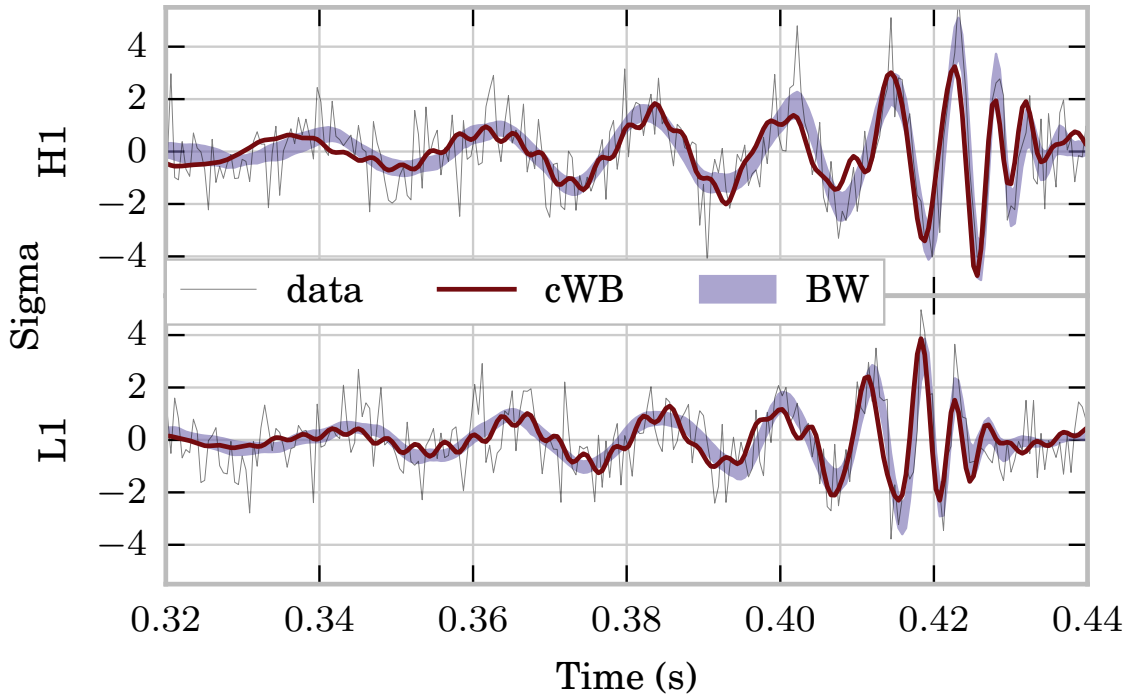

Figure 1.15: Point reconstruction of GW150914 by cWB and the 90% confidence interval constructed by BW as compared to the data. Image credit: [40].

(MLDC) were created to encourage the development of data analysis techniques as well as to showcase the readiness of the scientific community to utilize LISA's data [44, 45]. These have since been renewed (https://lisa-ldc.lal.in2p3.fr/ldc), drawing on and expanding upon the original MLDC.

The original MLDC consisted of multiple challenges, separated by 6 months, each growing in complexity. The organizers would provide mock LISA data, consisting of simulated noise (realistic or simplified) accompanied by one or more signals. With the exception of specific cases, the mock data stream consisted of 1 year of data. Challengers would then be tasked with identifying as much information as possible about the sources of the included signals. In addition to the challenge data, which had signals with parameters unknown to the challengers, the organizers would also provide training data which included the parameters to aid in the development of techniques. The tools to create the data streams were also public, allowing challengers to create their own mock data streams. Groups were

asked to submit their results along with descriptions of their techniques.

Recently, the MLDC has been rebooted, with the first challenge, known as Radler, having ended on December 2019. This challenge consisted of 6 subchallenges, many of which were similar to those put forward in the earlier challenges of the 2000's. A key difference, however, is that the current challenge is not blind; the groups are able to access the parameters of the included signals if they so choose, similar to the training data from the previous challenges. For each of the subchallenges, data streams were provided with and without noise. The subchallenges are as follows: 1) a single signal from a BBH system, 2) a single signal from an EMRI, 3) overlapping verification Galactic white dwarf binaries, 4) a population of 26 million Galactic white dwarf binaries, 5) a population of stellar mass BBH systems, and 6) an isotropic stochastic background of primordial origin. These are described further at: https://lisa-ldc.lal.in2p3.fr/ldc .

A number of promising data analysis techniques were highlighted by the MLDCs [46, 47, 48]. The Metropolis-Hastings Search Algorithm developed by Cornish and Porter [49] is an iterative algorithm which finds the brightest source, removes it, and then repeats the search for the next signal. A quite useful aspect of this technique is that it is able to separate out the extrinsic and intrinsic search parameters, shrinking the search parameter space.

Gair and Porter developed the Hybrid Evolutionary Algorithm [50] which, unlike the Metropolis-Hastings Search Algorithm, simultaneously searches for multiple sources. It combines the Metropolis-Hastings algorithm with nested sampling and evolutionary rules. It begins with a number of trial solutions, or organisms, and cluster centroids which are dropped onto the likelihood surface. In order to survive and continue to the next iteration, these trial solutions much satisfy certain fitness criteria including having an SNR greater than the threshold value. After the initial elimination, individual trial solutions are required to be fitter than the average fitness of all the trial solutions. They are then able to evolve to improve their fitness, and often form clusters. The centroids are now assigned to the center of mass of each of these new clusters, and the evolution of these centroids is the primary

focus from this point. This method was tested on a data set with two SMBHs, one bright coalescing source and one dim non-coalescing source. The algorithm was told there would be between 2 and 8 possible sources. It was able to find both primary and secondary modes to within 5σ.

Another algorithm is MultiNest developed by Feroz, Hobson, and Bridges [51] which improves upon some of the difficulties associated with nested sampling. In particular, it becomes challenging to randomly find a better place in the parameter space once you're already close to the solution. MultiNest addresses this by using the current set of live points to model the likelihood surface. This method was able to find 11 modes, including seven which were found by the Hybrid Evolutionary Algorithm.

The development of GW detectors and search pipelines capable of detecting coalescing compact binaries has brought about the era of GW astronomy. However, detecting and analyzing GW signals relies upon understanding the expected form they should take, based upon the theory. For binaries of moderate to low mass ratios, generating these predicted GW signals can only accurately be done using NR.

CHAPTER 2

INTRODUCTION: NUMERICAL RELATIVITY

With the detection of GWs opening up a new way to observe the universe, it is important to be able to maximize the scientific gain from each detected signal. Accomplishing this requires a theoretical understanding of the sources as well as the radiation they emit. This is provided by NR, which computationally solves the two body problem in GR.

The key differences between Newton's and Einstein's theories are the nature of gravity itself and the constancy of the speed of light. Einstein's theory of special relativity was based upon the notion that the laws of physics are identical in all inertial reference frames and the speed of light is constant in all inertial reference frames. This significantly altered the way time was treated; rather than being a constant vector, marching forward at the same rate for all observers, its behavior depends upon the reference frame of the observer. As a result, time and space cannot be treated independently, but instead must be considered together in a four-dimensional structure referred to as *spacetime*.

This theory was referred to as "special" because it only handled a very specific scenario, the one in which spacetime is flat. Einstein went on to develop his theory of *general* relativity which addressed the curvature of spacetime, caused by the presence of matter, and governed by what is referred to as the Einstein field equations,

$$G_{ab} = 8\pi T_{ab}\,. \tag{2.1}$$

Here, G_{ab} is the symmetric Einstein tensor,

$$G_{ab} = {}^{(4)}R_{ab} - \frac{1}{2} g_{ab}\, {}^{(4)}R \tag{2.2}$$

where ${}^{(4)}R_{ab}$ is the 4-dimensional Ricci tensor, $R = g^{ab}R_{ab}$ is its trace, and g_{ab} is the

4-dimensional metric. T_{ab} is the symmetric energy-momentum (or stress-energy) tensor. The left side of Einstien's equation describes the structure of spacetime and the right side describes the matter which informs that structure.

This reinterpreted the nature of gravity; rather than gravity being a force as Newton had described it, gravity was simply the effect that matter had on the curvature of spacetime. John Wheeler summarizes this nicely stating, "Space-time tells matter how to move; matter tells space-time how to curve." The fact that spacetime itself changes with time makes Einstein's equations impossible to solve analytically for all but the most symmetric of cases.

In fact, for decades after the unveiling of Einstein's equations, scientists were only able to find solutions to highly symmetrical cases such as single BHs. The solution for a single spherical mass with no electric charge and no angular momentum was found in 1916 by Karl Schwarzschild [52]. The solution to this system is referred to as the Schwarzschild metric and depends only upon the mass of the BH. From this result came the idea of an event horizon, the boundary from within in which nothing can escape to spatial or temporal infinity.

Shortly after Schwarzschild developed his solution to the nonspinning, uncharged mass, Hans Reissner, Hermann Weyl, Gunnar Nordström, and George Barker Jeffrey found the solution to the nonspinning, charged, spherical mass [53, 54], subsequently named the Reissner-Nordström metric. It took many more years before the spinning BH case was solved, but in 1963, Roy Kerr introduced his solution to a rotating, uncharged mass, referred to as the Kerr metric [55]. In 1965, the final single BH solution was found by addressing the spacetime of a charged, spinning BH [56]. This would be known as the Kerr-Newman metric.

While solutions to the single BH can be found analytically, the two body problem is a different story and requires a numerical solution. The first step towards developing a numerical solution to Einstein's equations is to express them as an initial value problem. In 1962, Richard Arnowitt, Stanley Deser, and Charles W. Misner found a way to decompose

the 4-dimensional spacetime described by Einstein into 3 spatial dimensions and one time dimension, i.e. a 3+1 decomposition referred to as the ADM formalism [57]. When the ADM formalism proved to not be well posed, a modified version was introduced, frequently referred to as the BSSN formalism [58, 59, 60, 61].

2.1 3+1 Decomposition

The (3+1)-decomposition of Einstein's equations was the basis for the initial value problem. Here, I will briefly go though its form and key equations as laid out in Baumgarte and Shapiro [61]. Note, I will use abstract index notation, with repeated indices being summed over.

First, the four dimensional spacetime must be split into 3 spatial coordinates and one time coordinate. Define a space-like hypersurface with constant time $\Sigma(t)$ with spatial metric:

$$dl^2 = \gamma_{ij} dx^i dx^j . \tag{2.3}$$

At a given point P on $\Sigma(t)$, there is a normal vector which will intersect another hypersurface $\Sigma(t + \Delta t)$ at P'. The proper distance between P and P' is proportional to Δt with the proportionality variable (α) being referred to as the *lapse function*. Similarly, a line passing through P in such a way that the spatial coordinates are constant would intersect $\Sigma(t + \Delta t)$ at P''. The distance from P' to P'' would be a spatial vector also proportional to Δt, with the proportionality variable (β^i) being referred to as the *shift vector*.

Without going through all the steps, this leads to the four dimensional metric

$$ds^2 = -\alpha^2 dt^2 + \gamma_{ij}(dx^i + \beta^i dt)(dx^j + \beta^j dt) . \tag{2.4}$$

We can then define the extrinsic curvature

$$\frac{d}{dt}\gamma_{ij} = -2\alpha K_{ij} \tag{2.5}$$

with $\frac{d}{dt} = \frac{\partial}{\partial t} - \mathcal{L}_\beta$ where $\mathcal{L}$ is the Lie derivative. We also have the matter sources defined as:

$$\rho = n_\alpha n_\beta T^{\alpha\beta}\,, \tag{2.6}$$

$$S_i = -\gamma_{i\alpha} n_\beta T^{\alpha\beta}\,, \tag{2.7}$$

$$S_{ij} = \gamma_{i\alpha}\gamma_{j\beta} T^{\alpha\beta}\,, \tag{2.8}$$

$$M_{ij} \equiv S_{ij} + \frac{1}{2}\gamma_{ij}(\rho - S)\,, \tag{2.9}$$

where $S = \gamma^{ij} S_{ij}$.

The ten Einstein equations can then be rewritten into four constraint equations and six evolution equations. The constraint equations are given by the Hamiltonian constraint

$$R - K_{ij}K^{ij} + K^2 = 2\rho\,, \tag{2.10}$$

and the momentum constraint

$$D_j K^j{}_i - D_i K = S_i\,. \tag{2.11}$$

For the evolution equations, we have the evolution of the extrinsic curvature (which comes from the spatial metric)

$$\frac{d}{dt}K_{ij} = -D_i D_j \alpha + \alpha(R_{ij} - 2K_{il}K^l_j + K K_{ij} - M_{ij})\,. \tag{2.12}$$

where D_i is the covariant derivative associated with γ_{ij}. R_{ij} is the Ricci tensor associated with the spatial metric and is expressible as

$$R_{ij} = \frac{1}{2}\gamma^{kl}\left(\gamma_{kj,il} + \gamma_{il,kj} - \gamma_{kl,ij} - \gamma_{ij,kl}\right) + \gamma^{kl}\left(\Gamma^m_{il}\Gamma_{mkj} - \Gamma^m_{ij}\Gamma_{mkl}\right)\,. \tag{2.13}$$

There are ten second time derivatives required for the evolution of the system but only six evolution equations. This is as expected due to the four degrees of freedom associated with our choice of coordinates, specified by our choice of lapse and shift functions.

With this new formalism, scientists began solving more complex systems computationally. One of the most significant developments came in 1977, when Larry Smarr performed a head-on BH collision [62]. NR began to take off, but there were complications; the simulations built with ADM were often unstable, and it was unclear whether the instability was an intrinsic problem with the formalism itself or an external issue resulting from its implementation.

It wasn't until the 1990's when Shibata and Nakamura modified the ADM formalism, and Baumgarte and Shapiro established the increased stability, that numerically stable simulations became possible [58, 59, 60].

Takashi Nakamura, Kenichi Oobara, and Yasufumi Korjima presented a summary of their work in NR and gravitational radiation as part of the Kyoto group in 1987. They end their paper by saying:

> "We can estimate the energy flux for low amplitude case within an error of a few per cent. This opens the possibility of constructing a fully general relativistic code in which we can simulate any problems in numerical relativity."

Shibata and Nakamura published a paper later in 1995, in which they describe this formalism more completely [59].

The general idea behind their decomposition is to evolve a conformal factor and the trace of the extrinsic curvature independently. This decomposition naturally separates radiative and nonradiative variables. Let's briefly explore the form that this decomposition takes.

They begin by introducing a conformal metric

$$\tilde{\gamma}_{ij} = exp(-4\phi)\gamma_{ij} \tag{2.14}$$

with $det(\tilde{\gamma}_{ij})$ defined to be unity. They also define the trace-free part of the extrinsic curvature as

$$\tilde{A}_{ij} \equiv exp(-4\phi)\left(K_{ij} - \frac{1}{3}\gamma_{ij}K\right). \tag{2.15}$$

The evolution equations are then rewritten for these variables as

$$\frac{d}{dt}\tilde{\gamma}_{ij} = -2\alpha\tilde{A}_{ij} + \tilde{\gamma}_{il}\frac{\partial\beta^l}{\partial x^j} + \tilde{\gamma}_{jl}\frac{\partial\beta^l}{\partial x^i} - \frac{2}{3}\tilde{\gamma}_{ij}\frac{\partial\beta^l}{\partial x^l}, \tag{2.16}$$

$$\begin{aligned}\frac{d}{dt}\tilde{A}_{ij} = exp(-4\phi)\left[\alpha\left(R_{ij} - \frac{1}{3}\gamma_{ij}R\right) - \left(D_iD_j\alpha - \frac{1}{3}\gamma_{ij}D^kD_k\alpha\right)\right] \\ + \alpha\left(K\tilde{A}_{ij} - 2\tilde{A}_{il}\tilde{A}^l_j\right) + \frac{\partial\beta^m}{\partial x^i}\tilde{A}_{mj} + \frac{\partial^m}{\partial x^j}\tilde{A}_{mi} + \frac{2}{3}\frac{\partial\beta^m}{\partial x^m}\tilde{A}_{ij},\end{aligned} \tag{2.17}$$

$$\frac{d}{dt}\phi = \frac{1}{6}\left(-\alpha K + \frac{\partial\beta^i}{\partial x^i}\right), \tag{2.18}$$

$$\frac{d}{dt}K = \alpha\left(\tilde{A}_{ij}\tilde{A}^{ij} + \frac{1}{3}K^2\right) - D^iD_i\alpha, \tag{2.19}$$

where D is the covariant derivative with respect to γ_{ij} and

$$\frac{d}{dt} = \frac{\partial}{\partial t} - \beta^i\frac{\partial}{\partial x^i}. \tag{2.20}$$

Next the Ricci tensor can be split into two parts

$$R_{ij} = \tilde{R}_{ij} + R^{\phi}_{ij} \tag{2.21}$$

so that $\tilde{R}_{ij}$ is the Ricci tensor with respect to $\tilde{\gamma}_{ij}$ and

$$R^{\phi}_{ij} = -2\tilde{D}_i\tilde{D}_j\phi - 1\tilde{\gamma}_{ij}\tilde{D}^k\tilde{D}_k\phi + 4\left(\tilde{D}_i\phi\right)\left(\tilde{D}_j\phi\right) - 4\tilde{\gamma}_{ij}\left(\tilde{D}_k\phi\right)\left(\tilde{D}^k\phi\right). \tag{2.22}$$

With $\tilde{\gamma}_{ij}$ expressed as a perturbation on flat space geometry as $\tilde{\gamma}_{ij} = \eta_{ij} + h_{ij}$, $\tilde{R}_{ij}$ can be written as

$$\tilde{R}_{ij} = \frac{1}{2}\left[h_{ij,kk} + h_{jl,li} + h_{il,lj} + f^{kl}_{,k}\left(h_{lj,i} + h_{li,j} - h_{ij,l}\right) + f^{kl}\left(h_{lj,ik} + h_{li,jk} - h_{ij,lk}\right)\right] - \tilde{\Gamma^{l}_{kj}}\tilde{\Gamma^{k}_{li}}, \quad (2.23)$$

where $,i$ is $\frac{\partial}{\partial x^i}$ and $\tilde{\Gamma^{k}_{ij}}$ are the Christoffel symbols associated with the conformal spatial metric. In this expression, the first term on the right hand side is the main part of the wave equation and the remaining terms are the nonlinear or gauge terms.

As described in the ADM section, hypersurfaces are defined and stitched together using the lapse and shift functions. Depending on how you slice your spacetime, those lapse and shift functions will be different. While there are a number of different ways to do such a slicing, and Shibata and Nakamura address a few in their 1995 paper, they settle on using harmonic slicing, such that

$$\alpha = \alpha_0(\mathbf{r})exp(6\phi), \quad (2.24)$$

with $\beta^i = 0$. We will discuss our gauge choices in a later section within this chapter.

Inspired by Shibata and Nakamura's work, in 1998 Thomas Baumgarte and Stuart Shapiro evolve small amplitude GWs to directly compare the performance of the original ADM equations with those developed by Shibata and Nakamura [60]. To compare the performance of the two sets of equations, they set up a linearized wave solution and construct a time-symmetric solution. They then evolve the system using a shift of zero, with both geodesic slicing ($\alpha = 1$) and harmonic slicing ($\alpha = e^{6\phi}$). Both ADM and BSSN performed better with harmonic slicing, but the BSSN equations proved to be more stable all around. Their study provided evidence that the instabilities associated with the ADM equations were likely intrinsic as opposed to an effect of boundary conditions. Numerical relativists continued improving the 3+1 formalism to create longer, more stable simulations [63, 64, 65, 66]. In 2005, Pretorius implemented a stable numerical code capable of

simulating the inspiral and merger of BBH systems [67, 68]. One key feature in this new code was the selection of a gauge condition that slowed the "collapse" of the lapse and thus had strong singularity avoidance.

Proper evolution equations are exceedingly important but in order to use them, you have to set up your computational grid, define the initial data correctly, choose integration techniques, etc. There are several NR codes which have implemented these steps in various ways. Spectral Einstein Code (SpEC) is a NR code which uses multi-domain spectral methods to solve the partial differential equations which arise from the Einstein equations [69, 70, 71]. Their techniques have been very successful, allowing the accurate simulation of many orbits of inspiral [70, 71].

EINSTEINTOOLKIT is a finite-differencing NR code which has allowed for the simulation of many binary systems [72]. It is particularly well suited for the highly non-linear merger stage of the coalescence. Our code, MAYA, which I will discuss here is built upon EINSTEINTOOLKIT.

2.2 Einstein Toolkit / MAYA Code

EINSTEINTOOLKIT is a set of computational tools which performs simulations using the Baumgarte Shapiro Shibata Nakamura (BSSN) formalism [72]. It is based upon CACTUS and uses CARPET mesh refinement. It includes modules referred to as "thorns" which address the various aspects of the simulation as mentioned above. The MAYA code builds upon EINSTEINTOOLKIT with the addition of new thorns.

In the following sections, I will briefly discuss some of these thorns and their importance to the success of NR, focusing more on those thorns for which a thorough understanding is important for my work.

2.2.1 Initial Data

The premise behind the 3+1 decomposition of Einstein's equations is to create an initial value problem, thus allowing us to specify the data at some initial time and then evolve it into future time. Therefore, a crucial step is to set up the initial data on the initial hypersurface in such a way that it satisfies the given constraint equations.

To do so, we use the TWOPUNCTURES thorn, using the methods developed by Ansorg, Brugmann, and Tichy [73]. They develop solutions to the constraint equations for both single and binary BHs using a pseudo-spectral method. They begin with Brill-Lindquist topology which works on $\mathbb{R}^3$ with the two "punctures" excised, providing "inner asymptotically flat infinity". By analytically filling in the puncture points, they are able to remove the computational singularities, enabling them to map $\mathbb{R}^3$ to a single rectangular coordinate patch [73].

When discussing the initial data for two BHs, they consider two BHs placed symmetrically on the x-axis at $x = \pm b$ such that their initial separation is $D = 2b$. Their bare mass, linear momentum, and spins are denoted as $m_\pm$, $\mathbf{P}_\pm$, and $\mathbf{S}_\pm$ respectively [73].

They then must choose coordinates such that $r_\pm$ is regular at both punctures and the entire space maps to a single rectangular domain. Once this is established, they apply their single-domain spectral method to solve the Hamiltonian constraint. Refer to their paper for details on how they solve the constraints [73].

2.2.2 Mesh refinement

The foundation of any numerical simulation is the grid upon which it is built. For many simulated systems, merging BHs included, certain regions of the computational domain are changing more rapidly and dramatically than others. Thus, the most computationally efficient grid structure would be adaptive-mesh refinement (AMR), in which finer grids are added automatically throughout the simulation in places where it determines they are needed. However, the first step towards that is creating progressive mesh refinements for

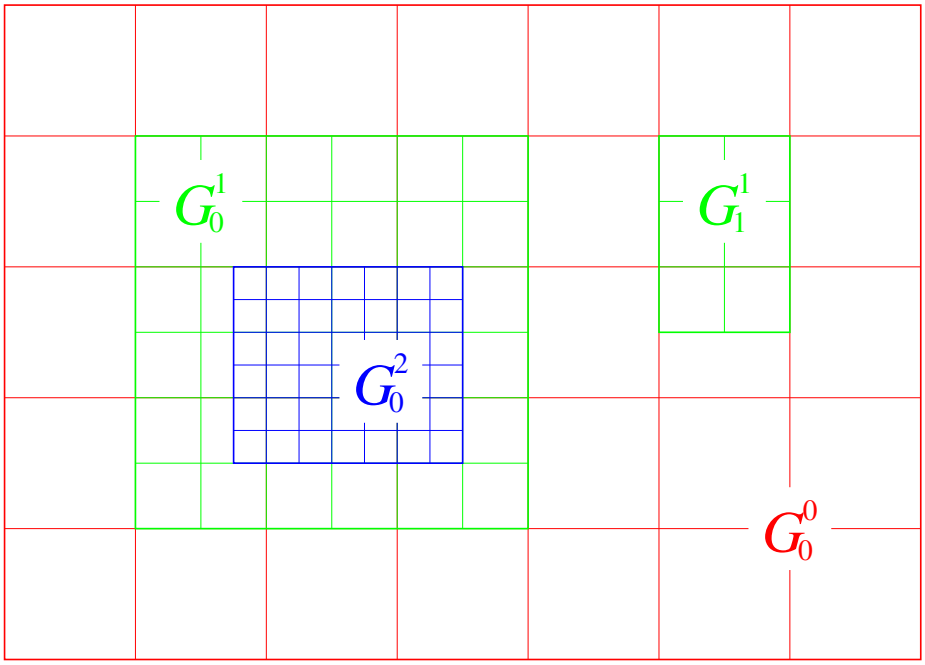

Figure 2.1: Minimal Berger-Oliger mesh refinement. Finer meshes fall entirely within the coarser grids, aligned in such a way that their boundaries fall on coarser grid lines. Image credit: [74].

full 3D simulations. The CARPET thorn provides this [74]. Rather than using a high resolution uniform grid, CARPET creates nested grids of increasing resolution, allowing for the same accuracy with less computational resources. For our simulations, we increase the refinements about the center of mass with additional refinements around each individual BH.

The mesh refinement is based on the minimal Berger-Oliger approach [75], a simplified version of the Berger-Oliger design. It makes use of a set of rectangular grids, arranged such that the grid boundaries are aligned with the grid lines of coarser levels. It uses a a constant refinement ratio between each of the levels, with coarse grid points coinciding with the fine grid points where they exist.

Figure 2.1 shows this structure. The full grid structure is made up of k refinement levels denoted as L^k, each of which contains some number of grids, G_j^k. The L^0 refinement level spans the full computational domain. The spacing between points within a grid is specified by Δx^k such that $\Delta x^k = \Delta x^{k-1}/N_{refine}$, where N_{refine} is a constant refinement factor.

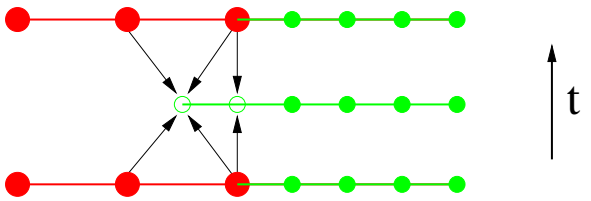

Figure 2.2: Time evolution scheme designed such that coarse grids can provide boundary conditions for the evolution of finer grids. Red points denote the coarse grid while filled green points denote the finer grid. The open green circles show the interpolated boundaries obtained from the coarse grid's data. Image credit: [74].

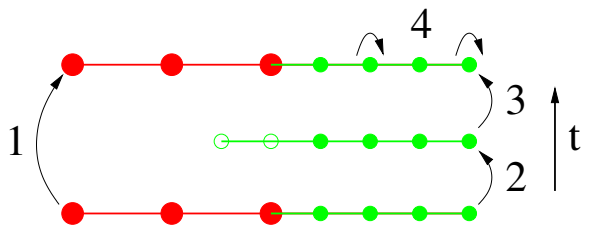

Figure 2.3: Time evolution scheme shown in four steps. 1) The coarse grid steps forward one time step. 2) and 3) the fine grid steps forward N_{refine} time steps to arrive at the same time as the coarse grid. 4) Data is copied from the fine grid to the coarse grid. Image credit: [74].

Once the grid structure is established, the simulation must be able to iterate through timesteps as well. CARPET utilizes the Berger and Oliger AMR time evolution scheme. The general idea behind it is to evolve the coarse grid one timestep before evolving the finer grids. The coarse grid can then be used to provide Dirichlet boundary conditions for the smaller grids by performing an interpolation in time and space. The refinement factor N_{refine} specified for the spatial grid necessitates that the time steps are also smaller for the finer grids by a factor of N_{refine}. Figure 2.2 shows how the data from the coarse grid can be used to provide the boundary conditions for the evolution of the finer grids [74].

After the coarse and fine refinement levels have been evolved one coarse timestep (N_{refine} steps for the finer level), the data is copied from the finer grid to the coarser grid at points they share. This ensures consistency and accuracy and occurs recursively from the finest to the coarsest mesh. Figure 2.3 shows each of these steps [74].

For simple integration methods, the boundary conditions can be applied once per time step. However, we use Runge-Kutta integration, which necessitates that the fine grid bound-

ary conditions be applied multiple times.

The initial data for the simulation is set up recursively from the coarsest grid down to the finest. The data from the finer grids is then copied to the coarser grids where they coincide. However, for higher order time integration, one may need initial data at several time levels. One solution is to use lower order integration and interpolation at the beginning of the simulation.

Another solution, the one used in CARPET, is to evolve the coarse grid backwards in time one step and forwards in time one step, and then evolve the finer grids recursively. Since the initial data is required to precede $t = 0$, one additional step backwards is necessary. The simulation can then proceed without any modification to the integration at early times [74].

2.2.3 Gauge conditions

The gauge conditions specify how you slice the spacetime and evolve through it, by providing equations for the lapse α and the shift β^i. The lapse defines how the spatial slices, Σ, are chosen, and the shift defines the coordinates on the spatial slices. An appropriate gauge condition is necessary for performing long, stable evolutions. We make use of the puncture gauge conditions [76, 77, 78, 66].

For our slicing condition, we use a modified Bona-Masso slicing condition which is often referred to as "1+log" slicing, where α obeys

$$\partial_0 \alpha = -2\alpha K \,. \tag{2.25}$$

It is named as such because the analytic solution to the lapse is of the form "1+log".

We use a modified Gamma-driver shift condition to define β^i:

$$\partial_0 \beta^i = \xi B^i \tag{2.26}$$

$$\partial_0 B^i = \partial_0 \tilde{\Gamma}^i - \eta B^i \,, \tag{2.27}$$

where $\partial_0 = \partial_t - \beta^i \partial_i$.

This gauge condition has strong sigularity avoidance; the lapse going to near zero around the puncture causes the proper time to move more slowly.

In addition to defining the coordinate system the simulation is evolving in, the gauge condition is also used by SHIFTTRACKER to track the puncture. It does so making use of

$$\frac{dx^i}{dt} = -\beta^i \,. \tag{2.28}$$

2.2.4 Waveform Extraction

One of the main purposes of performing NR BBH simulations is to predict the gravitational radiation that would be observed by a detector such as LIGO. This gravitational radiation can be understood from the Weyl tensor, $C_{\alpha\beta\gamma\delta}$, which is the completely antisymmetric Riemann curvature tensor. We can compute the -2 spin weighted pseudoscalar referred to as the Weyl scalar, Ψ_4, from the Weyl tensor once we choose an appropriate null tetrad consisting of four basis vectors, $\{l^\mu, n^\mu, m^\mu, \bar{m}^\mu\}$:

$$\Psi_4 = C_{\alpha\beta\gamma\delta} \mathbf{l}^\alpha, \mathbf{n}^\beta, \mathbf{m}^\gamma, \bar{\mathbf{m}}^\delta \,. \tag{2.29}$$

Ψ_4 can be expressed in terms of the spin-weighted spherical harmonics, ${}_sY_{\ell m}$ [79, 80], with $s = -2$. The amplitudes which serve as the coefficients for each of the spherical harmonics can be computed as

$$C_{\ell m}(t, r) = \oint \Psi_{4-2} \bar{Y}_{\ell m}(\theta, \phi) d\Omega \,. \tag{2.30}$$

This representation allows the GW data to be expressed on spheres as amplitudes associated with each ℓ, m pair with angular independence. It can then be reconstructed in a particular location using the spherical harmonics and the desired angular coordinates as

$$\Psi_4 = \sum_{\ell=2}^{\infty} \sum_{m=-\ell}^{\ell} C_{\ell m}(t,r)_{-2}Y_{\ell m}(\theta,\phi)\,. \tag{2.31}$$

Two thorns, WEYLSCAL4 and YLMDECOMP are used to compute the gravitational radiation. First, WEYLSCAL4 computes the values of Ψ_4 at each of the points within the domain, and then YLMDECOMP interpolates Ψ_4 onto concentric spheres of various radii. We desire the gravitational radiation at infinite radius, but are limited by our finite grid size. Therefore, we use the values Ψ_4 computed by YLMDECOMP on spheres of finite radius and extrapolate to obtain the radiation at infinity [81]. This introduces a potential source of error, and requires careful choice of extraction radius. We typically choose $r = 75M$ as it is a reasonable distance from both the BHs and the boundary of the grid.

2.2.5 Apparent Horizon Finder

One of the additional challenges in NR is defining the boundary of a BH. Traditionally in GR, one talks about the event horizon, the boundary from within which nothing can escape to spatial and temporal infinity. However, in NR, this definition would be extremely computationally intensive and impractical. Instead, numerical relativists tend to track MOTS, closed two-surfaces with outgoing expansion of zero:

$$\Theta \equiv \nabla_i n^i + K_{ij} n^i n^j - K = 0, \tag{2.32}$$

where K_{ij} is the extrinsic curvature of the slice and n^i are the normal vectors.

The outermost MOTS is known as the AH and provides information about the mass and spin of the BH. The AH is defined on each spatial slice and, if it exists, is guaranteed to lie within the event horizon. While these AHs are gauge dependent, tracking them through

the merger may provide information about the way the common horizon forms and how it settles down to an isolated state. Similarly, tracking the MOTS which may exist within the common AH could potentially reveal information about the spacetime structure within a BH. To find the AH of BHs during a NR simulation, we use Thornburg's AHFINDERDIRECT [82], which solves Eq. 2.32 numerically.

AHFINDERDIRECT assumes the horizon is a "star-shaped region", meaning the surface can be expressed as $r = h(angle)$. This gives a nonlinear elliptical PDE in h on S^2 with coefficients that are algebraic functions of g_{ij}, its spatial derivatives, and K_{ij}. The surface is broken into individual overlapping angular patches. One quadrant is shown in Figure 2.4. The code uses 4th order angular finite differencing and uses Newton's method with "symbolic differentiation" to compute the Jacobian matrix and find the desired MOTS. The algorithm considers a surface to have been found if the ∞-norm of $\{\Theta_{\rm I}\}$ is below a given threshold (10^{-8} by default).

Using N_{ang} angular grid points provides a set of N_{ang} nonlinear algebraic equations for the values of h. Therefore, it uses Newton's method in N_{ang} dimensions. The AHFinderDirect algorithm uses 4 steps to find the horizon:

- Newton's method iteration,
- computation of the expansion $\{\Theta_{\rm I}\}$ given a trial surface $\{h_{\rm I}\}$,
- computation of the Jacobian matrix $\mathbf{J}_{\rm IJ} \equiv d\Theta_{\rm I}/dh_{\rm J}$ given a trial surface $\{h_{\rm I}\}$,
- solving the updating equation $\mathbf{J} \cdot \delta h = -\Theta$.

Much more detail on the algorithm can be found in Thornburg's paper which describes AHFinderDirect [82].

2.3 Performing MAYA Numerical Relativity Simulations

With a base understanding of the thorns established, it's important to detail how to perform a NR simulation, beginning with how to choose the initial parameters and ending with how

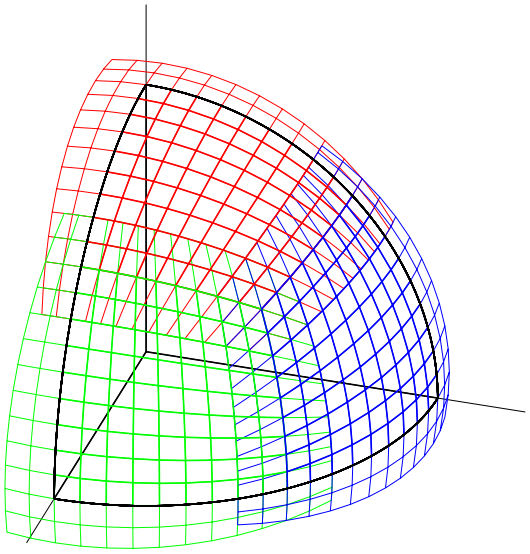

Figure 2.4: AHFINDERDIRECT angular patches overlapping to cover one quadrant. Image credit: [82].

to perform post-processing analysis.

2.3.1 Initial Parameters

A BBH system can be fully described by 9 parameters: two masses (m_1 and m_2), two spin vectors ($\mathbf{S_1}$ and $\mathbf{S_2}$), and the eccentricity of the orbit (ϵ). Since everything about the BBH system can be scaled according to the total mass, we reduce the dimensionality by constraining $m_1 + m_2 = 1$. Therefore we replace m_1 and m_2 with the mass ratio $q = m_1/m_2 > 1$. MAYA uses geometric units ($c = G = 1$), so length and time are both are both in units of M .

Once you choose the 8 parameters you want to describe your BBH system, there are a few steps to turn them into NR initial data. Typically, we create a `rpar` file which can then either generate a `.par` file or can be used directly with the MAYA code. The `rpar` file allows for calculations to be performed within the file, rather than requiring everything to be hard-coded. I will briefly go through the steps to create a `rpar` file for a simulation.

While the 8 parameters listed above may fully describe a BBH system, NR simulations begin at a finite separation and require the initial positions and momentums in addition to the aforementioned parameters. To help compute these parameters, particularly when trying to create a quasi-circular orbit ($\epsilon = 0$), we begin with the BHs at a large separation and then evolve them using PN evolution until we reach the desired separation to begin our NR simulation. This provides us with the linear momenta, the positions, and the spins to use at the beginning of our simulation. Our in-house script for performing the PN evolution is called PNevo and was written by Jim Healy. The orbits during PNevo and the NR simulation are shown in Figure 2.5. The PN evolution starts at a larger separation than shown in this figure.

After determining the initial momenta, spins, and positions for the simulation, we use the MAYA initial data solver (BAUM) to find the initial bare masses. The BAUM thorn is part of the MAYA code, and therefore requires you to have a valid build of MAYA in order to

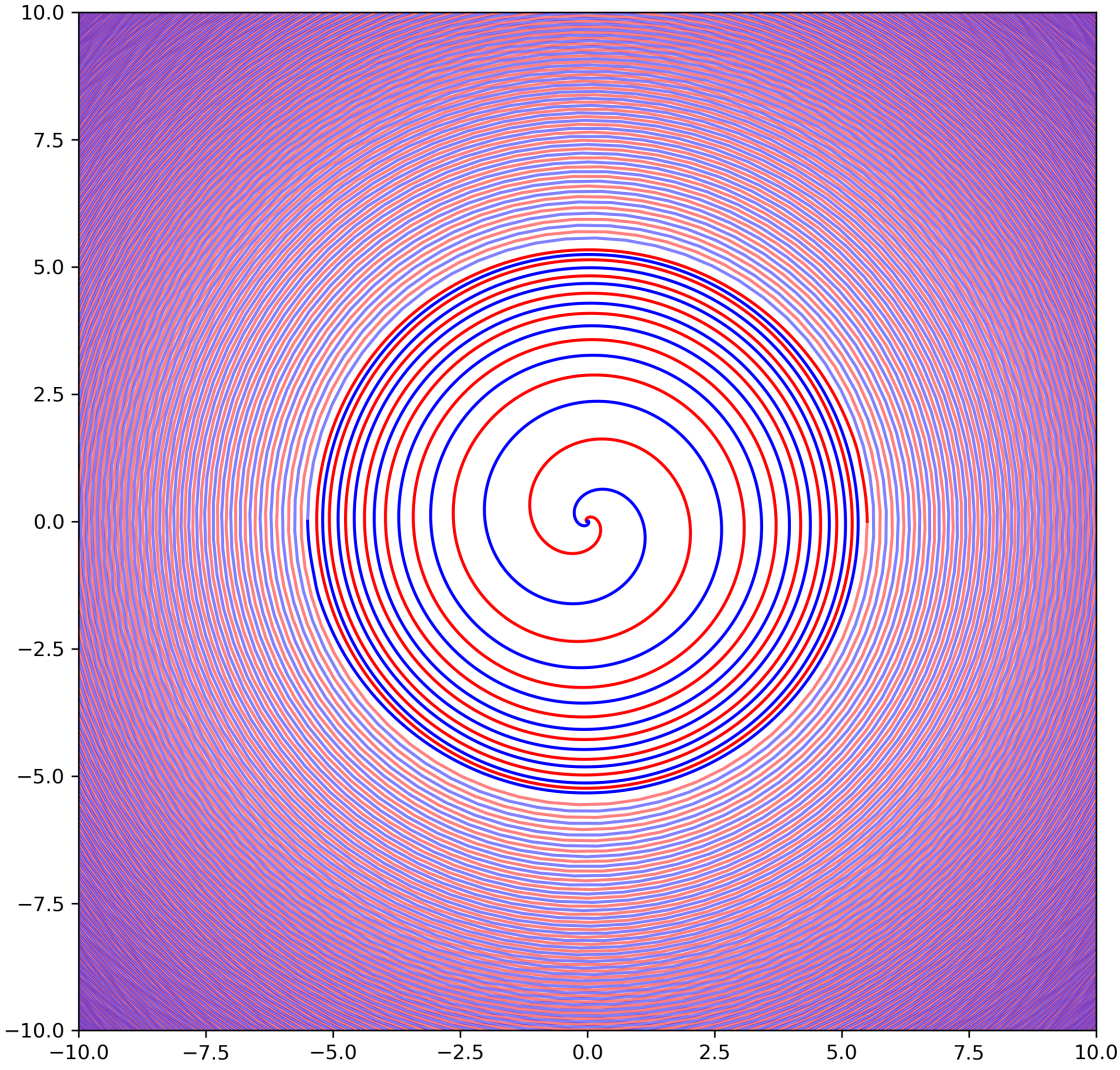

Figure 2.5: BBH orbits from Post-Newtonian evolution and NR. The lighter red and blue show the end of the Post-Netwonian orbit and the dark red and blue show the NR orbits.

solve for the bare masses. Jim Healy wrote a script called `CreateRparFromPNevo.sh` which takes the output of PNevo, runs it through the Baum solver, and then combines the result with a provided template rpar file to create a usable parameter file for the simulation. The Baum solver uses an iterative process to take the desired momentums, spins, separation, and mass ratio and compute the bare masses for the initial BHs. This is the required input for the TWOPUNCTURES initial data thorn.

2.3.2 Grid Structure

The previous section describes how to generate a working parameter file based upon the initial parameters you desire. However, it relies upon having a template `rpar` file which already sets most of the parameters for the simulation. There are a number of reliable `rpar` templates the group has set up over the years, but it is likely that for various simulations they will need to be modified. One of the most frequently made changes is the grid structure.

As described earlier in the mesh refinement section, MAYA simulations run on a set of nested grids of increasing resolution. Properly choosing the number of refinement levels, the spacing, and the radii of the grids is critically important for the accuracy and efficiency of the simulation.

The desired grid structure is heavily dependent upon the mass ratio. The accuracy with which we can assess the spacetime around the individual BHs depends on the number of points across the horizon. For computational efficiency, that finest grid only needs to extend a small range outside the BH, and the radius of the smallest refinement should be set to be slightly larger than the radius of the smallest BH.

Typically we use 10 or 11 refinement levels with the resolution increasing by a factor of two at each level. The coarsest $\sim$4 are centered at the origin, which will be the location of the final BH. The remaining refinement levels have grids for the individual BHs. It is possible to only have a grid for one of the BHs, e.g. having extra refinement grids for only the smaller BH in order to improve computational efficiency.

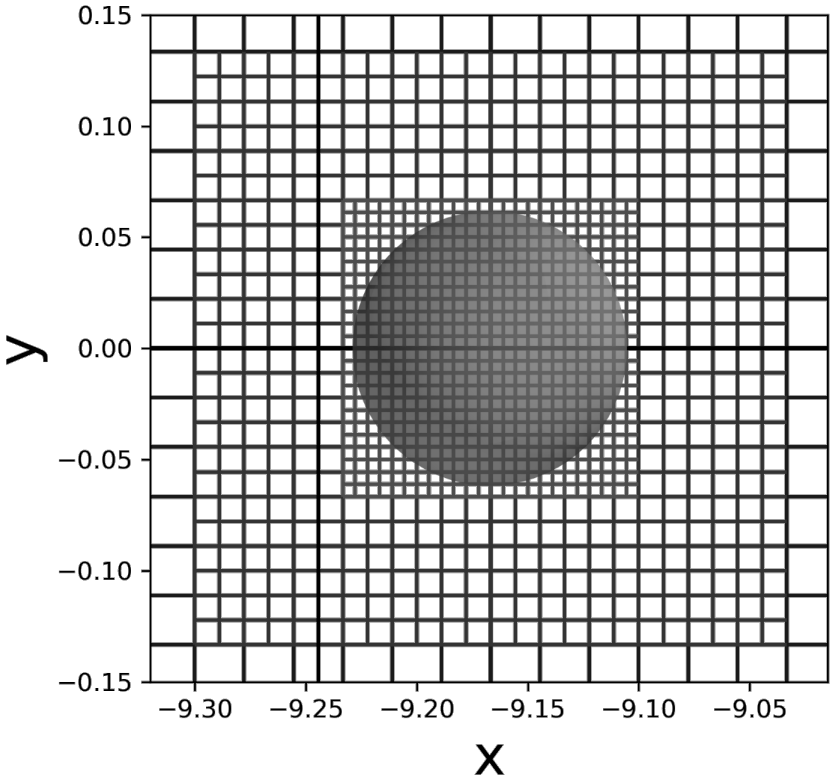

Figure 2.6: Subsection of the grid structure for a BBH simulation. The finest mesh extends just beyond the AH of the BH.

The number of points necessary across the finest grid depends on your use case. Any finite resolution waveform will have errors associated with it due to the discretization, but higher resolution grids will have lower error. In Chapter 5, I present an equation for the necessary grid resolution as a function of the signal-to-noise ratio of a GW signal. Typically, we select the grid resolution such that we have at least 24 points across the smaller BH, but we often go much higher. A section of this grid structure can be seen in Figure 2.6 which shows the region around one of the BHs.

After setting up the parameter file, you need to decide what computational resources the simulation will require. Based upon the grid structure, the `rpar` files can provide an estimate of the memory requirements. Look at the memory per node on the cluster you are using and then request a number of nodes accordingly. The standard output file of

the simulation will also print the required memory. This measure will be more accurate than the estimate provided by the `rpar` file, so it is a good habit to check the memory requirements after beginning the simulation as well.

2.3.3 Post-processing Analysis

After performing a simulation and copying the data to a local machine, there are a number of useful tools to analyze the data. One such tool is Runview, a python script written by Bhavesh Khamesra. The two main purposes of Runview are to 1) stitch together all the output folders and 2) create plots of the most frequently desired quantities and create an HTML file to display them.

When we perform simulations on clusters, we typically ask for time in 24 or 48 hour segments. Because MAYA checkpoints periodically, we can resume our runs after they stop. This leaves our simulation data broken into many numbered output folders. Stitching all these together is an important first step for performing analysis.

Runview's visualization capabilities are also quite useful for analyzing a simulation. It can plot the Ψ_4 data as a function of time, the trajectories, etc. This step may be the final step of your analysis, or it may form a useful status check to make sure the simulation looks correct.

There is also a set of Matlab scripts referred to in house as the Healy Toolkit, which provides further data analysis capabilities. The typical workflow when using the Healy Toolkit is to first create a modeBundle object which gathers all the relevant data for each ℓ, m mode from the simulation. From there we clean the Ψ_4 data. Ideally, we are simulating compact binary systems which began with infinite separation at rest. However, we must begin the simulations at a finite separation with specified values of momentum, and must establish the initial data on the spatial slice at this initial time. This leads to nonphysical radiation for the first $\approx 20\,\mathrm{M}$, so we remove the beginning of the simulation to cut off this nonphysical radiation and then taper the waveform to zero. Next, since we extract the

gravitational radiation at a finite radius, we generally extrapolate it to infinite radius [81]. Various quantities such as the energy radiated can be computed at this point. Our NR simulations naturally output the Weyl scalar (ψ_4), but in order for it to be of use with detector data, we require the gravitational strain (h), the second integral of ψ_4 with respect to time:

$$h(t) = h_+(t) - ih_\times(t) = \int_{-\infty}^{t} dt' \int_{-\infty}^{t'} dt'' \psi_4(t'') \,. \tag{2.33}$$

The Healy Toolkit can be used to perform this conversion. The strain can then be output into ascii files for future use, or can be used within the script to compute quantities such as SNR.

A general overview of our NR workflow is shown in Figure 2.7, though I have also written additional post-processing analysis tools which I will discuss in Chapter 3.

With the NR infrastructure set up, we have the ability to simulate the coalescence of BBH systems. These simulations allow us to see precisely how spacetime behaves if Einstein's theory of GR is correct. This enables us to create template waveforms which can be used with the detectors and analysis techniques described in Chapter 1.

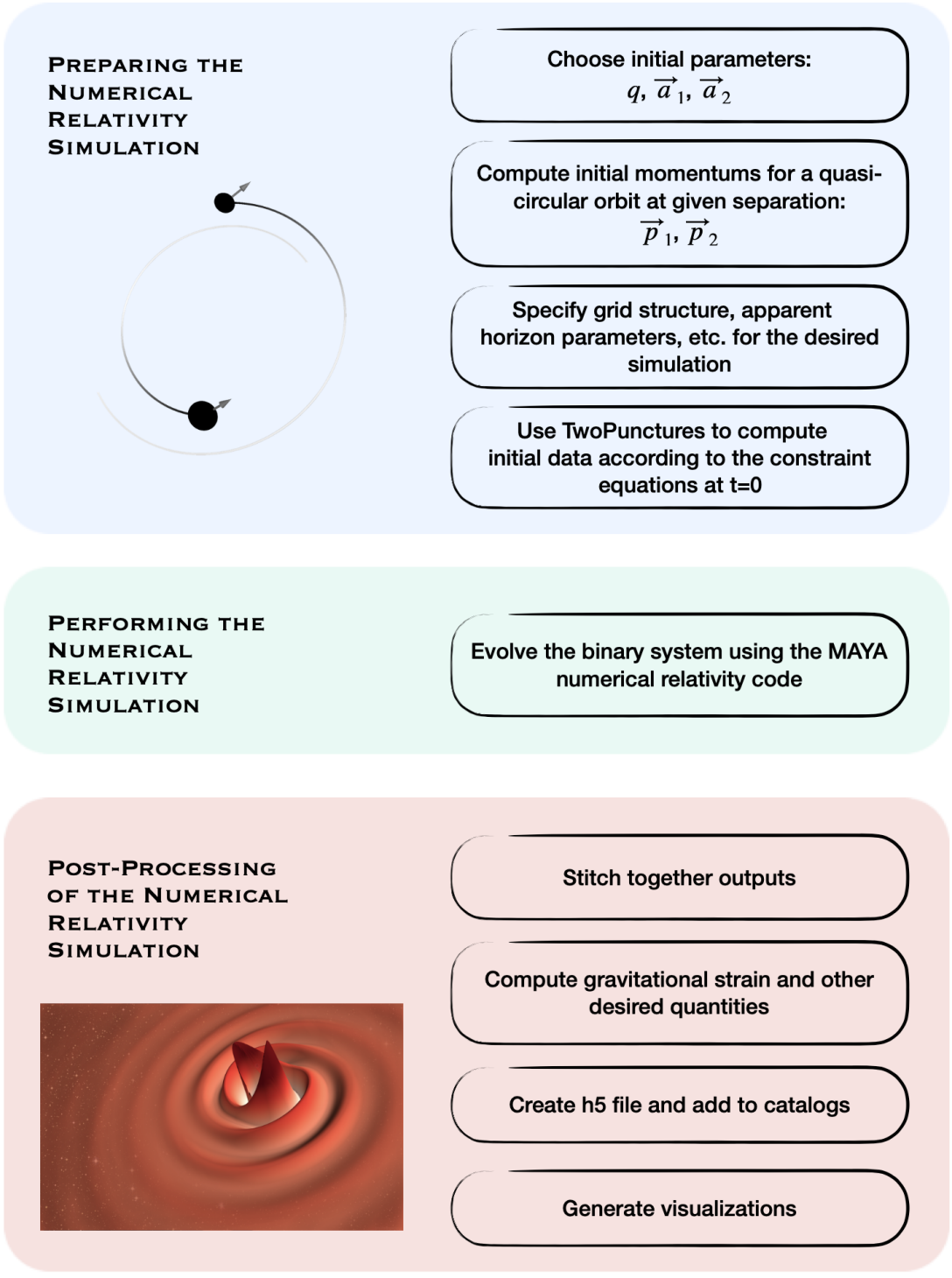

Figure 2.7: Workflow to create a catalog-ready waveform. In blue are the steps to set up the desired NR simulation. In green are the steps involved with the actual running of the simulation. In red are the post-processing steps.

CHAPTER 3

INFRASTRUCTURE

Most of our work involves the production of new NR simulations or the analysis of existing simulations. These both require extensive infrastructure built around our MAYA code. I have worked to improve this infrastructure both to simplify our current tools to make them easier and faster to use and to expand our analysis capabilities. This improved infrastructure allows us to more rapidly and correctly create new NR waveforms, for in house use, to add to the LVC catalog, and to add to our public catalog.

One of my roles has been maintaining and improving our NR catalog including cleaning up our scripts to generate LVC compatible waveforms, cleaning up the public catalog, introducing new runs to both catalogs, and improving the testing of our simulations. I have also generated a number of scripts to improve and automate the generation of simulation parameter files. I've written additional analysis tools, particularly focusing on computing the match between waveforms. In order to better study the AHs that exist during a simulation, I have also made modifications to the AHFINDERDIRECT thorn. Finally, I have created a visualization tool to generate animations of the AHs and Ψ_4 data of our simulations.

3.1 Numerical Relativity Catalog

Part of our group's role within the LIGO Scientific Collaboration (LSC) is to provide NR waveforms to be used for data analysis as well as in the training of models. The waveforms provided by all the NR groups are stored within the LVC NR catalog as `h5` files [83]. In addition to contributing to this LVC NR catalog, we also maintain a public catalog currently hosted at http://www.einstein.gatech.edu. In our public catalog, we provide our waveforms in the same format as the LVC catalog, with the addition of extra metadata. There are many steps involved both in preparing a NR simulation and in the post-processing to produce the

gravitational radiation in the proper format.

First, one has to select the initial parameters that describe the desired binary system and then generate a parameter file, as described in Chapter 2. With the intent of simplifying the steps necessary to obtain a parameter file, I have first cleaned up our old "rpar bodies", skeleton `rpar` files to be used when creating various simulations. I've created a set of `rpar` bodies which are optimized for aligned spin, precessing spin, low mass ratio, and high mass ratio cases. I then created a script to take in a configuration file and not only automate the running of PNevo and CreateRparfromPNevo, but also select the appropriate `rpar` body and set up a reasonable grid structure. While doing these tasks by hand should be simple after having run multiple simulations, it can often be an unnecessarily complicated barrier of entry for new members. Eventually I would like to have the creation and running of new simulations be fully automated. This will take some time, as it requires selecting the initial parameters, creating the parameter file, submitting to a cluster, and monitoring the progress. However, automating the parameter file creation moves us one step closer towards that goal.

As described in Chapter 2, there are also numerous steps required to go from a raw NR simulation to a final `h5` file. I have worked to make this less complicated and more automated. As a temporary solution, I created a python script which runs each of the steps in turn. The user provides a configuration file which tells the script where the initial simulation is and where to store the final `h5` file as well as any desired intermediate data. The script then takes the raw simulation data and automatically creates the catalog-ready `h5` file.

I have also been working on rewriting our scripts in easy-to-use Jupyter notebooks to do all the required postprocessing on a NR simulation. The notebooks include individual functions to compute the strain as well as to generate the `h5` files. My goal is to create a toolkit and workflow that is easy enough that any new group member can analyze and prepare their raw simulation for entry into the catalog. This is an ongoing task that will

likely continue into my post-doctoral career.

The final step in preparing catalog waveforms is to thoroughly test them. When I took over maintenance of the catalog, one of the first challenges I tackled was an inconsistency in the value of initial frequency provided in the metadata. I found the problem to be caused by the time at which we were cropping the beginning of the waveform. We tapered our waveforms initially but the LVC NR infrastructure required all tapering to be removed. For many of our simulations, the cutoff time had been chosen to be too low, not removing all the tapering. This skewed the value of initial frequency enough to be problematic. Another challenge I faced was that a number of our waveforms had been previously rejected by the LVC NR tests. In investigating what caused some but not all waveforms to be rejected, I noticed an error in our spin metadata. Correcting these two issues allowed us to add many more waveforms to the LVC NR catalog which had previously been rejected. These issues highlighted the need to update our waveform test suite to be more thorough. With our improved `h5` generating scripts and improved test suite, we can be confident in the waveforms we are providing.

3.2 Data Analysis Tools

A significant portion of my work has involved data analysis of NR simulations, often analyses that span our entire catalog. Out of these tasks has come a suite of NR data analysis tools.

3.2.1 Frequency at Maximum Amplitude Computation

In Chapter 4, I will describe a method I created to identify the spin of the remnant BH using the instantaneous frequency and its derivative at the time of maximum amplitude. The relationship was found using NR waveforms, but the purpose is to apply it to detection data, without requiring a templated search. To do this, I used BW to recover the value of the instantaneous frequency and its derivative at maximum amplitude for each of the

posteriors.

This required modifying the BW post analysis scripts to compute the necessary quantities. I wrote four additional functions, the first three of which have been merged into the most recent version of BW. The first function, `get_time_domain_envelope`, computes the amplitude envelope from the real part of the waveform by shifting the frequency domain waveform by $\pi/2$ and then converting back to the time domain. This shifted waveform can be used with the original real part in order to compute the amplitude. The second function, `get_time_at_max`, uses the aforementioned function to identify the time at which the amplitude reaches a maximum. Next, `get_freq_at_max` computes the instantaneous frequency and identifies its value at the time obtained from the previous function. Similarly, `get_dfreq_at_max` computes the derivative of the instantaneous frequency and its value at the time of maximum amplitude.

The value of `t_at_max_amp` and `f_at_max_amp` have both been added as columns to the moments file, thus allowing their distribution across the draws from the posterior to be computed. The distribution of `f_at_max_amp` for an injected signal with SNR of 100 is shown in Figure 3.1.

3.2.2 Match Computation

As GW detections have become routine, we are increasingly confident in our ability to observe them and have become more concerned with improving our ability to characterize them. As future detectors come online, this will be even more important.

With this in mind, we often find ourselves asking some form of the question: "Are waveform A and waveform B distinguishable within a given detector?" This led me to create a Jupyter notebook to compute the match between any two NR waveforms as well as the signal SNR, and the SNR of the difference between the waveforms (the residual). The user creates a configuration file (an example `input.json` is included in the repository) to specify the details of the comparisons they require. The notebook then reads the specified

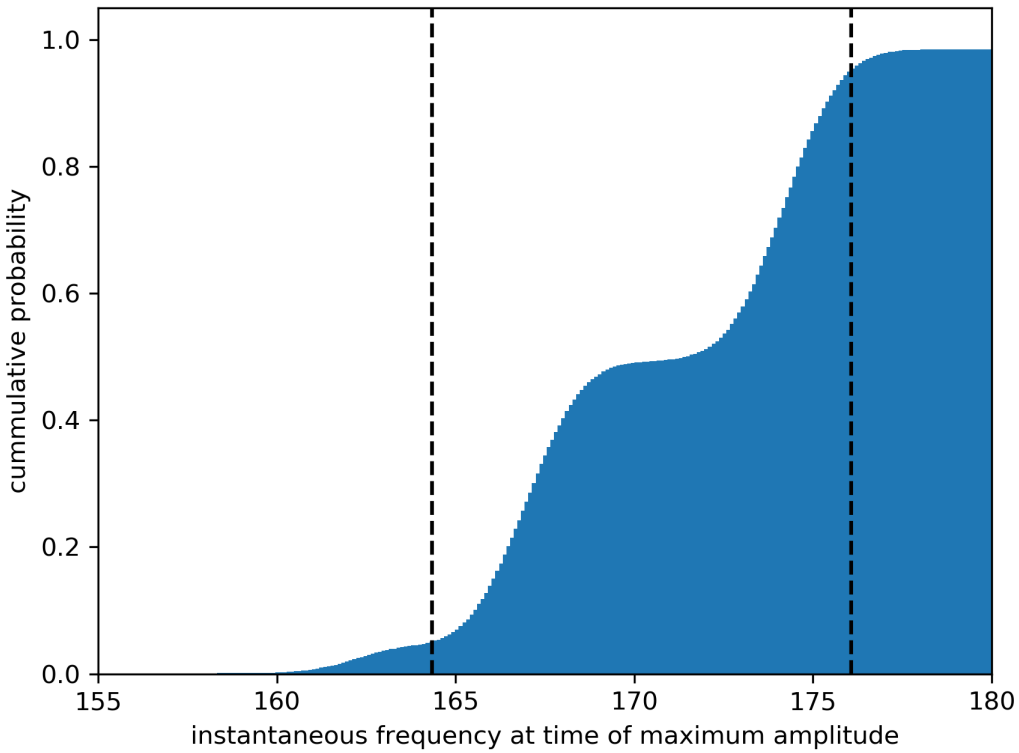

Figure 3.1: Distribution of the instantaneous frequency at the time of maximum amplitude from a BayesWave recovery performed on a NR injection with parameters consistent with GW190521.

waveforms and aligns them such that the overlap is maximized over time and phase. It then computes the mismatch and the residual between the two waveforms as well as the SNRs of both the signal and the residual. It also computes the signal SNR at which the residual SNR would be greater than one. This is saved in a text file for all configurations the user specified. For legibility purposes, I have reformatted an example `.txt` file into a table here.

Table 3.1: Example output from match computation Jupyter notebook. Generally output as a text file but currently reformatted as a table for ease of inclusion in this description.

mass	distance	detector	iota	phi	$modes_1$	$modes_2$	supplementary info	ρ_{signal}	ρ_{res}	mismatch (ϵ)	ρ where $\rho_{res} = 1$
300	1000	LIGO	0	0	[[2, 2], [3, 3], [4, 4]]	[[2, 2], [3, 3], [4, 4]]	all significant modes	172.111	0.727	0.000009	236.711
300	1000	ET	0	0	all	all	none	2217.037	38.988	0.000155	56.864
5000000	30000	LISA	0	0	all	all	none	3505.689	11.6056	0.000005	302.070

The user can also request that figures be generated showing the two specified waveforms and their residual with the noise curve of the desired detector. Figure 3.2 shows an example of such a plot. Additionally, the notebook can output text files containing the PSD of the detector and the frequency series and time series of the waveforms and residuals.

I created a second notebook to compare a given NR waveform with a model waveform, for any model supported by PyCBC. The configuration is very similar, but instead of providing a second `h5` file, the user provides the name of the model they would like to use. In the future, I will combine these two scripts into one, allowing the user to use either a model or NR for either waveform. The notebook is compatible with all waveforms in the LVC catalog and has contributed to several studies exploring what features of binary coalescences are observable by GW detectors. Details for how to set up the configuration file for this notebook can be seen in Appendix A.

3.3 Apparent Horizon Finder

When discussing BHs, it is often useful to consider their event horizons. Unfortunately, event horizons require evolution to spatial and temporal infinity in order to be identified, so

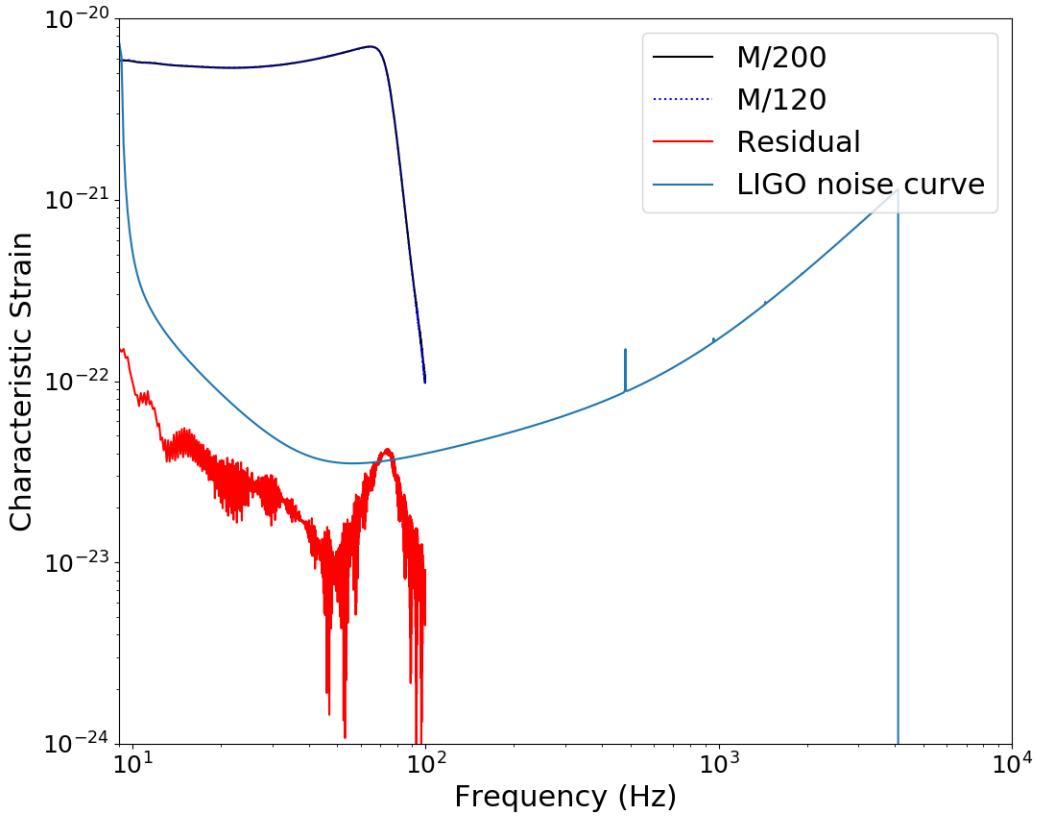

Figure 3.2: Characteristic strain for two waveforms of the same BBH system with different resolutions: $M/200$ (black) and $M/120$ (dotted blue). The red line shows the residual resulting from subtracting the lower resolution waveform from the higher resolution waveform. The LIGO noise curve is shown in light blue.

we replace them with the AH. If the AH exists on a given spatial slice, it is guaranteed to lie on or within the event horizon, and asymptotically becomes the event horizon in an isolated system when approaching infinite time. This makes AHs the preferred horizon to use with NR simulations. Once the common AH forms, no information from within the AH is able to escape. However, it is possible that the dynamics within the AH could be correlated with the radiation zone outside the AH. To begin exploring this possible relation, we were interested in understanding the behavior of the MOTSs that exist within the common AH once it has already formed [84]. Accomplishing this goal involved taking advantage of less frequently used features of `AHFinderDirect` as well as making some modifications to the thorn.

The common AH actually consists of two MOTSs, an inner and an outer MOTS. Since AHFINDERDIRECT aims to search for the outermost common AH, it takes some coercion to locate the inner common MOTS. By modifying the `shiftout` parameter to be less than one, I was able to locate the inner common MOTS. Locating each common MOTS as early as possible revealed that the inner and outer common MOTS begin at the same location and split, with the inner common MOTS shrinking and the outer common MOTS growing. This can be seen in Figure 3.3.

Unfortunately, as the simulation progressed, we had difficulty continuing to track the inner common MOTS. As can be seen in the later frames of Figure 3.3, as it shrinks, the inner common MOTS appears to become increasingly distorted, and eventually, AHFINDERDIRECT was no longer able to find a suitable surface. In order to investigate this, I modified the AHFINDERDIRECT thorn to output the trial surface at every iteration of the Newton search algorithm, a few timesteps of which are shown in Figure 3.4.

This revealed that the inability to find a suitable surface was due to the highly distorted nature of the surface. AHFINDERDIRECT assumes the AHs have a "star" shape, meaning that if one draws rays from the center of the AH outward, it should only intersect with the surface once. The inner common MOTS does not obey this at later times, causing

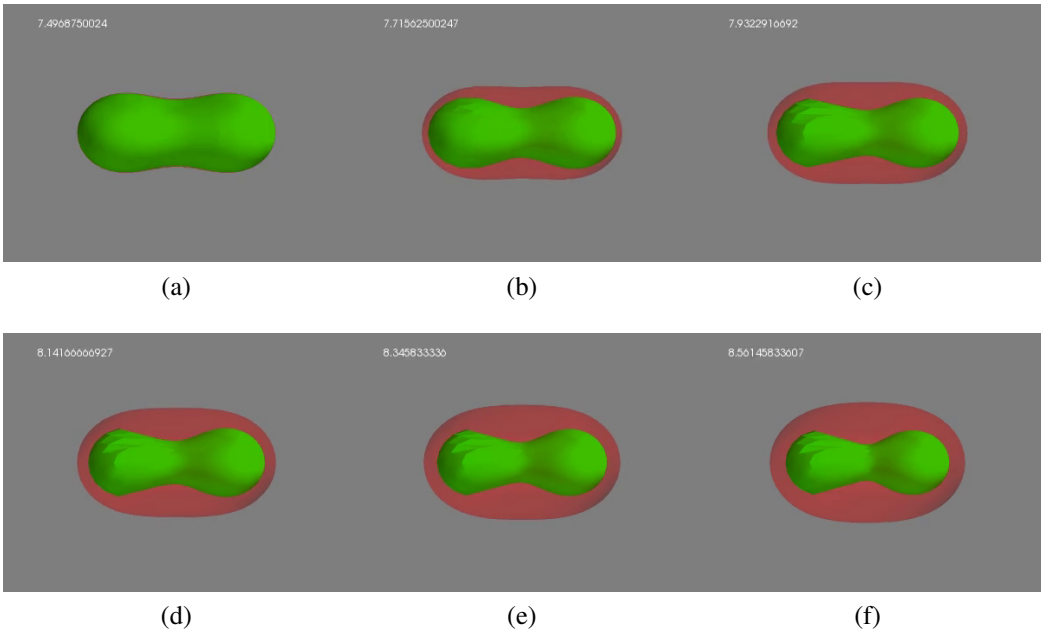

(a) (b) (c)

(d) (e) (f)

Figure 3.3: The evolution of the two MOTSs which make up the common AH.

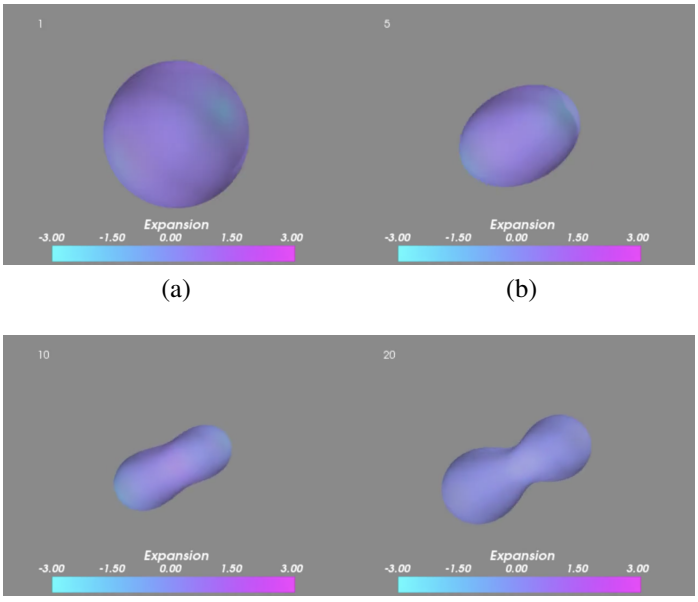

(a) (b)

(c) (d)

Figure 3.4: Trial surface at various iterations of the AHFINDERDIRECT search algorithm.

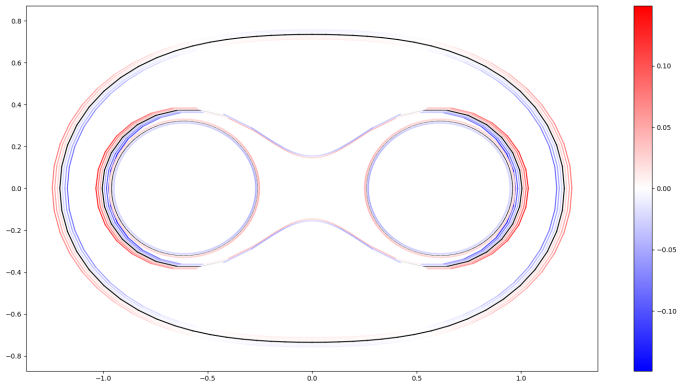

Figure 3.5: The value of the expansion along surfaces placed just outside and within the MOTSs in the xy-plane.

AHFINDERDIRECT to shift the center to create a more spherical AH, leaving one half of the surface severely under resolved. I was able to solve this by turning on reflection symmetry for the AH, allowing us allowing us to track the inner common AH for much longer as it approached the initial AHs.

We were also interested in exploring the value of the expansion throughout the space foliated by these MOTSs. Since the expansion is only defined with respect to a surface, I modified AHFINDERDIRECT to output the surfaces as well as their values of expansion just inside and outside the identified AHs, shown on the xy plane in Figure 3.5.

With these modifications, we were able to track the initial MOTS as well as the inner common MOTS for much longer than we were originally able to, enabling us to explore their evolution. These debugging modifications will likely be beneficial as we search for MOTS in other unique situations as well.

3.4 Visualization Tools

My work with AHFINDERDIRECT inspired my creation of a tool to plot the 3D AHs output by AHFINDERDIRECT. The Mayavi python plotting library provided me with useful functions to plot surfaces and meshes when provided with triangulated data points [85].

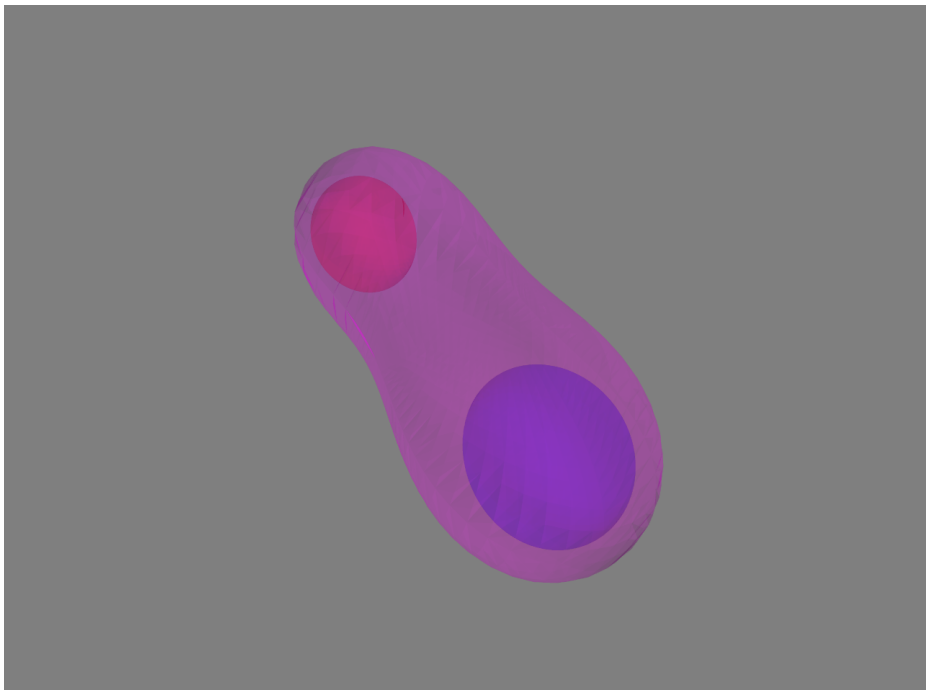

Figure 3.6: Inner common MOTS and initial MOTS during the merger of two BBHs.

The initial motivation for the tool was to observe the shape of the common AH as it formed around the initial AHs and then track how its shape evolved until it disappeared. For this purpose, early versions of the tool focused on automatically generalizing to any number of AHs, plotting both individual and common MOTS, as shown in Figure 3.6.

As the study progressed, I expanded my script to provide the option to color the AHs according to a scalar quantity. This was motivated by the desire to display the value of the expansion on the surface, as seen in Figure 3.7, but it generalizes to any scalar quantity provided with the same structure as the AH data.

Over the years, I made additional improvements to the visualization tool, both in terms of features and user interface. New features included plotting the spin vectors of the BHs and tracing the path of the BH centers, leading to Figure 3.8.

In 2019, LIGO and Virgo observed a BBH merger which resulted in what is likely an intermediate mass black hole (IMBH), a significant discovery as the existence of BHs in that mass range had not been confirmed. As part of that release, I created a visualization of the AHs as well as the GW data. This led to a large rewriting of my scripts and produced

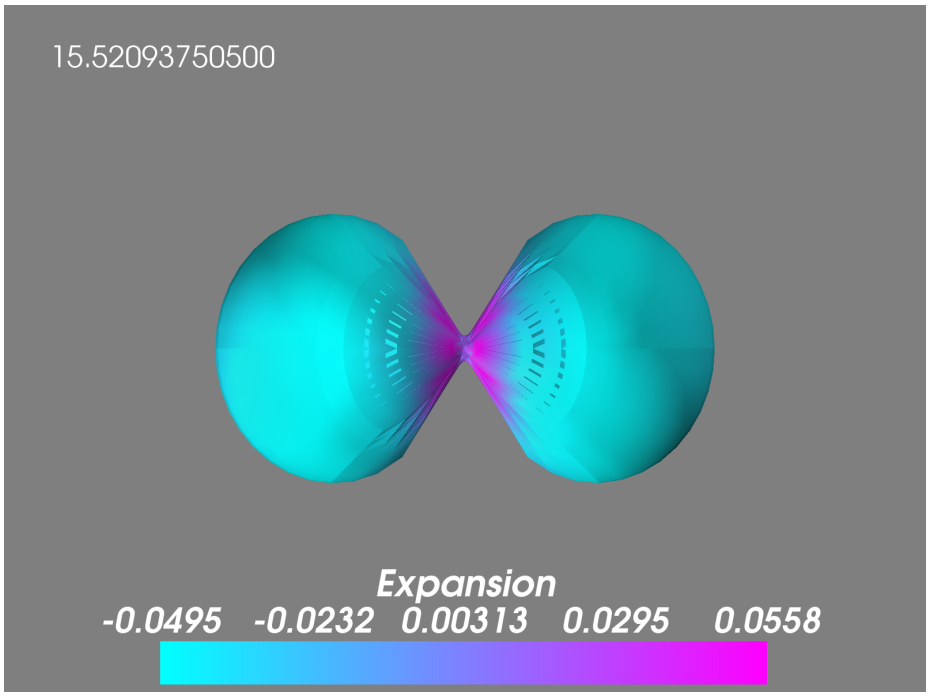

Figure 3.7: Inner common MOTS colored by the value of the expansion at each point. The simulation time is shown in the upper left corner in units of M.

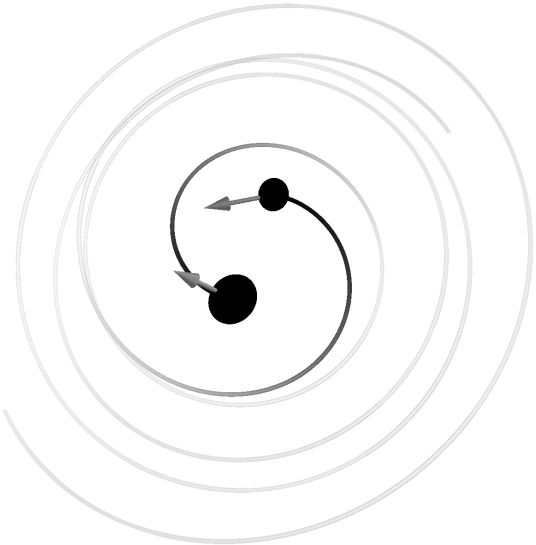

Figure 3.8: Coalescence of two BHs showing the AHs of BHs, their trajectories, and their spin vectors.

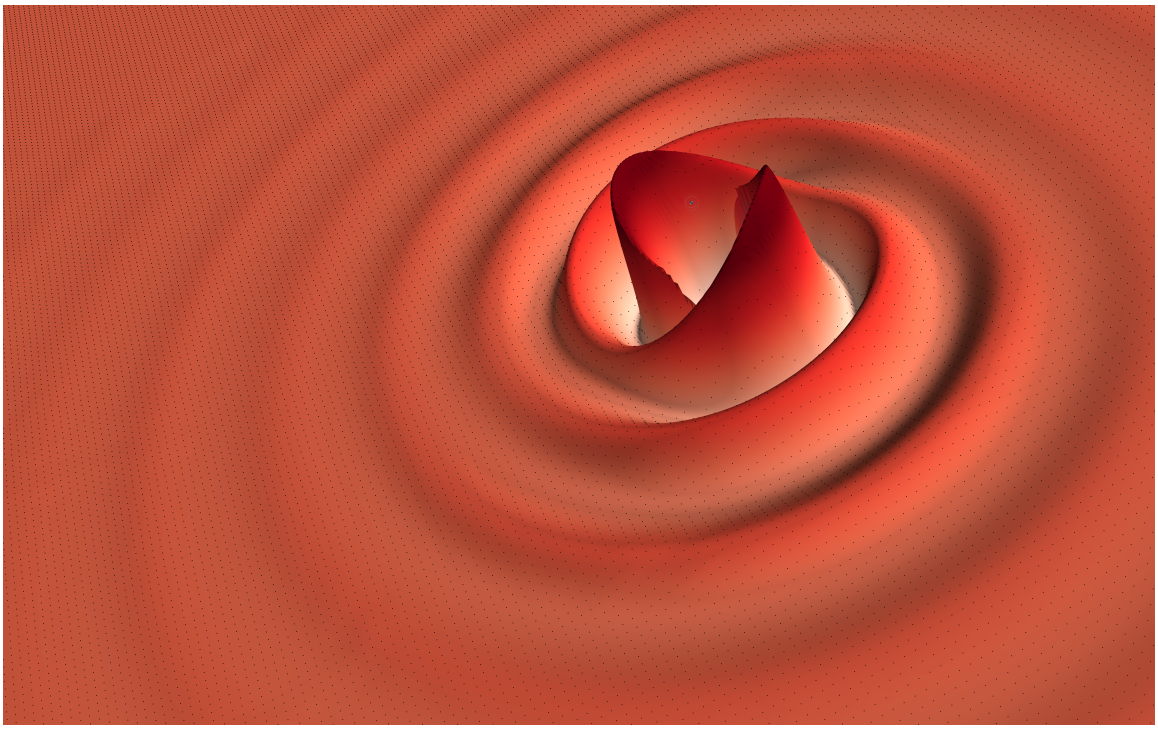

Figure 3.9: Ψ_4 emitted from the merger of two BHs. In the middle are the AHs of the initial BHs and the common AH.

the result shown in Figure 3.9.

I also extended the script to allow the camera view to change between frames. This was particularly useful because, while the AHs are plotted along with Ψ_4 in Figure 3.9, they are extremely tiny and difficult to see. I created a video which begins zoomed into the AHs (much like Figure 3.8) and then pans out until similar to Figure 3.9. The video can be seen at https://youtu.be/p43sb92YOww. I will continue improving this tool to make it more general and to increase its speed.

Performing and analyzing NR simulations both require a large amount of infrastructure which has been built and improved upon over the years by countless members of the group. In order to improve our waveform catalogs, both LVC and public, I have cleaned and edited our post-processing scripts as well as begun the creation of a new set of Jupyter notebooks. With my automation for creating `rpar` files, I have made it easier for new members to begin running simulations and have also taken the first step towards automating the running

of simulations. By introducing changes to AHFINDERDIRECT that allow for improved debugging, I have made it easier to search for MOTS during NR simulations. Additionally, with my AH visualization tool, we can plot AHs and scalar quantities in order to study our simulations as well as to create production quality images and videos.

CHAPTER 4

PREDICTING REMNANT SPIN

In the few years since the first detection of GWs [86], LIGO has reported signals from 50 binary systems [87, 88]. With each of these detections, we want to use the GW signal to characterize the source and perform tests of GR. This chapter will describe a new method to accomplish this goal by making use of NR simulations.

Each stage of the coalescence provides information about the merging BBH system; this chapter will focus on the parameters describing the remnant BH. The product of a BBH merger is a perturbed BH that emits ringdown radiation as it settles to a Kerr BH. This process provides fundamental information to understand gravity in its most extreme regime. Perturbation theory tells a compelling story about how perturbed BHs, like the remnant of a BBH merger, lose the information about the disturbance, often called hair, in the form of GWs [89]. Perturbed BHs ring down or emit GWs with a frequency (ω_{qnm}) and decay time (τ_{qnm}) characterized by the BH mass and spin [90], providing the means to determine the remnant BH parameters upon the detection of GWs.

The GW during this ringdown phase is generally represented as the sum of quasi-normal modes (QNMs), each expressible as a damped sinusoid with its own ω_{qnm} and τ_{qnm}, fixed by the mass and spin of the final BH [91, 92, 93]. The Echeverria formulas [94] provide relationships to determine the BH mass and spin from ω_{qnm} and τ_{qnm} using spheroidal harmonics. Since each of the spheroidal modes has its own value of ω_{qnm} and τ_{qnm} as predicted by the mass and spin, computing ω_{qnm} and τ_{qnm} for multiple modes would provide a test of GR. The possibility of using GWs to detect this spectrum of radiation is often referred to as BH spectroscopy [95, 96, 97].

There have been attempts to measure ω_{qnm} and τ_{qnm} of the ringdown from the GW data [98, 99, 100, 101, 102, 103, 104] and as the detectors improve in sensitivity, this

will become more viable. One common method is to estimate the ringdown parameters by matching directly to the exponentially decaying ringdown, where Ref.[101] finds consistent results for GW150914 searching for damped sinusoids. The short duration and low-amplitude of the signal expected from stellar-mass mergers, however, makes this post-merger phase challenging to detect, which is further compounded by the reliance upon knowing when ringdown begins [105, 106]. Ringdown is defined to begin once the GW signal reaches the linear regime. This transition from non-linear to linear has ambiguity which is worsened by the fact that each mode reaches the transition at a different time.

Due to these challenges, current approaches [107, 108, 109] to estimate the spin of the final BH match the data to theoretical models of the inspiral. Fortunately, NR provides the map from initial to final parameters [110, 111, 112] that are used to estimate the final spin. For systems with many cycles of inspiral, this method can predict the remnant spin with precision, assuming GR. It is desirable to obtain the remnant spin independently of matched filtering of either the inspiral or ringdown in order to perform tests of GR [107, 113, 114, 115]. One can also perform tests of GR directly from the peak frequency [116].

With the goal of avoiding the use of the exponentially decaying ringdown, we propose a method of determining the final spin that takes advantage of the higher amplitude at the merger of two BHs. The method proposed here builds on earlier work by Healy *et al* [117] which connected the instantaneous frequency of the GW at peak amplitude to ω_{qnm} and τ_{qnm} of the ringdown. While it is not obvious that such a relationship should exist, there have been hints of the merged BH entering a perturbative regime as early as the peak amplitude [118, 119, 117, 120] with the radiation near the peak amplitude of the strain being described by QNMs that include the overtones. In this chapter, we find that the spin of the remnant BH is already known at the peak amplitude.

Inspired by the results of Healy *et al*, we create a map linking the instantaneous frequency at maximum amplitude (ω_{peak}), the derivative of the instantaneous frequency at maximum amplitude ($\dot{\omega}_{peak}$), and the chirp mass ($\mathcal{M}$) to the dimensionless remnant spin

(a_f). One advantage of this method is that all measurements involved, ω_{peak}, $\dot{\omega}_{peak}$, and $\mathcal{M}$, are independent of fitting the data to a model waveform. Furthermore, $\mathcal{M}$ has the advantage of needing only a few pre-peak cycles to obtain a good measurement using a well known gravitational-wave algorithm, cWB [121]. In the following work published in Physical Review Letters, we: a) demonstrate a tight relation between the frequency properties measured at peak and the spin of the final BH and b) develop an algorithm to exploit this relationship on GW observations [122].

In Section 4.1, I describe the NR data used to derive a connection from ω_{peak}, $\dot{\omega}_{peak}$, $\mathcal{M}$ to a_f and discuss the associated errors. In Section 4.2, I examine the viability of the relationship as a form of parameter estimation with noisy data. Finally, I summarize our findings in Section 4.3.

4.1 Methodology

4.1.1 NR Catalog and Errors

The relationships found in this chapter are based upon the use of 112 NR simulations provided by the MAYA waveform catalog, 47 of which are nonspinning and 65 of which are aligned spin, with mass ratios $1 \leq q \leq 10$ [123].

We create a map from ω_{peak}, $\dot{\omega}_{peak}$, $\mathcal{M}$ to a_f. As will be described in Section 4.1.2 this equates to a mapping from the dimensionless instantaneous frequency at maximum amplitude ($\hat{\omega}_{peak}$), the derivative of the dimensionless instantaneous frequency at maximum amplitude ($\hat{\dot{\omega}}_{peak}$), and the symmetric mass ratio (η) to a_f.

In order to create this mapping, $\hat{\omega}_{peak}$, $\hat{\dot{\omega}}_{peak}$, and a_f are obtained from the NR simulation data. In this chapter we use the strain, $h(t)$, for ease of working with the GW detectors. The strain can be represented as a sum of spin-weighted spherical harmonics ${}_{-2}Y_{\ell,m}$, with the $\ell = 2$, $m = 2$ mode dominating the signal for aligned spin scenarios and face on orientations. Therefore, this study uses only the $\ell = 2$, $m = 2$ mode [124, 125, 126, 127].

The GW amplitude is thus $|h_{22}(t)|$, and the instantaneous frequency is found as the

derivative of the phase, *i.e.* $\dot{\phi}(t)$ where $\phi(t) = arg(h_{22}(t))$. $\hat{\omega}_{peak}$ and $\hat{\dot{\omega}}_{peak}$ are obtained by identifying the time at which the amplitude reaches a maximum and grabbing the instantaneous frequency and its time derivative at that time. This is shown visually in Figure 4.1. Note a_f is determined from the AH of the remnant BH.

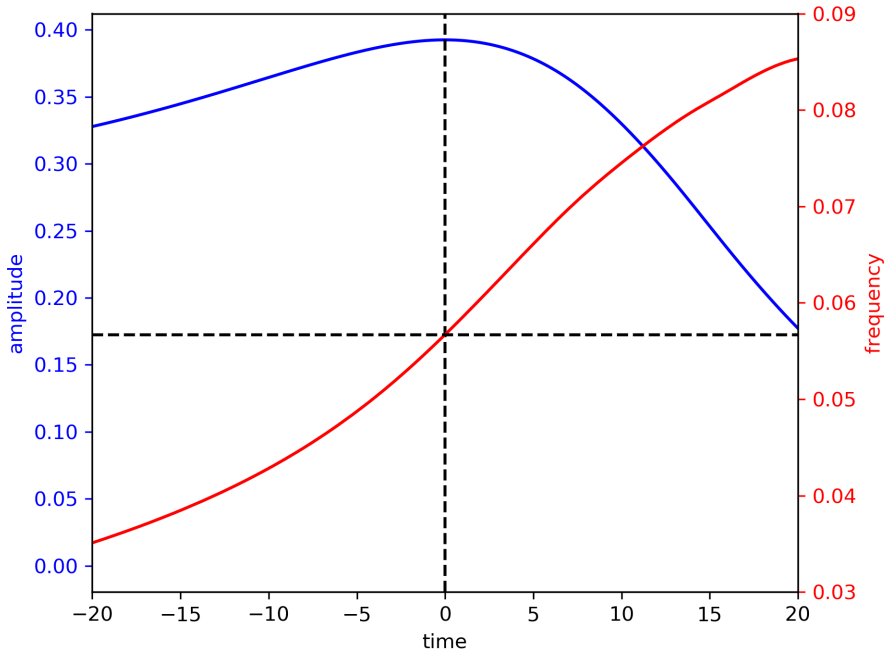

Figure 4.1: The amplitude and instantaneous frequency during merger. The vertical dotted line denotes the time of maximum amplitude and the horizontal dotted line shows the corresponding instantaneous frequency.

The finite spatial and temporal resolutions of NR simulations introduce systematic uncertainty into the estimates of frequency and spin. By repeating each simulation at multiple resolutions, the error is found to be of order 0.01% for a_f, 1% for $\hat{\omega}_{peak}$, and 1.4% for $\hat{\dot{\omega}}_{peak}$. These uncertainties account for the spread in the fit shown in Figure 4.2.

4.1.2 Fitting to final spin

With the data selected and the NR errors understood, I can create a fit that connects the peak amplitude of GW strain to the final BH spin. In order to create this fitting from ω_{peak},

$\dot{\omega}_{peak}$, and $\mathcal{M}$ to a_f using NR simulations, I utilize the following relationships:

$$\hat{\omega}\eta^{\frac{3}{5}} = \omega\mathcal{M}\,, \tag{4.1}$$

$$\hat{\dot{\omega}}\eta^{\frac{6}{5}} = \dot{\omega}\mathcal{M}^2\,, \tag{4.2}$$

where η is the symmetric mass ratio defined as a function of the initial masses, m_1 and m_2:

$$\eta = \frac{m_1 m_2}{(m_1+m_2)^2}\,, \tag{4.3}$$

and $\mathcal{M}$ is the chirp mass expressible as:

$$\mathcal{M} = \eta^{\frac{3}{5}}M = \frac{c^3}{G}\left(\frac{5}{96}\pi^{-\frac{8}{3}}f^{-\frac{11}{3}}\dot{f}\right)^{\frac{3}{5}}\,. \tag{4.4}$$

These lead me to plot the spin of the remnant BH against a function of $\hat{\omega}_{peak}\eta^{\frac{3}{5}}$ and $\hat{\dot{\omega}}_{peak}\eta^{\frac{6}{5}}$ which will take the form

$$x = ln\left(\left(\hat{\omega}_{\text{peak}}\eta^{\frac{3}{5}}\right)^{-\frac{11}{5}}\left(\hat{\dot{\omega}}_{\text{peak}}\eta^{\frac{6}{5}}\right)^{\frac{4}{5}}\right). \tag{4.5}$$

The resulting fit is shown in Figure 4.2. Adopting the same functional form as Healy *et.al* [117], I obtain the following best fit relationship

$$a_f = -0.216x^3 + 0.415x^2 - 0.252x + 0.989 \tag{4.6}$$

with an average spread of $\Delta a_f = 0.032$.

4.2 Final Spin

Having found an NR derived relationship relating ω_{peak}, $\dot{\omega}_{peak}$, and $\mathcal{M}$ to a_f, it's important to study how these values are obtained from real data and how precise this method will

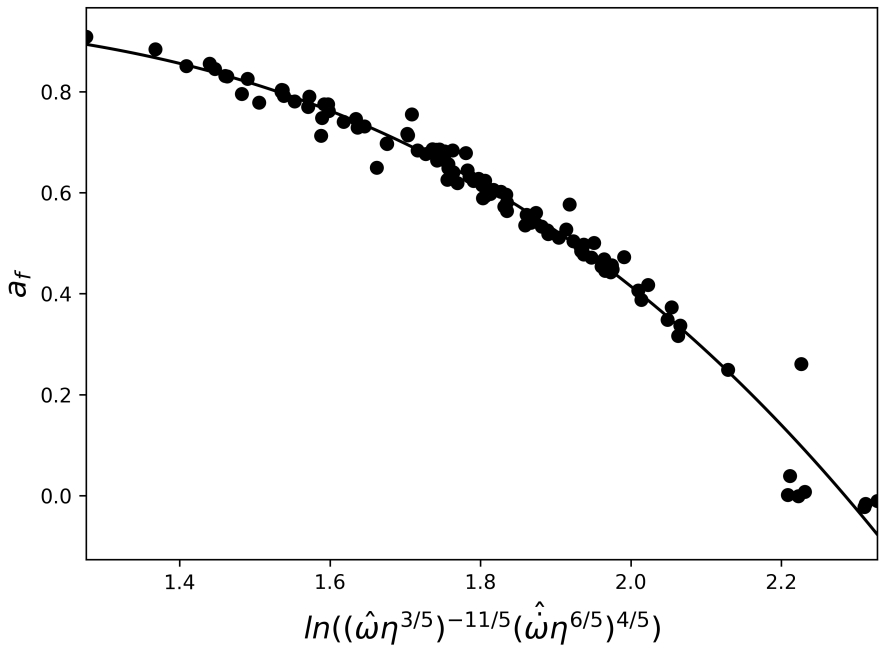

Figure 4.2: The dimensionless spin of the remnant BH versus a function of symmetric mass ratio, instantaneous dimensionless frequency, and its time derivative at maximum strain for aligned spin NR waveforms. The solid line shows the fitting relation described in Section 4.1.2.

be when faced with a detection. $\mathcal{M}$ is measured by burst searches that fit the frequency evolution of the signal [121]. By analyzing the recovered $\mathcal{M}$ of existing cWB runs, and using the knowledge that the uncertainty scales as 1/SNR [128], I estimate that the uncertainty in $\mathcal{M}$ as recovered by cWB is $\sim$1.5/SNR. This contributes an additional uncertainty of (126/SNR) % to a_f. For the SNR=100 runs I analyze in this chapter, this adds an uncertainty of 1.26% to a_f.

Since GW detector data is noisy, we can't reliably obtain ω_{peak} and $\dot{\omega}_{peak}$ directly without first de-noising it. In order to reconstruct a signal out of the noise, Ghonge and I use BW, a search pipeline that relies on modeling the GW as a number of sine Gaussians whose sum results in a coherent GW signal in a detector network [42]. By using this morphology-agnostic approach, the reconstructed waveform is robust against uncertainties which may be present in templated, CBC analyses. BW provides an independent, complementary estimate of the waveform morphology, and consequently avoids systematic uncertainty in the frequency evolution which might be present in the best fit CBC waveform [129, 130]. In this study we analyze the waveform as reconstructed by BW for the Livingston detector only.

To quantify the expected uncertainty in the remnant spin, I performed a systematic Monte-Carlo study whereby sets of BBH signals with increasing SNR [131] were added to stationary Gaussian noise colored with the PSD of the first observing run (O1) era LIGO detectors. The underlying waveforms for these "injections" were then recovered using BW. For a SNR of 100, I injected a h_{22} signal consistent with that of GW150914 in 2000 realizations of Gaussian noise and recovered ω_{peak} and $\dot{\omega}_{peak}$ for the median waveform of each. The value of ω_{peak} was obtained by first calculating the amplitude envelope of the median whitened waveform (using a python implementation of the Hilbert-Huang transform [132]) and then locating the time at which the amplitude is maximum. Then the median time frequency track, outputted by BW, is used to identify the frequency and the time derivative of the frequency at the given time.

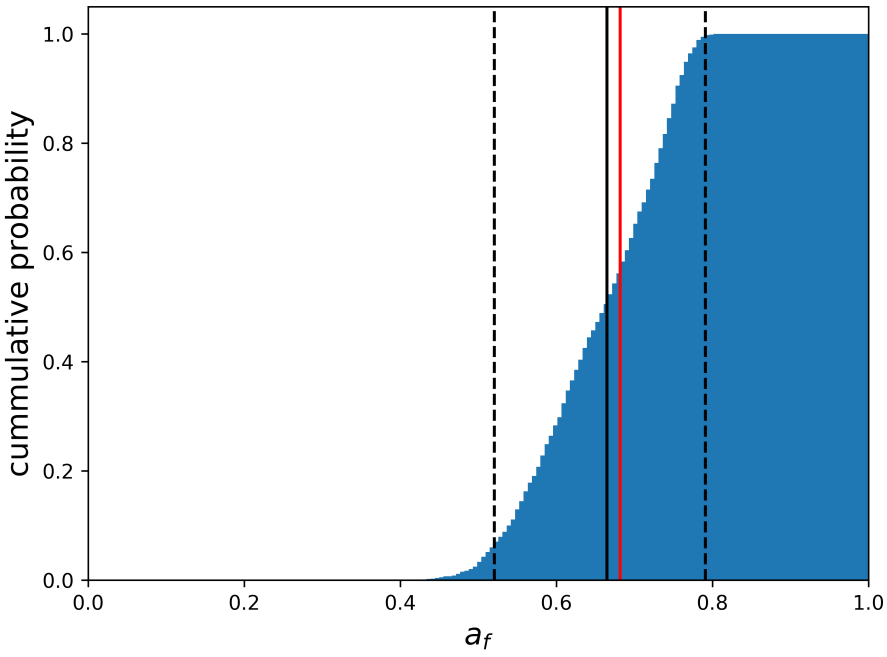

Figure 4.3: The cumulative probability distribution of the final dimensionless spin obtained for a GW150914-like signal injected into noise and recovered using BW with SNR 100. The solid black line shows the median recovered spin and the dotted black lines show the 90% confidence interval. The solid red line shows the true spin.

Figure 4.3 shows the cumulative probability distribution of the estimated a_f for our 2000 injections. The solid black line denotes the median, the solid red line denotes the true final spin, and the dotted lines show the 90% confidence interval, which is a_f=(0.51, 0.77) for SNR of 100.

To better understand how this error scales with SNR, I used the same technique just described with 250 injections each for SNRs 40, 60, 80, and 100. The resulting medians and 90% confidence intervals are shown in Table 4.1.

Table 4.1: Median and 90% confidence values of a_f for various SNRs.

SNR	median	lower 90% confidence	upper 90% confidence
40	0.671	0.437	0.802
60	0.677	0.484	0.785
80	0.654	0.497	0.782
100	0.667	0.510	0.772

4.3 Conclusions

This study finds that the remnant spin is known at the peak amplitude and presents a method of estimating it from the chirp mass, the frequency at maximum amplitude of the strain, and its derivative in an analytic relationship. This allows us to make use of the high SNR at the peak to estimate the final spin before entering the perturbative ringdown regime.

In order to understand the viability of this study as a parameter estimation method, we analyzed the distribution of the remnant spin obtained via recovering the waveform of a GW150914-like signal with increasing SNRs from 40 to 100. We demonstrate that we can reliably place bounds on the spin of the remnant BH using information found near the peak amplitude when the signal is dominated by the $\ell = 2$, $m = 2$ mode.

Our method avoids the usage of BBH templates, instead obtaining ω_{peak} and $\dot{\omega}_{peak}$ from a BW reconstruction and $\mathcal{M}$ from cWB. While matched filtering methods likely place a tighter bound on the remnant spin, our alternate approach is not subject to the same systematic biases due to waveform modeling present in the matched filter search. There remain systematic errors due to the fit we are using to determine the final spin from the peak amplitude. In addition, the fitting formula is an interpolation over a discrete set of NR templates and might change if more NR simulations are added to the fit.

Future steps in this study will see the method applied to all the LIGO/Virgo/KAGRA BBH detections with reasonable BW reconstructions from O1, O2, and O3. It will also be interesting to see the effect of adding precessing runs to the fit and whether this analysis can be expanded to include higher modes.

This chapter highlights how we can use NR to maximize the information we can obtain from current GW detections. I lay out a method to use NR simulations to create a map from quantities available during merger to parameters of the remnant BH. This can be used to compute the spin of the remnant BH from only information available during the loudest part of the GW signal. This provides more accurate parameter estimation for systems with very

little inspiral. In the case where the ringdown or the inspiral are observed, this provides an additional consistency test of GR.

CHAPTER 5

NUMERICAL RELATIVITY FOR FUTURE DETECTORS

As we prepare for future detectors with increased sensitivity and expanded frequency coverage, we need to explore the part NR will play. Waveforms extracted from NR simulations have played a crucial role in the detection and interpretation of GWs from merging BHs and NSs [133, 134, 135]. They have been used to construct models [136, 137, 138, 139, 140, 134], in direct analysis of the data [141], and as injections to stress test the detection pipeline [142]. As a first step towards preparing NR for future GW detectors, we need to investigate whether current NR codes have the capability to produce waveforms with the accuracy needed to unveil the wealth of information in the data collected by future detectors. In the work presented here, submitted for publication in Physical Review D Rapid Communication, we present the first estimate of the minimum resolution that a BBH simulation must have as a function of signal-to-noise ratio in order for the NR waveform to be indistinguishable from the true signal.

Differences between a template waveform and a GW signal could have many origins, including but not limited to, using the "wrong" theory of gravity, using an approximate theory of gravity, or having differences in the parameters of the system. Such errors or missing physics in the template waveform have the potential to lead to misleading or incorrect results. Assuming GR is the correct gravitational theory, the solutions to the vacuum Einstein equations, as well as the waveforms extracted from the solutions, only have errors associated with numerical discretization. This is in contrast with simulations containing NSs where the micro-physics of the stars is not well understood nor is the impact on the waveforms [143]. I will focus only on waveforms generated by evolving BBHs in vacuum under Einstein's theory of GR. Figure 5.1 shows an example of how the use of a low resolution template, one with significant discretization errors, can lead to residuals remaining

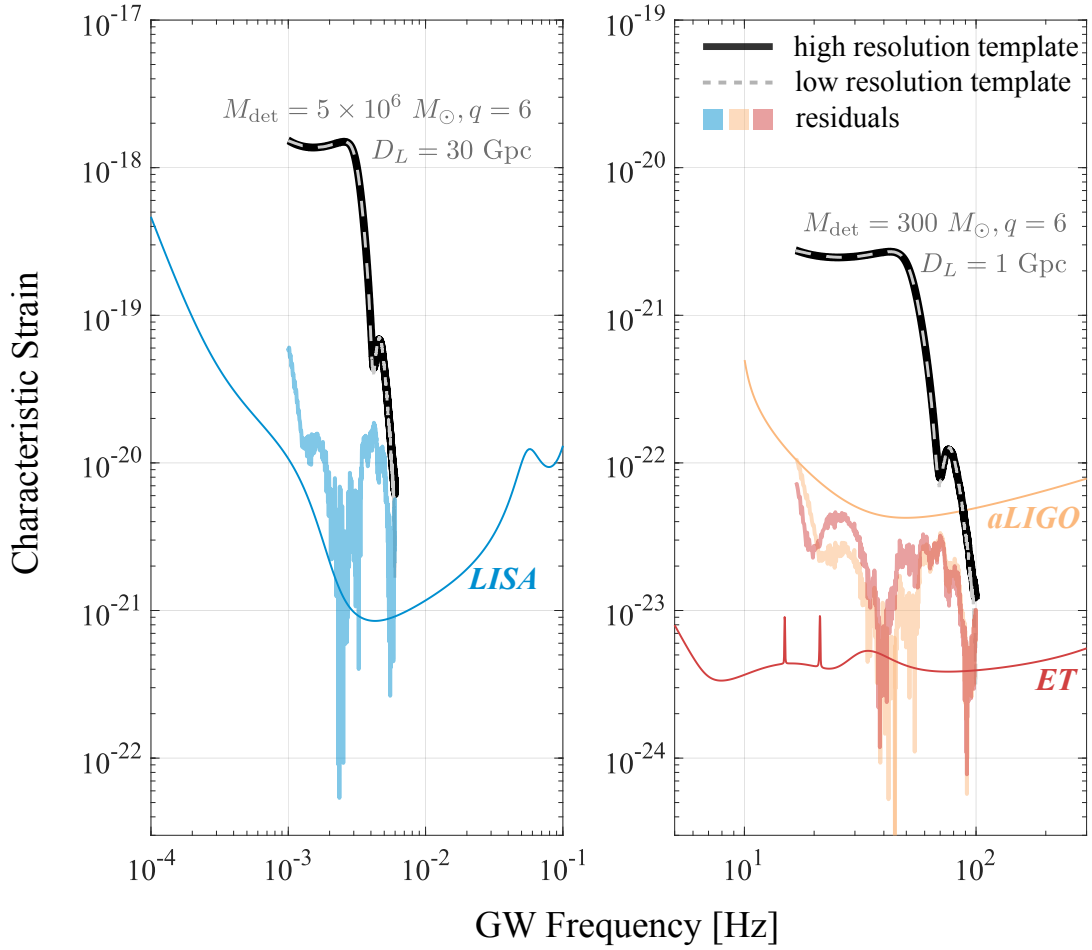

Figure 5.1: Strains (gray) for $q = 6$ sources with an aligned spin of $a = 0.2$ on the larger BH; also plotted are noise curves and the residuals remaining in the data after using a low resolution template to match the signal (high resolution waveform).

in the data after the template is used to match the signal. This is demonstrated for an unequal mass binary of mass ratio 6:1 with a small spin of 20% maximal on the larger BH. In order to consider current detectors as well as future ground and space-based detectors, we show this in comparison to the noise curves of LISA [144], ET [14], and Advanced LIGO at design sensitivity [145, 31]. The residual remaining in CE [146, 147] is comparable to that shown in ET.

To further stress the importance of having high resolution in unequal mass ratio binaries for which higher modes are relevant, we show in Figure 5.2 the strain of the same binary

but now at an inclination of $\iota = 15^0$ for LISA, along with two residuals [148, 17]. The blue dashed line is a low resolution waveform and the solid blue line is the residual resulting from using that waveform as the template in matched filtering. The dark red line is a high resolution waveform containing only the $(l, m) = (2, 2)$ mode, with the faint red line showing the residual resulting from using it as the template waveform. Notice that the two residuals are comparable, both in strength and even in structure for this case, although we note that the structure of the residual will change depending on the details of the match and waveform.

Several studies have explored the potential impact that numerical errors could have on interpreting LIGO data [142, 149, 150, 151], including bounds on the numerical errors necessary for detection as well as for measurement [152, 153, 149]. Reference [150] presents follow up work detailing different methods of assessing the accuracy of waveforms and the appropriate scenarios for each measure. Reference [154] discusses the requirements on waveform model accuracy in order to be prepared for third-generation ground-based detectors and the relative errors in NR waveforms. While NR simulations produce waveforms for which the numerical errors are less significant than the noise associated with the current detectors, this will likely change as the sensitivity of the detectors increases.

Our work focuses on the impact of the errors associated with NR simulations of BBHs. We present a criterion to assess the errors arising from using a discrete resolution in NR waveforms and use that criterion to estimate the minimum resolution required of NR simulations to produce waveforms indistinguishable from the true signal as a function of SNR in the context of LIGO, LISA, CE, and ET [14, 15]. We also demonstrate how using templates with low resolution may leave residuals that could potentially obscure or be confused with higher order modes.

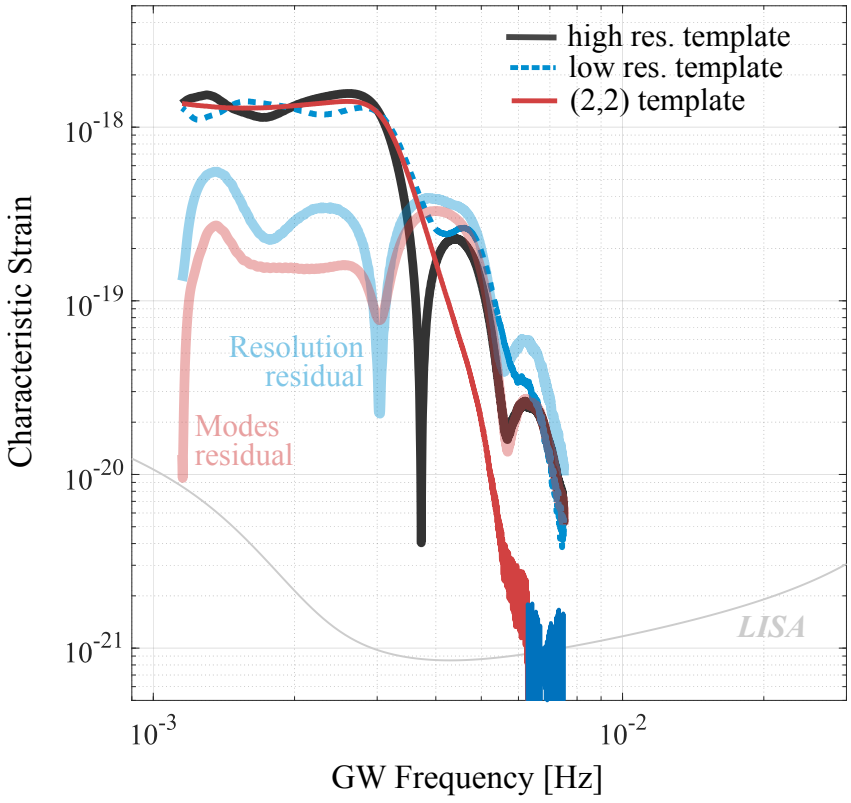

Figure 5.2: Strain (black line) of a high resolution $(q, \iota) = (6, 15^o)$ source with an aligned spin of $a = 0.2$ on the larger BH for LISA at a distance of 30 Gpc, $\rho = 976$. The blue dashed line is a low resolution waveform of the same source parameters, with the solid blue line denoting the residual resulting from using it as the template. The dark red line is a high resolution template containing only the $(l, m) = (2, 2)$ mode, with the faint red line showing the residual resulting from using it as the template waveform.

5.1 NR Waveforms

Our results are based on the MAYA catalog of waveforms [155] produced using the MAYA code [156, 157, 158, 159]. The simulations used in this study were performed on a grid with 10 refinement levels, a largest grid radii of $409.6\,M$, and a smallest grid radii of $0.2\,M$ ($0.1\,M$) for mass ratios of 1:1 (6:1). The inspiral parameters quoted for this study are computed at the beginning of the simulation, but there is evidence that the excess radiation emitted at the beginning of an NR simulation does not significantly impact the values of the parameters [160].

As with all BSSN codes, our MAYA code computes waveforms from the Weyl Scalar Ψ_4 extracted at a finite radius away from the BBH and then extrapolated to infinity [81]. For this study, all waveforms have been analyzed at the original extracted radius of $75\,M$, in order to isolate only the impact of resolution. While extrapolating the waveform to infinite radius makes the waveform more accurate to a true observed signal, by comparing all our waveforms at 75M, I am considering our "true" signal as it would appear at 75M. I have repeated this at multiple extraction radii and our results do not change. I therefore do not expect extracting the waveforms to infinite radius to change the impact of resolution, so I leave it at 75M for simplicity and error orthogonalization.

The strain, h, is given by the second time integral of Ψ_4. To facilitate analysis, the strain is decomposed in terms of spin-weighted spherical harmonics ${}_{-2}Y_{l,m}$, of which the $(l, m) = (2, 2)$ quadrupole mode is generally the most dominant. In the present work, I only use the modes: $(2, 1), (2, 2), (3, 2), (3, 3), (4, 3)$ and $(4, 4)$.

For the binary masses detected and expected, NR simulations are not generally able to produce waveforms with enough cycles to cover the sensitive frequency range of the LIGO and Virgo detectors. This will be even more significant for LISA, CE, and ET. To circumvent this, NR waveforms are stitched to approximates (e.g. PN), thus creating hybridized waveforms [161]. However, since the goal of this chapter is to analyze specifically the

truncation error associated with limited NR resolution, I am using only the NR waveform and computing the relevant quantities over the frequency range spanned by it. The starting frequencies for a total mass of $1M_{\odot}$ are provided by the NR waveforms, and I divide by total mass to obtain the desired frequency. For this analysis, I primarily consider total masses in the detector frame of $M_{det} = 300M_{\odot}$ for terrestrial detectors (CE, ET, and LIGO) and $M_{det} = 5 \times 10^6 M_{\odot}$ for LISA. For the NR waveforms utilized in this study, this means for terrestrial detectors I use a starting frequency of $f_{lower} = 6.8$ Hz for the equal mass scenario and $f_{lower} = 15.9$ Hz for the case with mass ratio 6:1. For LISA, I use a starting frequency of $f_{lower} = 4.1 \times 10^{-4}$ Hz for the equal mass scenario and $f_{lower} = 9.5 \times 10^{-4}$ Hz for the case with mass ratio 6:1. By increasing the initial frequency to shorten the waveform, I can assess the impact of only using a limited number of cycles in our analysis. Comparing the waveform with 7 inspiral cycles to the shortened waveform with only 2 inspiral cycles, I find that our results do not change significantly.

5.2 Criterion for Assessing Accuracy

A waveform h_i extracted from a NR simulation will differ from the exact solution h by an error δh_i; that is, $h_i = h + \delta h_i$. Since our code uses finite differencing, to leading order we have $\delta h_i = c\,\Delta_i^{\alpha}$. Here α is the convergence rate of the code, c depends on derivatives of h, and Δ_i is the characteristic discretization scale, or grid-spacing, used in the simulation. Due to our use of adaptive mesh refinements, Δ_i will refer to the grid spacing of our finest mesh, which covers the smallest of the two initial BHs.

By carrying out simulations of different resolutions, one can determine the convergence rate α of the code and extrapolate h_i to infinite resolution and, in principle, obtain h in a process called Richardson extrapolation [162]. Computing matches between a finite resolution template and the Richardson extrapolated waveform would be an ideal way to quantify the errors associated with limited resolution. However, effects from boundary re-

finements [74], extrapolations during temporal stepping, and outer boundary conditions, to name a few, make the process of Richardson extrapolation more challenging. Therefore, to approximate the truncation errors of a given resolution, I compute the relative errors between multiple simulations of different resolutions and, by doing this for multiple pairs of resolutions, compute our code's convergence rate and express the impact of the truncation errors as a function of resolution. To compute α I make use of a $q = 1$ BBH system with aligned, dimensionless spin of $a = 0.6$ for which we have multiple resolutions. By keeping the higher resolution waveform fixed at $\Delta_1 = 200$ and varying the lower resolution template, I compute $\alpha = 4$. As our simulations are performed using $6th$ order spatial finite-differencing and $4th$ order Runge-Kutta for time evolution, this value of convergence rate is consistent. There are other aspects of the simulations, such as the Berger-Oliger evolution scheme, which could cause additional sources of error, possibly with different convergence rates. Future work should be done to explore each of these other potential sources of error.

With the convergence rate established, let us consider the overlap of two NR waveforms, h_1 and h_2:

$$\mathcal{O}[h_1, h_2] \equiv \frac{\langle h_1|h_2\rangle}{\sqrt{\langle h_1|h_1\rangle\langle h_2|h_2\rangle}}, \tag{5.1}$$

where

$$\langle h_1|h_2\rangle = 2\int_0^\infty \frac{h_1^* h_2 + h_1\, h_2^*}{S_n} df\,, \tag{5.2}$$

with S_n being the one-sided power spectral density of the detector, and $*$ denoting the complex conjugate. Expanding Eq. 5.1 to second order in the truncation error [163]:

$$\mathcal{O}[h_1, h_2] \approx 1 - \frac{1}{2}\left(\Delta_2^\alpha - \Delta_1^\alpha\right)^2 \frac{\langle c|c\rangle}{\langle h|h\rangle}\left[1 - \mathcal{O}^2[h, c]\right]. \tag{5.3}$$

Noting that c depends on derivatives of h, we can approximate that $\mathcal{O}^2[h, c] \approx 0$ and

write Eq. 5.3 in terms of the mismatch, $\epsilon = 1 - \max_{t_0 \phi_0} \mathcal{O}$, as

$$\epsilon[h_1, h_2] = \frac{\beta^2}{2} \left(\Delta_2^\alpha - \Delta_1^\alpha\right)^2 , \tag{5.4}$$

with $\beta^2 = \langle c|c\rangle / \langle h|h\rangle = \langle c|c\rangle / \rho^2$ and $\rho = \langle h|h\rangle^{1/2}$ being the SNR.

Following reference [149], a NR waveform will be indistinguishable by the detector from the true signal if and only if: $\langle \delta h|\delta h\rangle < 1$, or equivalently $\Delta^{2\alpha}\langle c|c\rangle < 1$. We propose a new version of this criterion for assessing accuracy written in terms of β as

$$\rho < \frac{1}{\beta\, \Delta^\alpha}, \tag{5.5}$$

allowing a *direct* computation between SNR and NR discretization.

5.3 Applying Accuracy Criterion to Detectors

Once I obtain values for α and β, Eq. 5.5 provides the SNRs for which a NR waveform of a given resolution will be indistinguishable from a signal of the same parameters. Using simulations with multiple different resolutions, I compute mismatches ϵ to obtain α and β from Eq. 5.4. It is important to keep in mind that β depends on both the detector and the parameters of the source (mass M_{det}, mass ratio q, spins a, and inclination ι). Here I define mass ratio such that $q \geq 1$.

I explore the values of β for three different BBH systems each for LIGO, CE, ET, and LISA. For the equal mass BBH case, I keep the higher resolution waveform fixed at $\Delta_1 = M/200$ and consider lower resolutions of $\Delta_2 = M/80$, $M/120$, and $M/140$. Using these, I compute $\beta \approx 10^6$ for all three detectors. For unequal mass simulations, finer resolution is required to fully resolve the smaller BH. Therefore, for a $q = 6$ BBH with the more massive BH having an aligned, dimensionless spin of $a = 0.2$, I use resolutions

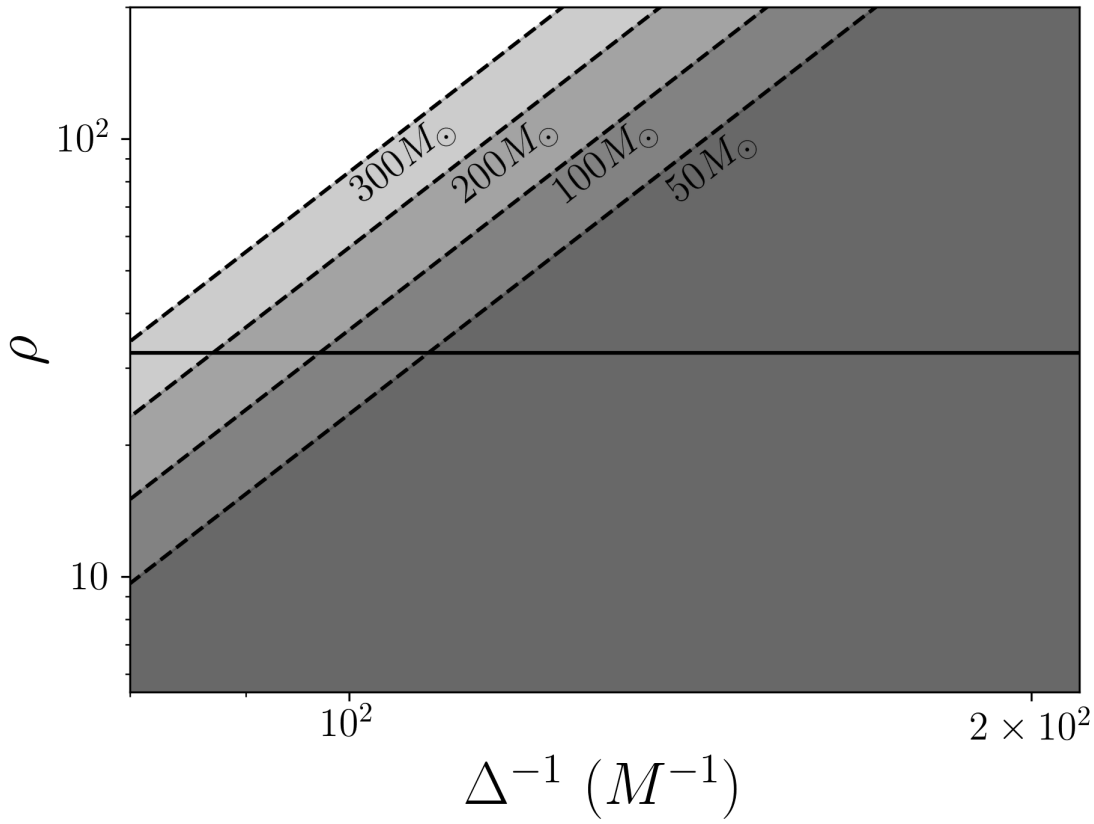

Figure 5.3: Plot of $\rho < 1/(\beta\,\Delta^{\alpha})$ where Δ is the resolution of a NR simulation for $(q, \iota) = (1, 0^o)$ with an aligned spin of $a = 0.6$ for both BHs in the case of LIGO for several M_{det}. The horizontal line shows $\rho = 32.4$, the highest SNR yet observed.

of $\Delta_1 = M/280$ and $\Delta_2 = M/200$ to obtain $\beta \approx 10^7$ when observed with $\iota = 0$ and $\beta \approx 5 \times 10^8$ when observed with $\iota = 15^o$, in each of the detectors. While these values do change with total mass, they remain at the same order of magnitude.

Figure 5.3 shows Eq. 5.5 for $(q, \iota) = (1, 0^o)$ in the case of LIGO for several M_{det}. The horizontal line shows $\rho = 32.4$, the highest SNR yet observed by LIGO. The BBH case in this figure is characteristic of most of the $q \approx 1$ BBH systems observed so far. Since the NR waveforms used in the data analysis of those signals had resolutions $\Delta < M/120$, they were not distinguishable by LIGO from the true signal.

Looking towards the future detectors as well, Eq. 5.5 is plotted in Fig. 5.4 for three detectors: a second-generation detector (LIGO), a third-generation terrestrial detector (ET),

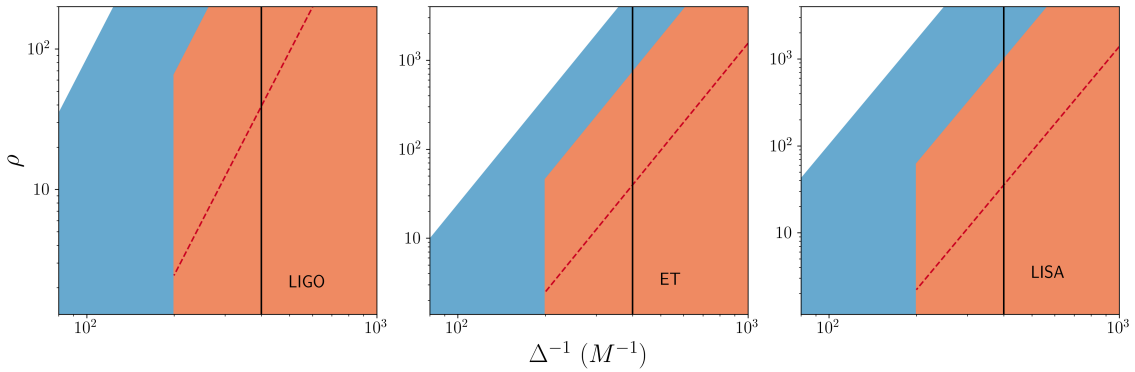

Figure 5.4: Logarithmic plots of $\rho < 1/(\beta\,\Delta^{\alpha})$, where Δ is the resolution of a NR simulation. The regions where the inequality holds are shown by the blue shaded region for $(q, \iota) = (1, 0^o)$ with $a = 0.6$ for both BHs, the red shaded region for $(q, \iota) = (6, 0^o)$ with $a = 0.2$ for the larger BH, and below the dashed line for $(q, \iota) = (6, 15^o)$. The vertical line shows the highest resolution of our production runs ($\Delta = M/400$).

and a space-based detector (LISA). The results for CE are extremely comparable to those for ET. Each of the shaded regions show the values of ρ for which an NR waveform of a given resolution Δ is guaranteed to be indistinguishable from the true signal of the same parameters. Blue is for the case $(q, \iota) = (1, 0^o)$, and red is for the case $(q, \iota) = (6, 0^o)$. Below the red dashed line is the case $(q, \iota) = (6, 15^o)$. The vertical line shows the highest resolution MAYA waveform in the LVC catalog ($\Delta = M/400$). I do not include data below the lowest NR resolutions we analyze, $\Delta = M/80$ for $q = 1$ and $\Delta = M/200$ for $q = 6$.

For LISA, CE, and ET, it appears that for low mass ratio cases, current NR waveforms will be sufficient at the expected SNRs. For the $(q, \iota) = (6, 0^o)$ case (red regions), NR waveforms at our current highest resolution ($\Delta = M/400$) would be sufficient for $\rho < 800$ for each of the detectors. Since it is expected that LISA, CE, and ET will be able to detect signals in the hundreds or thousands, it is clear from Figure 5.4 that one would require resolutions of at least $\Delta \approx M/600$. The situation gets more challenging if the source has inclination, allowing higher modes to be more observable. For LISA, CE, and ET in the case $(q, \iota) = (6, 15^o)$, resolutions at the level of $\Delta \approx M/10^3$ are needed to reach $\rho \approx 10^3$.

Equation 5.5 also allows us to estimate the fractional loss of SNR due to numerical

errors:

$$\frac{\delta\rho}{\rho} = \frac{\rho_i - \rho}{\rho} = \sqrt{\frac{\langle h_i|h_i\rangle}{\langle h|h\rangle}} - 1 \approx \frac{1}{2}\Delta^{2\alpha}\beta^2 < \frac{1}{2\,\rho^2}\,. \tag{5.6}$$

This equation allows us to see that for signals with large SNR, the fractional loss will be less than for low SNR signals.

5.4 Conclusions

Given the SNR of BBH signals, we have provided estimates of the resolution needed in NR finite-differencing codes to produce waveforms that are indistinguishable by the LIGO, LISA, CE, and ET detectors from the real signal, assuming that the template and the signal have the same parameters. We showed that for detections such as the ones obtained by LIGO so far, with $\rho < 40$, current finite-difference codes are capable of producing adequate waveforms if $\Delta < M/120$. We also showed that for high mass ratio binaries or binaries with inclination, where higher modes play an important role, NR codes need to improve significantly. To reach SNRs above a thousand, finite-difference NR codes would have to efficiently scale to resolutions of at least $\Delta < M/700$. At those resolutions, to obtain even 7 orbits, we would require approximately 16 nodes on a Stampede equivalent cluster for about 30 days, a very heavy computational load for even the minimum requirements. More orbits will be important when performing simulations for LISA, increasing the necessary time to complete a simulation. Additionally, in order to accurately analyze simulations with inclination such that higher modes become more prominent, even finer resolutions will be required, increasing the necessary node count and time.

Reaching resolutions for template indistinguishability is particularly important because, as I demonstrated, residuals resulting from using lower resolution templates could be comparable to those resulting from ignoring higher modes entirely. Additionally, since the models used in data analysis are trained on NR waveforms, their accuracy is directly limited by

that of NR. If we are incapable of providing accurate, indistinguishable NR waveforms, we will not be able to maximize the scientific return from next generation detectors.

While this chapter investigates the relationship between resolution and SNR, there are alternative ways to increase the convergence rate of the codes, including increasing the finite-differencing order or implementing more efficient differencing schemes. The need for high quality NR waveforms may be alleviated if the very high SNR signals are not coincident in the detectors, allowing on-demand NR simulations to be deployed per high SNR event.

The next step of this study will be a parameter estimation study to understand how this NR truncation error translates to uncertainty in the physical parameters of the source. Furthermore, the present work was done using the methodology typical for LIGO data analysis, and simply using the noise curves for each detector. However, LISA's data analysis will be notably more complicated, and it will be a crucial future step to study the impact of these errors with LISA's data analysis machinery [44]. This is particularly important since it is expected that LISA will detect numerous signals concurrently. Additionally, using the techniques discussed here, we can explore the impact of other errors including those caused by extraction radius and boundary conditions.

CHAPTER 6

OPTIMIZING NUMERICAL RELATIVITY TEMPLATE PLACEMENT

Over the last few years, GW detections have gone from being a dream to being a regular occurrence. In the upcoming years, current detectors including LIGO and Virgo will improve in sensitivity and are expected to provide us with even more frequent GW observations. In the slightly more distant future of ≈ 2030, LISA will begin its observing run, as could possible third-generation, ground-based detectors, bringing unprecedented sensitivities and new frequency bands.

To capitalize on the wealth of knowledge provided by each of these detections, it is imperative to have sufficient template waveform banks to be used for detection and parameter estimation. In order to have continuous coverage of the parameter space with which to build the template banks, searches often use analytic models which have been trained on NR waveforms. The banks are built such that the mismatch between a model waveform and the detected signal is no more than 3% [30]. Therefore, the NR waveforms the models are trained upon must fill the parameter space densely enough such that this can be achieved with high accuracy.

With the improved detector sensitivities, template banks which would be sufficient for current detectors may no longer be densely populated enough. Additionally, the high sensitivities of future detectors will require much more accurate waveforms and thus very highly resolved NR simulations [164]. The parameter space of NR BBH coalescences is 8 dimensional, consisting of mass ratio $q = m_1/m_2$, 3-dimensional spins $\vec{a_1}$ and $\vec{a_2}$, and eccentricity e. To be prepared for the future wealth of detections, it would be ideal to densely populate the entire parameter space with NR simulations. Unfortunately, NR simulations are both time consuming and computationally expensive and create discrete coverage of the parameter space. Therefore, each NR simulation needs to be chosen with care in such

a way that it maximizes the scientific benefit.

In this chapter, I discuss two approaches I am currently taking towards achieving this goal. First, I seek to reduce the parameter space by exploring whether future detectors will be sensitive to the secondary spin of high mass ratio binaries. Then, I generalize this to explore the impact that each parameter has by creating a NN to predict the match between two waveforms given the initial parameters of their respective binaries.

6.1 Decreasing Spin Parameter Space

In order to mitigate the need for time consuming, computationally expensive, high resolution NR simulations, I first explore how we can reduce the NR parameter space. For EMRIs, the smaller BH can be considered a perturbation, and its spin plays a much smaller role in the dynamics of the spacetime [165]. With this knowledge as motivation, I explore the importance of the spin of the smaller BH (henceforth referred to as the secondary spin) for various mass ratios where NR is still the appropriate technique. I define how the critical SNR, ρ_{crit}, above which the secondary spin is distinguishable from a nonspinning counterpart changes with mass ratio and spin magnitude.

The NR waveforms analyzed in this chapter are built from the MAYA code. The grids of our AMR are structured such that the smallest grid spans the smallest BH. Therefore, the resolutions (grid-spacing of the finest mesh) are higher for the high mass ratio cases. My current results extend up to $q = 5$.

I make use of the requirement that if the residual waveform $\delta h = h_1 - h_2$ satisfies

$$\langle \delta h | \delta h \rangle < 1 \,, \tag{6.1}$$

the two waveforms are indistinguishable by the detector [149].

For each mass ratio, I performed a simulation with both the primary and secondary BH nonspinning. I then compare to it a suite of simulations with a nonspinning primary BH and

an aligned spin secondary BH with spin magnitudes $a_2 = [0.2, 0.4, 0.6, 0.8]$. By treating the spinning waveform as our "signal" and the nonspinning waveform as our "template", I investigate the residual remaining by approximating the signal from a spinning binary with a template from a nonspinning simulation. Using PyCBC [24], I mimic the methods of LIGO data analysis to perform matched filtering. I align the two waveforms such that the match is maximized over time and phase. I then subtract the nonspinning waveform from the spinning waveform to obtain a residual and compute its SNR. Eq. 6.1 is equivalent to stating that the SNR of the residual waveform must be less than one. The fractional SNR of the residual of the waveform $\frac{\langle \delta h | \delta h \rangle}{\langle h_1 | h_1 \rangle}$ is constant as I change distance, so I can identify ρ_{crit}.

These simulations begin at a separation of $11M$, leading to ~ 20 cycles of inspiral. For the purposes of this analysis, we only consider the SNR within the frequency range spanned by the NR waveforms. Changing the detector frame mass of the system changes the results slightly, since it changes the frequency of merger. For most of this study, we select the masses such that the merger occurs at approximately the most sensitive frequency of each detector. For LISA, this corresponds to $M_{det} = 5 \times 10^6 \, M_\odot$. Since we allow the SNR to change, we are also allowing the distance and therefore the source frame mass to change.

The value of ρ_{crit} as a function of mass ratio and spin magnitude can be seen in Figure 6.1. It can be seen that as the mass ratio increases, a secondary spin of the same magnitude requires higher SNR to be distinguishable. Similarly, for a fixed mass ratio, the required SNR decreases with higher spin magnitude. As I consider higher mass ratios, we will be able to see how this trend extends. I will also consider binary systems with antialigned spins in future work.

6.2 Predicting Match Between Waveforms

We can see that the significance of the secondary spin decreases as the mass ratio increases, so how can we expand that to explore the impact of each of the other parameters? Since

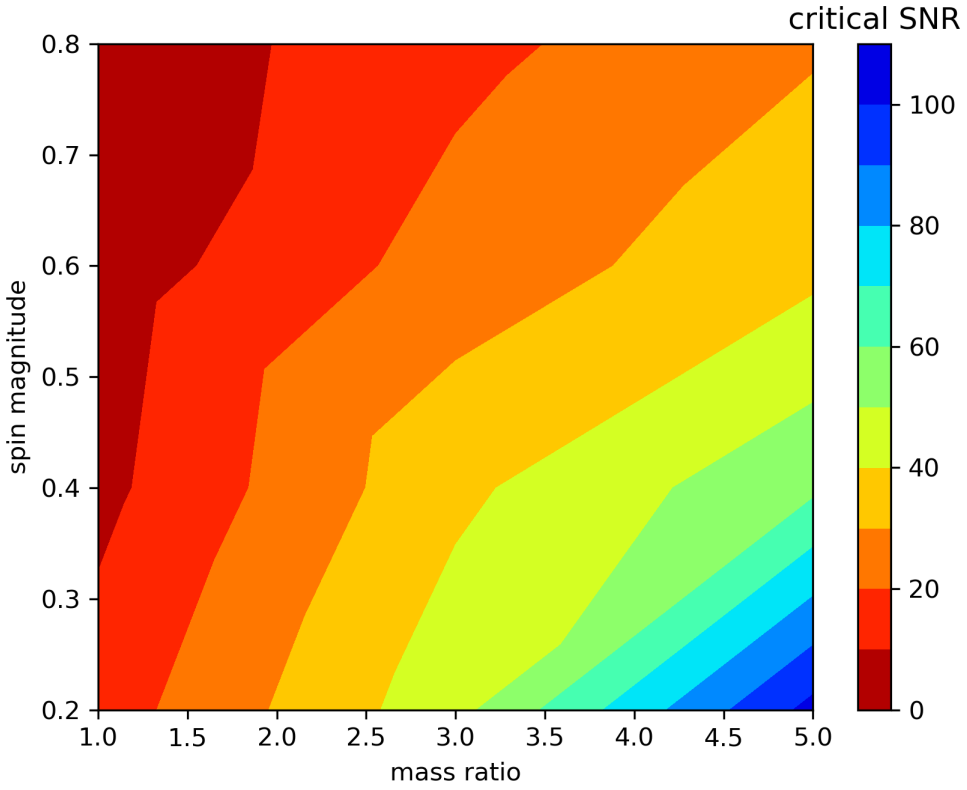

Figure 6.1: Plot of the critical SNR as a function of the mass ratio and the secondary spin magnitude. The critical SNR defines the SNR at which the waveform from a BH binary with a spinning secondary BH is distinguishable from an otherwise equivalent nonspinning binary.

certain parameters may cause more variation in the gravitational signal than others, we need a way to quantify how different two waveforms are. There could be a number of ways of doing this including comparing the frequency evolution or the relative excitation of higher modes. However, one approach frequently used to compare waveforms is the match. If the match could be predicted before performing a simulation, a map of the parameter space could be created to identify regions which have minimal match with already existing simulations. The next optimal NR simulation could then be identified.

6.2.1 Match Predicting Neural Network

This section presents a NN which takes in the initial parameters of two BBH systems and outputs the match of their respective gravitational waveforms. I begin by outlining the architecture of the network. I go on to describe how I compute the match and generate the training data from each pair of waveforms. Finally, I assess the accuracy of the newly developed model.

Network Parameters

The input array for this NN contains the initial parameters for a pair of NR BBH simulations. BBH systems (at a given total mass) can be described by their mass ratio $q = m_1/m_2$, spin vectors $\vec{a_1}$ and $\vec{a_2}$, and eccentricity e. For binary systems where the spins are not aligned with the angular momentum of the binary, the directions of the spins evolve throughout the inspiral, while the magnitude stays consistent. I therefore define the spins at the same orbital frequency for all simulations. I consider only simulations with low eccentricity and approximate them as quasi-circular, giving each simulation 7 parameters, so the input array for the network, X, has 14 values for each training sample. The output node is the match between the waveforms of each BBH system. Figure 6.2 shows the input and output parameters of the network.

The data set is made up of 620 SXS NR waveforms from the LVC NR catalog. I

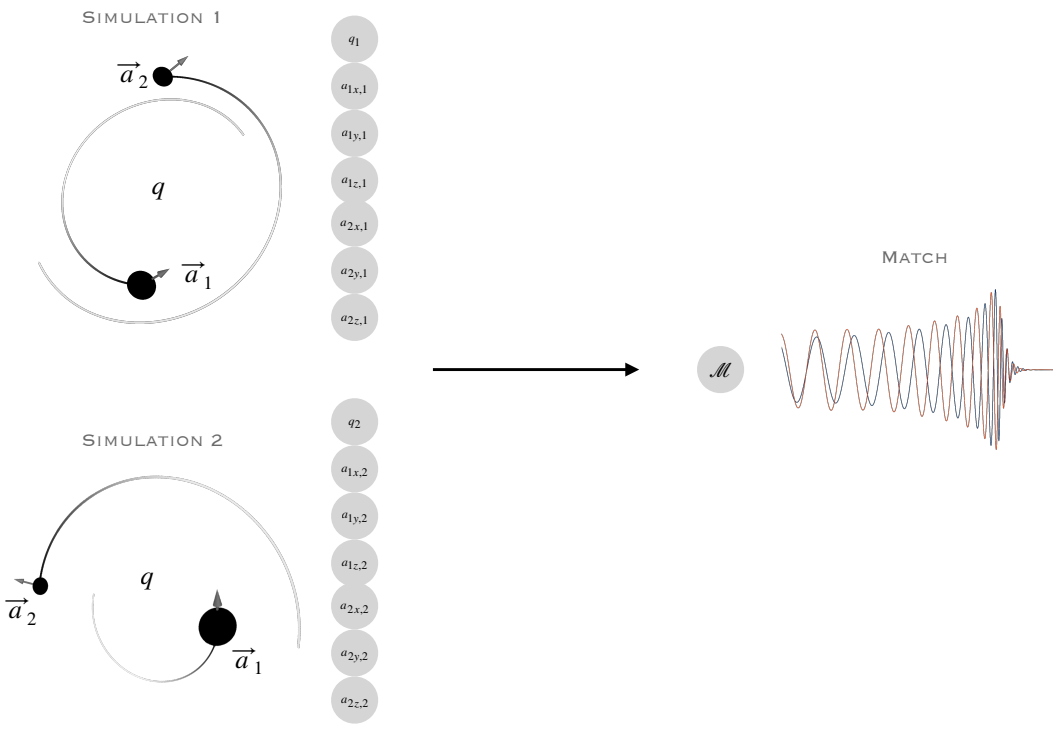

Figure 6.2: Diagram showing the input and output parameters of the match prediction NN. 7 input parameters per simulation totals 14 input parameters. The only output parameter is the match.

consider only SXS waveforms at this point because they include the spin components as a function of time, allowing the spins for all simulations to be defined at the same frequency. Since the inputs of the model include two simulations, each point is a pair of waveforms, leading to a data set of 384,400 points. I use ratios of 0.94/0.03/0.03 for my train/dev/test split, giving 361,337 points in the training set and 11,533 each in the development and testing sets.

Training Data

In order to create the train/dev/test data, I compute the match between all pairs of simulations included in this analysis. The match is dependent upon the detector and the total mass. The results I present in this chapter use a flat PSD set to unity, allowing me to make predictions purely based on the NR data without concern for detector or mass. However, the network can be trained on any noise curve and mass, allowing the results to be aimed specifically at particular detectors or types of events.

The NR waveforms are provided as the gravitational strain expressed in terms of the spherical harmonics, ${}_{-2}Y_{\ell,m}$. For the purpose of this study, we combine all the modes with a face-on orientation ($\theta, \phi = 0$). This means the $\ell = 2$, $m = 2$ mode will be the most dominant, but we aren't excluding higher order modes.

To perform the match computation for each pair of simulations, I utilize PyCBC [24], a python package used to analyze GWs. Given that each simulation may start at a different separation and therefore a different frequency, I compute the match over the frequency range which is spanned by both simulations.

Network Architecture and Accuracy

I created the NN with python using Tensorflow [166]. The architecture for this model is a simple one, using only fully connected layers, combined to create a deep NN. While the architecture of this network is still being optimized, the current network has 10 layers, each

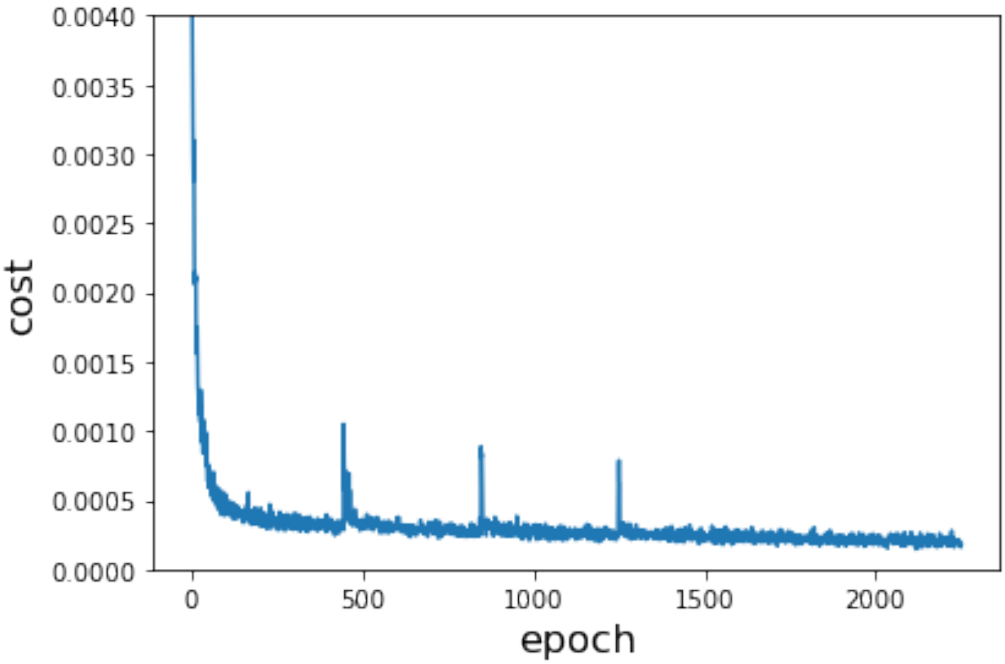

Figure 6.3: Cost at each epoch during the training of the match prediction NN.

with 448 nodes. I used a learning rate of 0.01 (the proportionality constant involved in the gradient descent) and a batch size of 16. Figure 6.3 shows the cost averaged over each epoch. The occasional spikes are caused by continuing the training from a checkpoint. This causes a spike before settling back down.

After training for 2250 epochs, the model had a train error of 0.0164 and a dev error of 0.0178. In other words, I can predict the match, which ranges between 0 to 1, to within 0.0178 on average. With this model, I am able to provide the initial parameters of two BBH systems and predict how similar their resulting gravitational radiation will be. Ultimately, this network will allow us to create a map of the BBH parameter space showing how similar a proposed simulation would be to those already existing within the catalog. This will help us identify the optimal simulation to perform in order to maximize the scientific gain. For this purpose, the error of 0.0178 will be sufficient. Nevertheless, I am still continuing to train this model to improve this error.

6.2.2 Estimating Spin at Given Frequency

In the model described in the previous section, I only used SXS waveforms because they contained the spin orientation for the duration of the inspiral. For many other simulations, this is not always the case. In order to expand the model to use more waveforms, the spins would need to be predicted at the given frequency. Additionally, when setting up new simulations, it would be ideal if the chosen frequency can be used as the starting frequency for new simulations. This motivated me to develop a way to estimate the spin directions as a function of frequency for a simulation to identify the spin at a given frequency. I chose to tackle this with a NN as well since the spin evolution does not appear to take a simple form as a function of frequency.

Typically NNs perform best within the domain spanned by the training data. However, for this task, some simulations will need to have their spin data extrapolated to higher or lower frequencies. Since the spin evolution is fairly stable, we should be able to extrapolate the spin to earlier times (and lower frequencies) within a reasonable margin of error.

Figure 6.4 shows the spin evolution for the primary BH of MAYA simulation GT0010 and how we can divide the data for training and testing purposes. First, we will train on the data available during the part of the simulation shown by the blue line. Then we will test how well it can predict the frequencies and spins shown in orange. By obtaining the error as a function of $\Delta f = f_0 - f$ where f is the frequency at which the training begins, we can estimate how well our model extrapolates. Then, we will continue training our model by adding in the test data (the data in orange) and then use it to extrapolate the spin to lower frequencies, using our error as a function of Δf to approximate the uncertainty.

This network is trained for each waveform individually, using the frequency to predict the spin directions. Therefore, the input array for the training set consists only of the frequency at every point of the training data. The output array contains the spin directions, θ and ϕ, for the primary and secondary BH at the given GW frequency.

I performed preliminary tests on three MAYA waveforms: GT0010, GT0203, GT0205.

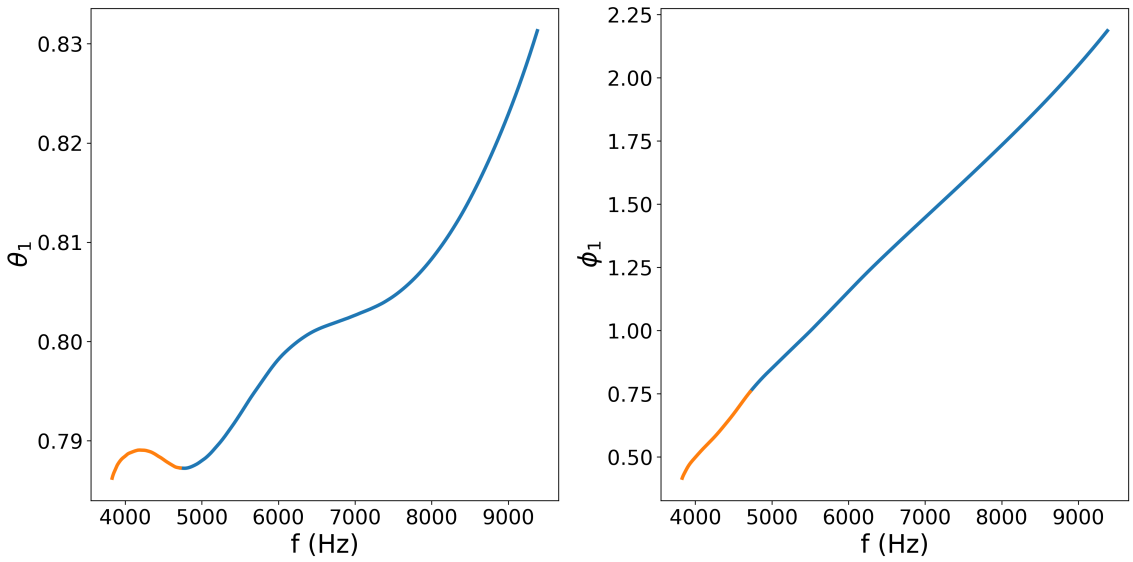

Figure 6.4: Spin direction of the primary BH during the inspiral of a precessing BBH system. The colors show how we can train our model on a subsection of the frequencies and then test at lower frequencies. The blue line shows the frequencies and spins trained over. The orange line shows the frequencies and spins tested over.

An average error in spin direction as a function of Δf is shown in Figure 6.5. The model predicts the spin direction to within 0.02 radians for θ_1 and 0.21 radians for ϕ_2. In both cases, the error roughly increases with Δf. It is worth noting that the value of ϕ generally changes much more rapidly than θ so the increased error is not unexpected.

While this model is in its preliminary stages, it promises to be an incredibly useful tool. This will allow us to compare precessing simulations that don't have concurrent spin data. Utilizing this model while generating the training data for my match prediction model will allow me to expand the training set.

As we prepare for improvements in current GW detectors and next generation detectors, we need to consider how NR will be used. Accurately characterizing the signals observed by detectors relies upon having dense template banks of model waveforms, trained upon NR. This chapter began exploring the question of which regions of NR parameter space need to be more densely covered and which regions can be more sparse. Answering this question will allow us to optimize how we prepare NR catalogs for the next generation of

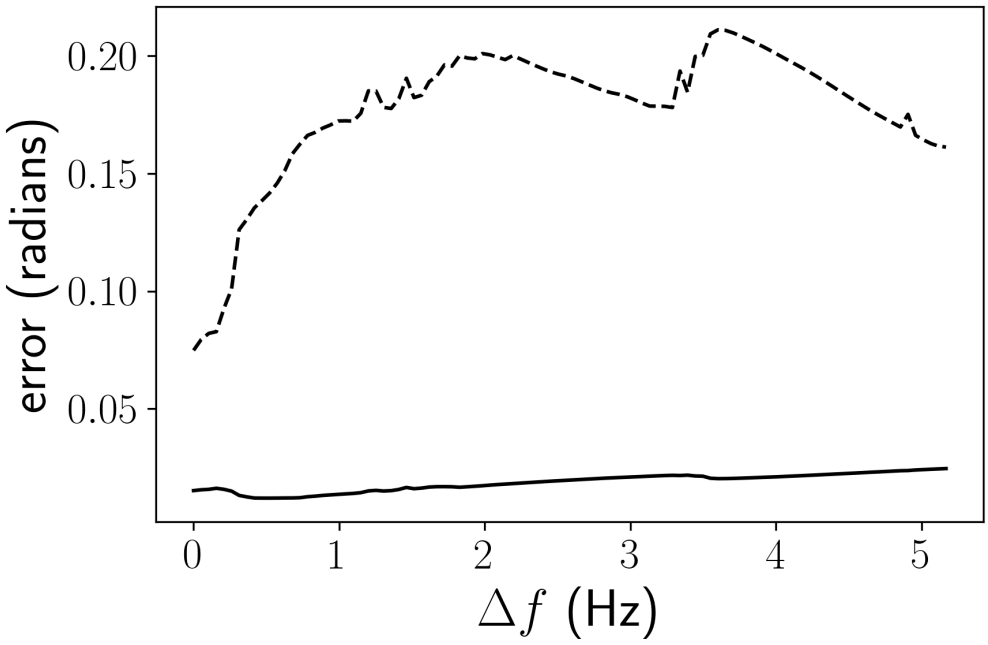

Figure 6.5: Average error in the predicted spin direction as a function of frequency. The solid line denotes the average error for θ and the dashed line denotes the average error for ϕ.

detectors.

CHAPTER 7
SUMMARY AND FUTURE OUTLOOK

With GW detections becoming more frequent, we have a new way to observe our universe. However, in order to understand these detections, we need to have predictions of what GW signals from various sources should look like according to theory. NR provides this by solving the Einstein equations computationally, allowing us to simulate mergers of compact binaries and obtain their expected gravitational waveforms. This dissertation addresses how to use these NR waveforms to maximize the scientific gain from GW observatories.

There is a large computational infrastructure built around our MAYA code, including both pre- and post-processing steps which have been developed over many years by numerous people. This dissertation describes a number of improvements I have made to this infrastructure, both modifying existing scripts and introducing new tools. I added additional automation to the simulation setup, making it easier for new members to begin performing simulations. I improved our scripts which take raw NR simulations and create catalog ready `h5` files as well as the tests used to ensure they are of LVC caliber. I then stitched all the post-processing steps into a single script, once again with the aim of simplifying the process such that new members can create catalog ready waveforms. Additionally, I created a new visualization tool which creates images and movies of the AHs of the BHs as well as their spin vectors and trajectories. It also allows for the plotting of the Ψ_4 gravitational radiation data. The tool is highly configurable, letting the user choose which quantities to plot and style it as they so choose.

I then created a new way to use NR to improve the parameter estimation and tests of GR that can be performed using the data from current GW detectors. This was done by developing a method to identify the spin of the remnant BH using only information available near merger. Using a bank of NR waveforms, I performed a fit from a function of the

instantaneous frequency at the time of maximum amplitude $\hat{\omega}_{peak}$, its derivative $\hat{\dot{\omega}}_{peak}$, and the symmetric mass ratio η to the dimensionless spin of the remnant BH, a_f. Since GWs scale with total mass, utilizing this relationship first requires scaling with a form of mass. For this study, we use the chirp mass $\mathcal{M}$, which will eliminate the need to know the symmetric mass ratio. Thus, to compute the remnant spin a_f from the GW signal, one needs only obtain the chirp mass $\mathcal{M}$, the instantaneous frequency at the time of maximum amplitude ω_{peak}, and its derivative $\dot{\omega}_{peak}$. These can be obtained entirely using burst searches, rather than modeled searches. Since the ringdown radiation is often dominated by noise, this provides an alternative method of identifying the spin independently of analyzing ringdown. This allows for additional GR consistency tests as well as parameter estimation for situations where little inspiral is observed, such as in the case of high mass binaries.

Next, this dissertation considered the use of NR in the context of future GW detectors. The next generation of GW observatories will bring higher sensitivities and access to new frequency bands. With this comes new data analysis challenges. LISA is expected to see possibly on order of 10^4 overlapping BBH signals, some with SNRs in the thousands. Characterizing all these signals will require template waveforms accurate enough that they don't leave behind significant residuals and don't obstruct parameter estimation. NR simulations are performed on computational grids, inherently limiting the accuracy. This dissertation establishes, for finite-differencing NR codes, what resolution is necessary as a function of signal SNR, in order for the template to be indistinguishable from a true signal. It showed that for some simple BBH systems, e.g. equal mass, current NR codes are capable of producing accurate enough templates. However, for situations where higher modes become more prominent, e.g. high mass ratio particularly with nonzero inclination, NR codes will be pushed to their limit, becoming extremely inefficient at best. To prepare for the next generation of detectors, it will be important to focus on improving the efficiency and accuracy of NR codes.

Since NR simulations are so computationally expensive and time consuming, it is im-

portant to carefully choose their placement in parameter space. One way to do this is to reduce the effective parameter space by analyzing how well detectors will be able to distinguish certain parameters. In this dissertation I discussed the resolutions at which a system with a spinning secondary BH becomes indistinguishable from a system with a nonspinning secondary BH as a function of mass ratio and spin magnitude. As the mass ratio increases, the secondary spin becomes more challenging to resolve. Therefore, for high mass ratio cases, the secondary spin parameter space may not need to be filled as densely as other parameters.

This can be extended to discuss the impact of all the parameters, as I showed by creating a neural network to predict the match between any two waveforms given the initial parameters of their binary systems. This dissertation details a network which takes in 14 input parameters, mass ratio q, and two spin vectors $\vec{a}_2$ and $\vec{a}_2$ for each of the two simulations and outputs their resulting match. The network is trained on the SXS waveforms in the LVC NR catalog, with 361,337 training points and 11,533 points each for the *dev* and *test* sets. The resulting network is able to predict the match to within 0.0178 on average. Using this, we can identify regions in the parameter space which have low match compared to the existing catalog, in order to perform simulations that will provide as much benefit as possible.

These studies work together to both maximize our scientific gain from current signals as well as to prepare for the next generation of GW detectors. NR is an extremely powerful tool which allows us to simulate BBH mergers and obtain the radiation they will emit. We can use this, in combination with detector data, to study gravity in its strongest regimes. This is an incredible opportunity and needs to be optimized for.

Appendices

APPENDIX A

MATCH COMPUTATION TOOL

The match and SNR are both frequently used values when considering how NR interfaces with GW detection. Since the match is the overlap maximized over time and phase, there are a number of necessary steps in order to compute these values. In order to make this easier and more automated, I wrote a Jupyter notebook to perform all necessary steps, given a configuration file. An example configuration file is as follows:

```
{
    "tag":"prefix_for_saved_results",
    "filepath1": "/path/to/first_waveform.h5",
    "filepath2": "/path/to/second_waveform.h5",
    "label1": "label_for_first_waveform",
    "label2": "label_for_second_waveform",
    "output_directory": "/path/to/save/results",
    "generate_figures": true,
    "save_frequency_series": true,
    "save_time_series": true,
    "print_psd": true,
    "match_cases": [
        {
            "mass": 300.0,
            "distance": 1000.0,
            "detector": "LIGO",
            "iota": 0.0,
            "phi": 0.0,
```

```
            "mode_array_1": [[2,2], [3,3], [4,4]],
            "mode_array_2": [[2,2], [3,3], [4,4]],
            "supplementary_info": "all_significant_modes"
        },
        {
            "mass": 300.0,
            "distance": 1000.0,
            "detector": "ET",
            "iota": 0.0,
            "phi": 0.0
        },
        {
            "mass": 5000000.0,
            "distance": 30000.0,
            "detector": "LISA",
            "iota": 0.0,
            "phi": 0.0
        }
    ]
}
```

A single configuration file describes a suite of comparisons done between two given waveforms with various physical parameters such as total mass and distance. The value of `tag` is a prefix to be used when saving results from this set of tests. `filepath1` and `filepath2` give the paths to the `h5` files to be compared, and `label1` and `label2` are their respective labels to be used in plotting and as column headers. The `output_directory` specifies where to save all the resulting files. If the directory does not exist, the notebook will create it. The next parameter, `generate_figures`, specifies whether to create plots

of the waveforms and their residuals. The next three parameters are boolean flags which specify whether to save text files of the waveform and residual frequency series, the waveform and residual timeseries, or the PSDs respectively.

Finally the user provides an array of cases over which to perform the match. Within each case, the user must provide the total mass M, detector frame distance D, inclination ι, and coalescence phase ϕ. The user also has the choice to provide specific modes to include for each waveform. If the parameters `mode_array_1` or `mode_array_2` are not provided, all modes are included in the computations. The user can also provide any supplementary info to be included as a tag for the results of that specific case only.

When run with the given configuration file, the notebook outputs a results file which contains the SNRs for the signal and the residual, the signal SNR at which the residual SNR would be greater than 1, and the match between the two waveforms. It also outputs the desired time and frequency series as well as figures if so specified.

APPENDIX B

HORIZON VISUALIZATION TOOL

AHFINDERDIRECT searches for and outputs AHs associated with the BHs during NR simulations. I've written a script which can visualize these surfaces as well as the trajectories and spins of the associated BHs. It can also plot the Ψ_4 data in the xy-plane as a 3D surface. The script takes in a `config.json` file created by the user to specify all the parameters for the visualization. Each of the following is one top level field in the `config.json` file. I've broken them apart here to walk through each of the parameters.

```
"paths":{
  "data_path": "/path/to/data",
  "image_output_path": "/path/to/image/location"
},
```

This is where the user provides the path to the horizon data and the location to store the frames generated by the script.

```
"scalar": {
  "use_scalar_coloring": false,
  "data_prefix": "h",
  "find_limits": true,
  "colormap": "bone"
},
```

The user specifies whether or not they want to color the BHs based on some scalar value. They specify the prefix of the file with the scalar data in `data_prefix`. Additionally, the user has the option to either have the code automatically find the minimum and maximum

values of the scalar variable or specify it themselves in `min_and_max.txt`. The user also specifies the colormap with which to color the horizons.

```
"spin": {
  "plot_spin_vectors": true
},
```

This allows the user to turn on and off the spin vectors.

```
"trajectory": {
  "trace_path": true
},
```

The user can choose whether or not to trace the path of the BHs.

```
"black_holes": {
  "colors": [[0.3,0.3,0.3],[0.3,0.3,0.3],[0.3,0.3,0.3]],
  "opacities": [1, 1, 0.8]
},
```

The `color` parameter specifies the color of the BHs, unless the scalar data is being used for coloring purposes. The `opacity` parameter specifies whether the BHs can be seen through. It can be interesting to set the opacity of the common MOTSs to less than 1 in order to observe the inner MOTSs within them.

```
"psi4": {
  "plot_surface": true,
  "use_colormap": true,
  "color": [0.901961, 0.329412, 0.243137],
  "colormap": "Blues",
  "opacity": 1,
```

```
  "plot_dots": true,
  "dot_size": 4,
  "large_grid_filename": "Psi4r_lev0.h5",
  "small_grid_filename": "Psi4r_lev2.h5",
  "excise_middle": true
},
```

The first parameter, `plot_surface`, allows the user to turn on and off plotting a physical surface representing Ψ_4. `use_colormap`, `color`, `colormap`, and `opacity` change the appearance of the surface, specifically its color and opacity. The user can also plot Ψ_4 as a grid of dots mapping out the same surface. They can also adjust the dot size given in pixels. `large_grid_filename` and `small_grid_filename` specify the `h5` files of the two Ψ_4 grids being plotted. Near the BHs, Ψ_4 gets extremely large, which can be problematic for visualization purposes. If `excise_middle` is set to true, the middle is removed from the visualization. If set to false, the middle is dropped to a large negative number.

```
"view": {
  "use_static_view": false,
  "static_values": {
    "distance": 600,
    "elevation": 45,
    "azimuth": 0,
    "focalpoint": [0, -75, -50],
    "roll": -60
  },
  "start_values": {
    "distance": 20,
    "elevation": 45,
```

```
    "azimuth": 0,
    "focalpoint": [0, 0, 0],
    "roll": -60
  },
  "final_values": {
    "distance": 600,
    "elevation": 45,
    "azimuth": 0,
    "focalpoint": [0, -75, -50],
    "roll": -60
  },
  "dynamic_timing": {
    "start_panning_iteration": 229376,
    "end_panning_acceleration_iteration": 236032,
     "end_panning_iteration": 294144,
    "begin_opacity_deceleration": 241152,
    "final_opacity_iteration": 248832
  }
},
```

This set of parameters controls the view of the camera. If `use_static_view` is set to true, the camera does not move throughout the visualization and is fixed at the values specified in `static_values`. If it is set to false, the camera starts at the values put in `start_values` and ends at the values specified in `final_values`. The timing of the camera change is controlled by the parameters in `dynamic_timing`. Each of these values is an iteration. The parameter `start_panning_iteration` tells the script when to begin moving the camera from the start position. This also begins the transition to the specified value of opacity for Ψ_4. `end_panning_acceleteration_iteration` controls

how long it takes the camera to reach its primary velocity. This transition period makes the animation much smoother. `end_panning_iteration` specifies at what iteration the camera should reach its final position. Often, the opacity transition needs to happen quicker than the zoom so it has its own parameters. It begins at the same time as the camera change, but it begins decelerating at `begin_opacity_deceleration` and reaches its final state at `final_opacity_iteration`.

```
"image": {
  "background_color": [0.298, 0.494, 0.643],
  "image_size": [6144, 3840],
  "frame_prefix": "panning_blue",
  "display_label": false,
  "label_time_scale": 1
}
```

This section includes more general parameters. `background_color` specifies the color of the canvas. This is particularly important if the user is either not plotting Ψ_4 or is excising the middle. `image_size` specifies the resolution at which to save the image. If `frame_prefix` is an empty string, the image will be saved as `frame#.png` where `#` is the iteration. Otherwise, the image will be saved as `frame_prefix_frame#.png`. The user can also choose to display a label in the upper left corner showing a scalar multiplied by the iteration using `display_label`. If the user sets `label_time_scale` to 1, it displays the iteration itself. Other values can be used, e.g. to scale it to show the time instead.

REFERENCES

[1] A. Einstein, "The Foundation of the General Theory of Relativity," *Annalen Phys.*, vol. 49, no. 7, pp. 769–822, 1916, [Annalen Phys.354,no.7,769(1916)].

[2] A. Einstein, "Näherungsweise Integration der Feldgleichungen der Gravitation," *Sitzungsberichte der Königlich Preußischen Akademie der Wissenschaften (Berlin*, pp. 688–696, Jan. 1916.

[3] R. A. Hulse and J. H. Taylor, "Discovery of a pulsar in a binary system," *Astrophys. J.*, vol. 195, pp. L51–L53, 1975.

[4] J. M. Weisberg and J. H. Taylor, "Relativistic binary pulsar B1913+16: Thirty years of observations and analysis," *ASP Conf. Ser.*, vol. 328, p. 25, 2005. arXiv: astro-ph/0407149 [astro-ph].

[5] J. M. Weisberg, D. J. Nice, and J. H. Taylor, "Timing Measurements of the Relativistic Binary Pulsar PSR B1913+16," *Astrophys. J.*, vol. 722, pp. 1030–1034, 2010. arXiv: 1011.0718 [astro-ph.GA].

[6] J. P. W. Verbiest, L. Lentati, G. Hobbs, R. van Haasteren, P. B. Demorest, G. H. Janssen, J.-B. Wang, G. Desvignes, R. N. Caballero, M. J. Keith, and et al., "The international pulsar timing array: First data release," *Monthly Notices of the Royal Astronomical Society*, vol. 458, no. 2, 1267–1288, 2016.

[7] C Affeldt, K Danzmann, K. L. Dooley, H Grote, M Hewitson, S Hild, J Hough, J Leong, H Lück, M Prijatelj, S Rowan, A Rüdiger, R Schilling, R Schnabel, E Schreiber, B Sorazu, K. A. Strain, H Vahlbruch, B Willke, W Winkler, and H Wittel, "Advanced techniques in GEO 600," *Classical and Quantum Gravity*, vol. 31, no. 22, p. 224 002, 2014.

[8] The LIGO Scientific Collaboration, "Advanced LIGO," *Classical and Quantum Gravity*, vol. 32, no. 7, p. 074 001, 2015.

[9] F. Acernese *et al.*, "Advanced Virgo: a second-generation interferometric gravitational wave detector," *Class. Quant. Grav.*, vol. 32, no. 2, p. 024 001, 2015. arXiv: 1408.3978 [gr-qc].

[10] Y. Aso, Y. Michimura, K. Somiya, M. Ando, O. Miyakawa, T. Sekiguchi, D. Tatsumi, and H. Yamamoto, "Interferometer design of the kagra gravitational wave detector," *Phys. Rev. D*, vol. 88, p. 043 007, 4 2013.

[11] J. Aasi *et al.*, "Advanced LIGO," *Class. Quant. Grav.*, vol. 32, p. 074 001, 2015. arXiv: 1411.4547 [gr-qc].

[12] R. Abbott *et al.*, "Open data from the first and second observing runs of Advanced LIGO and Advanced Virgo," Dec. 2019. arXiv: 1912.11716 [gr-qc].

[13] B. Abbott *et al.*, "Prospects for Observing and Localizing Gravitational-Wave Transients with Advanced LIGO, Advanced Virgo and KAGRA," *Living Rev. Rel.*, vol. 21, no. 1, p. 3, 2018. arXiv: 1304.0670 [gr-qc].

[14] M. Punturo *et al.*, "The Einstein Telescope: A third-generation gravitational wave observatory," *Class. Quant. Grav.*, vol. 27, F. Ricci, Ed., p. 194 002, 2010.

[15] M. Abernathy *et al.*, "Einstein gravitational wave telescope conceptual design study," *EGO*, 2011.

[16] J. Baker, J. Bellovary, P. L. Bender, E. Berti, R. Caldwell, J. Camp, J. W. Conklin, N. Cornish, C. Cutler, R. DeRosa, M. Eracleous, E. C. Ferrara, S. Francis, M. Hewitson, K. Holley-Bockelmann, A. Hornschemeier, C. Hogan, B. Kamai, B. J. Kelly, J. Shapiro Key, S. L. Larson, J. Livas, S. Manthripragada, K. McKenzie, S. T. McWilliams, G. Mueller, P. Natarajan, K. Numata, N. Rioux, S. R. Sankar, J. Schnittman, D. Shoemaker, D. Shoemaker, J. Slutsky, R. Spero, R. Stebbins, I. Thorpe, M. Vallisneri, B. Ware, P. Wass, A. Yu, and J. Ziemer, "The Laser Interferometer Space Antenna: Unveiling the Millihertz Gravitational Wave Sky," *arXiv e-prints*, arXiv:1907.06482, arXiv:1907.06482, Jul. 2019. arXiv: 1907.06482 [astro-ph.IM].

[17] P. Amaro-Seoane, H. Audley, S. Babak, J. Baker, E. Barausse, P. Bender, E. Berti, P. Binetruy, M. Born, D. Bortoluzzi, J. Camp, C. Caprini, V. Cardoso, M. Colpi, J. Conklin, N. Cornish, C. Cutler, K. Danzmann, R. Dolesi, L. Ferraioli, V. Ferroni, E. Fitzsimons, J. Gair, L. Gesa Bote, D. Giardini, F. Gibert, C. Grimani, H. Halloin, G. Heinzel, T. Hertog, M. Hewitson, K. Holley-Bockelmann, D. Hollington, M. Hueller, H. Inchauspe, P. Jetzer, N. Karnesis, C. Killow, A. Klein, B. Klipstein, N. Korsakova, S. L. Larson, J. Livas, I. Lloro, N. Man, D. Mance, J. Martino, I. Mateos, K. McKenzie, S. T. McWilliams, C. Miller, G. Mueller, G. Nardini, G. Nelemans, M. Nofrarias, A. Petiteau, P. Pivato, E. Plagnol, E. Porter, J. Reiche, D. Robertson, N. Robertson, E. Rossi, G. Russano, B. Schutz, A. Sesana, D. Shoemaker, J. Slutsky, C. F. Sopuerta, T. Sumner, N. Tamanini, I. Thorpe, M. Troebs, M. Vallisneri, A. Vecchio, D. Vetrugno, S. Vitale, M. Volonteri, G. Wanner, H. Ward, P. Wass, W. Weber, J. Ziemer, and P. Zweifel, "Laser Interferometer Space Antenna," *arXiv e-prints*, arXiv:1702.00786, arXiv:1702.00786, 2017. arXiv: 1702.00786 [astro-ph.IM].

[18] A. Taracchini *et al.*, "Effective-one-body model for black-hole binaries with generic mass ratios and spins," *Phys. Rev. D*, vol. 89, no. 6, p. 061 502, 2014. arXiv: 1311.2544 [gr-qc].

[19] M. Pürrer, "Frequency domain reduced order model of aligned-spin effective-one-body waveforms with generic mass-ratios and spins," *Phys. Rev. D*, vol. 93, no. 6, p. 064 041, 2016. arXiv: 1512.02248 [gr-qc].

[20] C. Capano, I. Harry, S. Privitera, and A. Buonanno, "Implementing a search for gravitational waves from binary black holes with nonprecessing spin," *Phys. Rev. D*, vol. 93, no. 12, p. 124 007, 2016. arXiv: 1602.03509 [gr-qc].

[21] M. van de Meent and H. P. Pfeiffer, "Intermediate mass-ratio black hole binaries: Applicability of small mass-ratio perturbation theory," Jun. 2020. arXiv: 2006.12036 [gr-qc].

[22] A. Buonanno, B. Iyer, E. Ochsner, Y. Pan, and B. Sathyaprakash, "Comparison of post-Newtonian templates for compact binary inspiral signals in gravitational-wave detectors," *Phys. Rev. D*, vol. 80, p. 084 043, 2009. arXiv: 0907.0700 [gr-qc].

[23] B. Abbott *et al.*, "GWTC-1: A Gravitational-Wave Transient Catalog of Compact Binary Mergers Observed by LIGO and Virgo during the First and Second Observing Runs," *Phys. Rev. X*, vol. 9, no. 3, p. 031 040, 2019. arXiv: 1811.12907 [astro-ph.HE].

[24] A. Nitz, I. Harry, D. Brown, C. M. Biwer, J. Willis, T. D. Canton, C. Capano, L. Pekowsky, T. Dent, A. R. Williamson, S. De, G. Davies, M. Cabero, D. Macleod, B. Machenschalk, S. Reyes, P. Kumar, T. Massinger, F. Pannarale, dfinstad, M. Tápai, S. Fairhurst, S. Khan, L. Singer, S. Kumar, A. Nielsen, shasvath, idorrington92, A. Lenon, and H. Gabbard, *Gwastro/pycbc: Pycbc release v1.15.4*, version v1.15.4, Jan. 2020.

[25] T. Dal Canton, A. H. Nitz, A. P. Lundgren, A. B. Nielsen, D. A. Brown, T. Dent, I. W. Harry, B. Krishnan, A. J. Miller, K. Wette, K. Wiesner, and J. L. Willis, "Implementing a search for aligned-spin neutron star-black hole systems with advanced ground based gravitational wave detectors," *Phys. Rev. D*, vol. 90, p. 082 004, 8 2014.

[26] S. A. Usman *et al.*, "The PyCBC search for gravitational waves from compact binary coalescence," *Class. Quant. Grav.*, vol. 33, no. 21, p. 215 004, 2016. arXiv: 1508.02357 [gr-qc].

[27] B. Allen, W. G. Anderson, P. R. Brady, D. A. Brown, and J. D. Creighton, "FINDCHIRP: An Algorithm for detection of gravitational waves from inspiraling compact binaries," *Phys. Rev. D*, vol. 85, p. 122 006, 2012. arXiv: gr-qc/0509116.

[28] K. Cannon *et al.*, "Toward Early-Warning Detection of Gravitational Waves from Compact Binary Coalescence," *Astrophys. J.*, vol. 748, p. 136, 2012. arXiv: 1107.2665 [astro-ph.IM].

[29] S. Privitera, S. R. Mohapatra, P. Ajith, K. Cannon, N. Fotopoulos, M. A. Frei, C. Hanna, A. J. Weinstein, and J. T. Whelan, "Improving the sensitivity of a search for coalescing binary black holes with nonprecessing spins in gravitational wave data," *Phys. Rev. D*, vol. 89, no. 2, p. 024 003, 2014. arXiv: 1310.5633 [gr-qc].

[30] C. Messick, K. Blackburn, P. Brady, P. Brockill, K. Cannon, R. Cariou, S. Caudill, S. J. Chamberlin, J. D. Creighton, R. Everett, and et al., "Analysis framework for the prompt discovery of compact binary mergers in gravitational-wave data," *Physical Review D*, vol. 95, no. 4, 2017.

[31] LIGO Scientific Collaboration, *LIGO Algorithm Library - LALSuite*, free software (GPL), 2018.

[32] S. Sachdev *et al.*, "The GstLAL Search Analysis Methods for Compact Binary Mergers in Advanced LIGO's Second and Advanced Virgo's First Observing Runs," Jan. 2019. arXiv: 1901.08580 [gr-qc].

[33] J. Lange, R. O'Shaughnessy, and M. Rizzo, *Rapid and accurate parameter inference for coalescing, precessing compact binaries*, 2018. arXiv: 1805.10457 [gr-qc].

[34] C. Pankow, P. Brady, E. Ochsner, and R. O'Shaughnessy, "Novel scheme for rapid parallel parameter estimation of gravitational waves from compact binary coalescences," *Phys. Rev. D*, vol. 92, no. 2, p. 023 002, 2015. arXiv: 1502.04370 [gr-qc].

[35] C. E. Rasmussen and C. K. I. Williams, *Gaussian Processes for Machine Learning (Adaptive Computation and Machine Learning)*. The MIT Press, 2005, ISBN: 026218253X.

[36] B. P. Abbott *et al.*, "All-sky search for short gravitational-wave bursts in the first Advanced LIGO run," *Phys. Rev. D*, vol. 95, no. 4, p. 042 003, 2017. arXiv: 1611.02972 [gr-qc].

[37] B. Abbott *et al.*, "All-Sky Search for Short Gravitational-Wave Bursts in the Second Advanced LIGO and Advanced Virgo Run," *Phys. Rev. D*, vol. 100, no. 2, p. 024 017, 2019. arXiv: 1905.03457 [gr-qc].

[38] S. Klimenko *et al.*, "Method for detection and reconstruction of gravitational wave transients with networks of advanced detectors," *Phys. Rev. D*, vol. 93, no. 4, p. 042 004, 2016. arXiv: 1511.05999 [gr-qc].

[39] S. Klimenko, I. Yakushin, A. Mercer, and G. Mitselmakher, "Coherent method for detection of gravitational wave bursts," *Class. Quant. Grav.*, vol. 25, S. M. Scott and D. E. McClelland, Eds., p. 114 029, 2008. arXiv: 0802.3232 [gr-qc].

[40] B. Abbott *et al.*, "Observing gravitational-wave transient GW150914 with minimal assumptions," *Phys. Rev. D*, vol. 93, no. 12, p. 122 004, 2016, [Addendum: Phys.Rev.D 94, 069903 (2016)]. arXiv: 1602.03843 [gr-qc].

[41] R. Lynch, S. Vitale, R. Essick, E. Katsavounidis, and F. Robinet, "Information-theoretic approach to the gravitational-wave burst detection problem," *Phys. Rev. D*, vol. 95, no. 10, p. 104 046, 2017. arXiv: 1511.05955 [gr-qc].

[42] N. J. Cornish and T. B. Littenberg, "BayesWave: Bayesian Inference for Gravitational Wave Bursts and Instrument Glitches," *Class. Quant. Grav.*, vol. 32, no. 13, p. 135 012, 2015. arXiv: 1410.3835 [gr-qc].

[43] T. B. Littenberg and N. J. Cornish, "Bayesian inference for spectral estimation of gravitational wave detector noise," *Phys. Rev. D*, vol. 91, no. 8, p. 084 034, 2015. arXiv: 1410.3852 [gr-qc].

[44] K. A. Arnaud *et al.*, "The Mock LISA Data Challenges: An overview," *AIP Conf. Proc.*, vol. 873, no. 1, pp. 619–624, 2006. arXiv: gr-qc/0609105 [gr-qc].

[45] S. Babak *et al.*, "Report on the second Mock LISA Data Challenge," *Class. Quant. Grav.*, vol. 25, S. M. Scott and D. E. McClelland, Eds., p. 114 037, 2008. arXiv: 0711.2667 [gr-qc].

[46] E. K. Porter, "An Overview of LISA Data Analysis Algorithms," Oct. 2009. arXiv: 0910.0373 [gr-qc].

[47] T. Robson and N. Cornish, "Impact of galactic foreground characterization on a global analysis for the LISA gravitational wave observatory," *Class. Quant. Grav.*, vol. 34, no. 24, p. 244 002, 2017. arXiv: 1705.09421 [gr-qc].

[48] T. Littenberg, N. Cornish, K. Lackeos, and T. Robson, "Global Analysis of the Gravitational Wave Signal from Galactic Binaries," *Phys. Rev. D*, vol. 101, no. 12, p. 123 021, 2020. arXiv: 2004.08464 [gr-qc].

[49] N. J. Cornish and E. K. Porter, "The Search for supermassive black hole binaries with LISA," *Class. Quant. Grav.*, vol. 24, pp. 5729–5755, 2007. arXiv: gr-qc/0612091.

[50] J. R. Gair, E. K. Porter, S. Babak, and L. Barack, "A Constrained Metropolis-Hastings Search for EMRIs in the Mock LISA Data Challenge 1B," *Class. Quant.*

Grav., vol. 25, S. Hughes and E. Katsavounidis, Eds., p. 184 030, 2008. arXiv: 0804.3322 [gr-qc].

[51] F. Feroz, M. Hobson, and M. Bridges, "MultiNest: an efficient and robust Bayesian inference tool for cosmology and particle physics," *Mon. Not. Roy. Astron. Soc.*, vol. 398, pp. 1601–1614, 2009. arXiv: 0809.3437 [astro-ph].

[52] K. Schwarzschild, "On the gravitational field of a mass point according to Einstein's theory," *Sitzungsber. Preuss. Akad. Wiss. Berlin (Math. Phys.)*, vol. 1916, pp. 189–196, 1916. arXiv: physics/9905030 [physics].

[53] H. Reissner, "Über die eigengravitation des elektrischen feldes nach der einsteinschen theorie," *Annalen der Physik*, vol. 355, no. 9, pp. 106–120, 1916. eprint: https://onlinelibrary.wiley.com/doi/pdf/10.1002/andp.19163550905.

[54] G. Nordström, "On the Energy of the Gravitation field in Einstein's Theory," *Koninklijke Nederlandse Akademie van Wetenschappen Proceedings Series B Physical Sciences*, vol. 20, pp. 1238–1245, 1918.

[55] R. P. Kerr, "Gravitational field of a spinning mass as an example of algebraically special metrics," *Phys. Rev. Lett.*, vol. 11, pp. 237–238, 5 1963.

[56] E. T. Newman, E. Couch, K. Chinnapared, A. Exton, A. Prakash, and R. Torrence, "Metric of a rotating, charged mass," *Journal of Mathematical Physics*, vol. 6, no. 6, pp. 918–919, 1965. eprint: https://doi.org/10.1063/1.1704351.

[57] R. L. Arnowitt, S. Deser, and C. W. Misner, "The Dynamics of general relativity," *Gen. Rel. Grav.*, vol. 40, pp. 1997–2027, 2008. arXiv: gr-qc/0405109 [gr-qc].

[58] T. Nakamura, K. Oohara, and Y. Kojima, "General Relativistic Collapse to Black Holes and Gravitational Waves from Black Holes," *Progress of Theoretical Physics Supplement*, vol. 90, pp. 1–218, Jan. 1987. eprint: http://oup.prod.sis.lan/ptps/article-pdf/doi/10.1143/PTPS.90.1/5201911/90-1.pdf.

[59] M. Shibata and T. Nakamura, "Evolution of three-dimensional gravitational waves: Harmonic slicing case," *Phys. Rev. D*, vol. 52, pp. 5428–5444, 10 1995.

[60] T. W. Baumgarte and S. L. Shapiro, "Numerical integration of einstein's field equations," *Phys. Rev. D*, vol. 59, p. 024 007, 2 1998.

[61] ——, "On the numerical integration of Einstein's field equations," *Phys. Rev. D*, vol. 59, p. 024 007, 1999. arXiv: gr-qc/9810065.

[62] L. Smarr, "Gravitational radiation from distant encounters and from head-on collisions of black holes: The zero-frequency limit," *Phys. Rev. D*, vol. 15, pp. 2069–2077, 8 1977.

[63] P. Laguna and D. Shoemaker, "Numerical stability of a new conformal-traceless 3 $plus$ 1 formulation of the einstein equation," *Classical and Quantum Gravity*, vol. 19, no. 14, pp. 3679–3686, 2002.

[64] W. Tichy, B. Bruegmann, and P. Laguna, "Gauge conditions for binary black hole puncture data based on an approximate helical Killing vector," *Phys. Rev. D*, vol. 68, p. 064 008, 2003. arXiv: gr-qc/0306020.

[65] M. Campanelli, C. Lousto, P. Marronetti, and Y. Zlochower, "Accurate evolutions of orbiting black-hole binaries without excision," *Phys. Rev. Lett.*, vol. 96, p. 111 101, 2006. arXiv: gr-qc/0511048.

[66] J. G. Baker, J. Centrella, D.-I. Choi, M. Koppitz, and J. van Meter, "Gravitational wave extraction from an inspiraling configuration of merging black holes," *Phys. Rev. Lett.*, vol. 96, p. 111 102, 2006. arXiv: gr-qc/0511103 [gr-qc].

[67] F. Pretorius, "Numerical relativity using a generalized harmonic decomposition," *Class. Quant. Grav.*, vol. 22, pp. 425–452, 2005. arXiv: gr-qc/0407110.

[68] ——, "Evolution of binary black hole spacetimes," *Phys. Rev. Lett.*, vol. 95, p. 121 101, 2005. arXiv: gr-qc/0507014.

[69] L. E. Kidder, M. A. Scheel, S. A. Teukolsky, E. D. Carlson, and G. B. Cook, "Black hole evolution by spectral methods," *Phys. Rev. D*, vol. 62, p. 084 032, 2000. arXiv: gr-qc/0005056.

[70] M. Boyle, L. Lindblom, H. Pfeiffer, M. Scheel, and L. E. Kidder, "Testing the accuracy and stability of spectral methods in numerical relativity," *Phys. Rev. D*, vol. 75, p. 024 006, 2007. arXiv: gr-qc/0609047.

[71] M. A. Scheel, M. Boyle, T. Chu, L. E. Kidder, K. D. Matthews, and H. P. Pfeiffer, "High-accuracy waveforms for binary black hole inspiral, merger, and ringdown," *Phys. Rev. D*, vol. 79, p. 024 003, 2009. arXiv: 0810.1767 [gr-qc].

[72] F. Loffler *et al.*, "The Einstein Toolkit: A Community Computational Infrastructure for Relativistic Astrophysics," *Class. Quant. Grav.*, vol. 29, p. 115 001, 2012. arXiv: 1111.3344 [gr-qc].

[73] M. Ansorg, B. Bruegmann, and W. Tichy, "A Single-domain spectral method for black hole puncture data," *Phys. Rev.*, vol. D70, p. 064 011, 2004. arXiv: gr-qc/0404056 [gr-qc].

[74] E. Schnetter, S. H. Hawley, and I. Hawke, "Evolutions in 3-D numerical relativity using fixed mesh refinement," *Class. Quant. Grav.*, vol. 21, pp. 1465–1488, 2004. arXiv: gr-qc/0310042 [gr-qc].

[75] M. Berger and J. Oliger, "Adaptive mesh refinement for hyperbolic partial differential equations," *Journal of Computational Physics*, vol. 53, no. 3, pp. 484–512, Mar. 1984.

[76] M. Alcubierre, B. Bruegmann, P. Diener, M. Koppitz, D. Pollney, E. Seidel, and R. Takahashi, "Gauge conditions for long term numerical black hole evolutions without excision," *Phys. Rev. D*, vol. 67, p. 084 023, 2003. arXiv: gr-qc/0206072.

[77] C. Bona, J. Masso, E. Seidel, and J. Stela, "A New formalism for numerical relativity," *Phys. Rev. Lett.*, vol. 75, pp. 600–603, 1995. arXiv: gr-qc/9412071.

[78] M. Campanelli, C. O. Lousto, P. Marronetti, and Y. Zlochower, "Accurate evolutions of orbiting black-hole binaries without excision," *Phys. Rev. Lett.*, vol. 96, p. 111 101, 11 2006.

[79] E. Newman and R. Penrose, "Note on the Bondi-Metzner-Sachs group," *J. Math. Phys.*, vol. 7, pp. 863–870, 1966.

[80] J. Goldberg, A. MacFarlane, E. Newman, F. Rohrlich, and E. Sudarshan, "Spin s spherical harmonics and edth," *J. Math. Phys.*, vol. 8, p. 2155, 1967.

[81] H. Nakano, J. Healy, C. O. Lousto, and Y. Zlochower, "Perturbative extraction of gravitational waveforms generated with Numerical Relativity," *Phys. Rev. D*, vol. 91, no. 10, p. 104 022, 2015. arXiv: 1503.00718 [gr-qc].

[82] J. Thornburg, "A fast apparent horizon finder for three-dimensional cartesian grids in numerical relativity," *Classical and Quantum Gravity*, vol. 21, no. 2, pp. 743–766, 2003.

[83] P. Schmidt, I. W. Harry, and H. P. Pfeiffer, *Numerical relativity injection infrastructure*, 2017. arXiv: 1703.01076 [gr-qc].

[84] C. Evans, D. Ferguson, B. Khamesra, P. Laguna, and D. Shoemaker, "Inside the Final Black Hole: Puncture and Trapped Surface Dynamics," *Class. Quant. Grav.*, vol. 37, no. 15, 15LT02, 2020. arXiv: 2004.11979 [gr-qc].

[85] P. Ramachandran and G. Varoquaux, "Mayavi: 3D Visualization of Scientific Data," *Computing in Science & Engineering*, vol. 13, no. 2, pp. 40–51, 2011.

[86] L. S. Collaboration and V. Collaboration, "Observation of gravitational waves from a binary black hole merger," *Phys. Rev. Lett.*, vol. 116, p. 061 102, 6 2016.

[87] The LIGO Scientific Collaboration and The Virgo Collaboration, "Binary Black Hole Population Properties Inferred from the First and Second Observing Runs of Advanced LIGO and Advanced Virgo," *arXiv e-prints*, arXiv:1811.12940, arXiv:1811.12940, Nov. 2018. eprint: 1811.12940 (astro-ph.HE).

[88] R. Abbott *et al.*, "GWTC-2: Compact Binary Coalescences Observed by LIGO and Virgo During the First Half of the Third Observing Run," Oct. 2020. arXiv: 2010.14527 [gr-qc].

[89] C. V. Vishveshwara, "Stability of the schwarzschild metric," *Phys. Rev. D*, vol. 1, pp. 2870–2879, 10 1970.

[90] W. H. Press, "Long Wave Trains of Gravitational Waves from a Vibrating Black Hole," *ApJ Letters*, vol. 170, p. L105, Dec. 1971.

[91] H.-P. Nollert and R. H. Price, "Quantifying excitations of quasinormal mode systems," *Journal of Mathematical Physics*, vol. 40, pp. 980–1010, Feb. 1999. arXiv: gr-qc/9810074 [gr-qc].

[92] K. D. Kokkotas and B. G. Schmidt, "Quasi-Normal Modes of Stars and Black Holes," *Living Reviews in Relativity*, vol. 2, 2, p. 2, Sep. 1999. arXiv: gr-qc/9909058 [gr-qc].

[93] E. Berti, V. Cardoso, and A. O. Starinets, "TOPICAL REVIEW: Quasinormal modes of black holes and black branes," *Classical and Quantum Gravity*, vol. 26, 163001, p. 163 001, Aug. 2009. arXiv: 0905.2975 [gr-qc].

[94] F. Echeverria, "Gravitational-wave measurements of the mass and angular momentum of a black hole," *Phys. Rev. D*, vol. 40, pp. 3194–3203, 10 1989.

[95] O. Dreyer, B. J. Kelly, B. Krishnan, L. S. Finn, D. Garrison, and R. Lopez-Aleman, "Black hole spectroscopy: Testing general relativity through gravitational wave observations," *Class. Quant. Grav.*, vol. 21, pp. 787–804, 2004. arXiv: gr-qc/0309007 [gr-qc].

[96] E. Berti, V. Cardoso, and C. M. Will, "On gravitational-wave spectroscopy of massive black holes with the space interferometer LISA," *Phys. Rev.*, vol. D73, p. 064 030, 2006. arXiv: gr-qc/0512160 [gr-qc].

[97] R. Brito, A. Buonanno, and V. Raymond, "Black-hole spectroscopy by making full use of gravitational-wave modeling," *Phys. Rev. D*, vol. 98, p. 084 038, 8 2018.

[98] B. P. Abbott *et al.*, "Search for gravitational wave ringdowns from perturbed black holes in LIGO S4 data," *Phys. Rev.*, vol. D80, p. 062 001, 2009. arXiv: 0905.1654 [gr-qc].

[99] L. M. Goggin and the LIGO Scientific Collaboration, "Search for black hole ringdown signals in LIGO s4 data," *Classical and Quantum Gravity*, vol. 23, no. 19, S709–S713, 2006.

[100] E. Berti, J. Cardoso, V. Cardoso, and M. Cavaglia, "Matched-filtering and parameter estimation of ringdown waveforms," *Phys. Rev.*, vol. D76, p. 104 044, 2007. arXiv: 0707.1202 [gr-qc].

[101] G. Carullo, W. Del Pozzo, and J. Veitch, "Observational Black Hole Spectroscopy: A time-domain multimode analysis of GW150914," *arXiv:1902.07527*, 2019.

[102] H. Yang, K. Yagi, J. Blackman, L. Lehner, V. Paschalidis, F. Pretorius, and N. Yunes, "Black hole spectroscopy with coherent mode stacking," *Phys. Rev. Lett.*, vol. 118, p. 161 101, 16 2017.

[103] H. Nakano, T. Narikawa, K.-i. Oohara, K. Sakai, H.-a. Shinkai, H. Takahashi, T. Tanaka, N. Uchikata, S. Yamamoto, and T. S. Yamamoto, "Comparison of various methods to extract ringdown frequency from gravitational wave data," 2018. arXiv: 1811.06443 [gr-qc].

[104] M. Cabero, C. D. Capano, O. Fischer-Birnholtz, B. Krishnan, A. B. Nielsen, A. H. Nitz, and C. M. Biwer, "Observational tests of the black hole area increase law," *Phys. Rev. D*, vol. 97, p. 124 069, 12 2018.

[105] S. Bhagwat, M. Okounkova, S. W. Ballmer, D. A. Brown, M. Giesler, M. A. Scheel, and S. A. Teukolsky, "On choosing the start time of binary black hole ringdowns," *Phys. Rev.*, vol. D97, no. 10, p. 104 065, 2018. arXiv: 1711.00926 [gr-qc].

[106] G. Carullo, L. van der Schaaf, L. London, P. T. H. Pang, K. W. Tsang, O. A. Hannuksela, J. Meidam, M. Agathos, A. Samajdar, A. Ghosh, T. G. F. Li, W. Del Pozzo, and C. Van Den Broeck, "Empirical tests of the black hole no-hair conjecture using gravitational-wave observations," *Phys. Rev. D*, vol. 98, p. 104 020, 10 2018.

[107] B. P. Abbott *et al.*, "Tests of general relativity with GW150914," *Phys. Rev. Lett.*, vol. 116, no. 22, p. 221 101, 2016, [Erratum: Phys. Rev. Lett.121,no.12,129902(2018)]. arXiv: 1602.03841 [gr-qc].

[108] J. Healy, C. O. Lousto, and Y. Zlochower, "Remnant mass, spin, and recoil from spin aligned black-hole binaries," *Phys. Rev.*, vol. D90, no. 10, p. 104 004, 2014. arXiv: 1406.7295 [gr-qc].

[109] L. Rezzolla, P. Diener, E. N. Dorband, D. Pollney, C. Reisswig, E. Schnetter, and J. Seiler, "The Final spin from the coalescence of aligned-spin black-hole binaries," *Astrophys. J.*, vol. 674, pp. L29–L32, 2008. arXiv: 0710.3345 [gr-qc].

[110] J. Healy and C. O. Lousto, "Remnant of binary black-hole mergers: New simulations and peak luminosity studies," *PRD*, vol. 95, no. 2, 024037, p. 024 037, Jan. 2017. arXiv: 1610.09713 [gr-qc].

[111] X. Jiménez-Forteza, D. Keitel, S. Husa, M. Hannam, S. Khan, and M. Pürrer, "Hierarchical data-driven approach to fitting numerical relativity data for nonprecessing binary black holes with an application to final spin and radiated energy," *PRD*, vol. 95, no. 6, 064024, p. 064 024, Mar. 2017. arXiv: 1611.00332 [gr-qc].

[112] F. Hofmann, E. Barausse, and L. Rezzolla, "The Final Spin from Binary Black Holes in Quasi-circular Orbits," *ApJL*, vol. 825, L19, p. L19, Jul. 2016. arXiv: 1605.01938 [gr-qc].

[113] B. P. Abbott *et al.*, "Tests of General Relativity with the Binary Black Hole Signals from the LIGO-Virgo Catalog GWTC-1," 2019. arXiv: 1903.04467 [gr-qc].

[114] A. Ghosh, N. K. Johnson-Mcdaniel, A. Ghosh, C. K. Mishra, P. Ajith, W. Del Pozzo, C. P. L. Berry, A. B. Nielsen, and L. London, "Testing general relativity using gravitational wave signals from the inspiral, merger and ringdown of binary black holes," *Class. Quant. Grav.*, vol. 35, no. 1, p. 014 002, 2018. arXiv: 1704.06784 [gr-qc].

[115] A. Ghosh *et al.*, "Testing general relativity using golden black-hole binaries," *Phys. Rev.*, vol. D94, no. 2, p. 021 101, 2016. arXiv: 1602.02453 [gr-qc].

[116] G. Carullo, G. Riemenschneider, K. W. Tsang, A. Nagar, and W. Del Pozzo, "GW150914 peak frequency: a novel consistency test of strong-field General Relativity," *Class. Quant. Grav.*, vol. 36, no. 10, p. 105 009, 2019. arXiv: 1811.08744 [gr-qc].

[117] J. Healy, P. Laguna, and D. Shoemaker, "Decoding the final state in binary black hole mergers," *Classical and Quantum Gravity*, vol. 31, no. 21, 212001, p. 212 001, Nov. 2014. arXiv: 1407.5989 [gr-qc].

[118] A. Buonanno, G. B. Cook, and F. Pretorius, "Inspiral, merger and ring-down of equal-mass black-hole binaries," *Phys. Rev.*, vol. D75, p. 124 018, 2007. arXiv: gr-qc/0610122 [gr-qc].

[119] I. Kamaretsos, M. Hannam, and B. S. Sathyaprakash, "Is black-hole ringdown a memory of its progenitor?" *Phys. Rev. Lett.*, vol. 109, p. 141 102, 14 2012.

[120] M. Giesler, M. Isi, M. Scheel, and S. Teukolsky, "Black hole ringdown: the importance of overtones," 2019. arXiv: 1903.08284 [gr-qc].

[121] V. Tiwari, S. Klimenko, V. Necula, and G. Mitselmakher, "Reconstruction of chirp mass in searches for gravitational wave transients," *Class. Quant. Grav.*, vol. 33, no. 1, 01LT01, 2016. arXiv: 1510.02426 [astro-ph.IM].

[122] D. Ferguson, S. Ghonge, J. A. Clark, J. Calderon Bustillo, P. Laguna, D. Shoemaker, and J. Calderon Bustillo, "Measuring Spin of the Remnant Black Hole from Maximum Amplitude," *Phys. Rev. Lett.*, vol. 123, no. 15, p. 151 101, 2019. arXiv: 1905.03756 [gr-qc].

[123] K. Jani, J. Healy, J. A. Clark, L. London, P. Laguna, and D. Shoemaker, "Georgia tech catalog of gravitational waveforms," *Classical and Quantum Gravity*, vol. 33, no. 20, 204001, p. 204 001, Oct. 2016. arXiv: 1605.03204 [gr-qc].

[124] J. Calderón Bustillo, P. Laguna, and D. Shoemaker, "Detectability of gravitational waves from binary black holes: Impact of precession and higher modes," *Phys. Rev.*, vol. D95, no. 10, p. 104 038, 2017. arXiv: 1612.02340 [gr-qc].

[125] J. Calderón Bustillo, S. Husa, A. M. Sintes, and M. Pürrer, "Impact of gravitational radiation higher order modes on single aligned-spin gravitational wave searches for binary black holes," *Phys. Rev.*, vol. D93, no. 8, p. 084 019, 2016. arXiv: 1511.02060 [gr-qc].

[126] L. Pekowsky, J. Healy, D. Shoemaker, and P. Laguna, "Impact of higher-order modes on the detection of binary black hole coalescences," *Phys. Rev.*, vol. D87, no. 8, p. 084 008, 2013. arXiv: 1210.1891 [gr-qc].

[127] V. Varma and P. Ajith, "Effects of nonquadrupole modes in the detection and parameter estimation of black hole binaries with nonprecessing spins," *Phys. Rev.*, vol. D96, no. 12, p. 124 024, 2017. arXiv: 1612.05608 [gr-qc].

[128] M. Vallisneri, "Use and abuse of the Fisher information matrix in the assessment of gravitational-wave parameter-estimation prospects," *Phys. Rev.*, vol. D77, p. 042 001, 2008. arXiv: gr-qc/0703086 [GR-QC].

[129] J. Veitch, V. Raymond, B. Farr, W Farr, P. Graff, S. Vitale, B. Aylott, K. Blackburn, N. Christensen, M. Coughlin, *et al.*, "Parameter estimation for compact binaries with ground-based gravitational-wave observations using the lalinference software library," *Physical Review D*, vol. 91, no. 4, p. 042 003, 2015.

[130] C. Messick, K. Blackburn, P. Brady, P. Brockill, K. Cannon, R. Cariou, S. Caudill, S. J. Chamberlin, J. D. E. Creighton, R. Everett, C. Hanna, D. Keppel, R. N. Lang, T. G. F. Li, D. Meacher, A. Nielsen, C. Pankow, S. Privitera, H. Qi, S. Sachdev, L. Sadeghian, L. Singer, E. G. Thomas, L. Wade, M. Wade, A. Weinstein, and K. Wiesner, "Analysis framework for the prompt discovery of compact binary mergers

in gravitational-wave data," **??***jnlPhRvD*, vol. 95, 042001, p. 042 001, 2017. arXiv: 1604.04324 [astro-ph.IM].

[131] E. Parzen, "Review of 'extraction of signals from noise' (wainstein, l. a., and zubakov, v. d.; 1962)," *IEEE Trans. Inf. Theor.*, vol. 9, no. 2, pp. 127–127, Sep. 2006.

[132] N. E. Huang, Z. Shen, S. R. Long, M. C. Wu, H. H. Shih, Q. Zheng, N.-C. Yen, C. C. Tung, and H. H. Liu, "The empirical mode decomposition and the hilbert spectrum for nonlinear and non-stationary time series analysis," *Proceedings of the Royal Society of London. Series A: Mathematical, Physical and Engineering Sciences*, vol. 454, no. 1971, pp. 903–995, 1998. eprint: https://royalsocietypublishing.org/doi/pdf/10.1098/rspa.1998.0193.

[133] B. Abbott *et al.*, "GW170817: Observation of Gravitational Waves from a Binary Neutron Star Inspiral," *Phys. Rev. Lett.*, vol. 119, no. 16, p. 161 101, 2017. arXiv: 1710.05832 [gr-qc].

[134] ——, "GW190425: Observation of a Compact Binary Coalescence with Total Mass $\sim 3.4 M_{\odot}$," *Astrophys. J. Lett.*, vol. 892, no. 1, p. L3, 2020. arXiv: 2001.01761 [astro-ph.HE].

[135] M. Shibata, S. Fujibayashi, K. Hotokezaka, K. Kiuchi, K. Kyutoku, Y. Sekiguchi, and M. Tanaka, "Modeling GW170817 based on numerical relativity and its implications," *Phys. Rev. D*, vol. 96, no. 12, p. 123 012, 2017. arXiv: 1710.07579 [astro-ph.HE].

[136] M. Hannam, P. Schmidt, A. Bohé, L. Haegel, S. Husa, F. Ohme, G. Pratten, and M. Pürrer, "Simple Model of Complete Precessing Black-Hole-Binary Gravitational Waveforms," *Phys. Rev. Lett.*, vol. 113, no. 15, p. 151 101, 2014. arXiv: 1308.3271 [gr-qc].

[137] A. Bohé *et al.*, "Improved effective-one-body model of spinning, nonprecessing binary black holes for the era of gravitational-wave astrophysics with advanced detectors," *Phys. Rev. D*, vol. 95, no. 4, p. 044 028, 2017. arXiv: 1611.03703 [gr-qc].

[138] S. Khan, S. Husa, M. Hannam, F. Ohme, M. Pürrer, X. Jiménez Forteza, and A. Bohé, "Frequency-domain gravitational waves from nonprecessing black-hole binaries. II. A phenomenological model for the advanced detector era," *Phys. Rev. D*, vol. 93, no. 4, p. 044 007, 2016. arXiv: 1508.07253 [gr-qc].

[139] J. Blackman, S. E. Field, M. A. Scheel, C. R. Galley, C. D. Ott, M. Boyle, L. E. Kidder, H. P. Pfeiffer, and B. Szilágyi, "Numerical relativity waveform surrogate

model for generically precessing binary black hole mergers," *Phys. Rev. D*, vol. 96, no. 2, p. 024 058, 2017. arXiv: 1705.07089 [gr-qc].

[140] S. Husa, S. Khan, M. Hannam, M. Pürrer, F. Ohme, X. Jiménez Forteza, and A. Bohé, "Frequency-domain gravitational waves from nonprecessing black-hole binaries. I. New numerical waveforms and anatomy of the signal," *Phys. Rev. D*, vol. 93, no. 4, p. 044 006, 2016. arXiv: 1508.07250 [gr-qc].

[141] J. Lange *et al.*, "Parameter estimation method that directly compares gravitational wave observations to numerical relativity," *Phys. Rev. D*, vol. 96, no. 10, p. 104 041, 2017. arXiv: 1705.09833 [gr-qc].

[142] P. Schmidt, I. W. Harry, and H. P. Pfeiffer, "Numerical Relativity Injection Infrastructure," 2017. arXiv: 1703.01076 [gr-qc].

[143] V. Nedora, S. Bernuzzi, D. Radice, B. Daszuta, A. Endrizzi, A. Perego, A. Prakash, M. Safarzadeh, F. Schianchi, and D. Logoteta, "Numerical Relativity Simulations of the Neutron Star Merger GW170817: Long-Term Remnant Evolutions, Winds, Remnant Disks, and Nucleosynthesis," Aug. 2020. arXiv: 2008.04333 [astro-ph.HE].

[144] T. Robson, N. J. Cornish, and C. Liu, "The construction and use of lisa sensitivity curves," *Classical and Quantum Gravity*, vol. 36, no. 10, p. 105 011, 2019.

[145] Abbott, B. P. *et al.*, "Prospects for Observing and Localizing Gravitational-Wave Transients with Advanced LIGO, Advanced Virgo and KAGRA," *Living Rev. Rel.*, vol. 21, no. 1, p. 3, 2018. arXiv: 1304.0670 [gr-qc].

[146] D. Reitze *et al.*, "Cosmic Explorer: The U.S. Contribution to Gravitational-Wave Astronomy beyond LIGO," *Bull. Am. Astron. Soc.*, vol. 51, p. 035, Jul. 2019. arXiv: 1907.04833 [astro-ph.IM].

[147] S. Dwyer, D. Sigg, S. W. Ballmer, L. Barsotti, N. Mavalvala, and M. Evans, "Gravitational wave detector with cosmological reach," *Phys. Rev. D*, vol. 91, p. 082 001, 8 2015.

[148] P. A. Seoane *et al.*, "The Gravitational Universe," 2013. arXiv: 1305.5720 [astro-ph.CO].

[149] L. Lindblom, B. J. Owen, and D. A. Brown, "Model Waveform Accuracy Standards for Gravitational Wave Data Analysis," *Phys. Rev.*, vol. D78, p. 124 020, 2008. arXiv: 0809.3844 [gr-qc].

[150] L. Lindblom, "Use and Abuse of the Model Waveform Accuracy Standards," *Phys. Rev.*, vol. D80, p. 064 019, 2009. arXiv: 0907.0457 [gr-qc].

[151] I. Hinder *et al.*, "Error-analysis and comparison to analytical models of numerical waveforms produced by the NRAR Collaboration," *Class. Quant. Grav.*, vol. 31, p. 025 012, 2014. arXiv: 1307.5307 [gr-qc].

[152] E. E. Flanagan and S. A. Hughes, "Measuring gravitational waves from binary black hole coalescences: 2. The Waves' information and its extraction, with and without templates," *Phys. Rev.*, vol. D57, pp. 4566–4587, 1998. arXiv: gr-qc/9710129 [gr-qc].

[153] M. Miller, "Accuracy requirements for the calculation of gravitational waveforms from coalescing compact binaries in numerical relativity," *Phys. Rev. D*, vol. 71, p. 104 016, 10 2005.

[154] M. Pürrer and C.-J. Haster, "Ready for what lies ahead? – Gravitational waveform accuracy requirements for future ground based detectors," *Phys. Rev. Res.*, vol. 2, no. 2, p. 023 151, 2020. arXiv: 1912.10055 [gr-qc].

[155] K. Jani, J. Healy, J. A. Clark, L. London, P. Laguna, and D. Shoemaker, "Georgia Tech Catalog of Gravitational Waveforms," *Class. Quant. Grav.*, vol. 33, no. 20, p. 204 001, 2016. arXiv: 1605.03204 [gr-qc].

[156] F. Herrmann, I. Hinder, D. Shoemaker, and P. Laguna, "Unequal mass binary black hole plunges and gravitational recoil," *Classical and Quantum Gravity*, vol. 24, S33–S42, Jun. 2007. arXiv: gr-qc/0601026 [gr-qc].

[157] B. Vaishnav, I. Hinder, F. Herrmann, and D. Shoemaker, "Matched filtering of numerical relativity templates of spinning binary black holes," **??***jnlPhRvD*, vol. 76, 084020, p. 084 020, Oct. 2007. arXiv: 0705.3829 [gr-qc].

[158] J. Healy, J. Levin, and D. Shoemaker, "Zoom-whirl orbits in black hole binaries," *Phys. Rev. Lett.*, vol. 103, p. 131 101, 13 2009.

[159] L. Pekowsky, R. O'Shaughnessy, J. Healy, and D. Shoemaker, "Comparing gravitational waves from nonprecessing and precessing black hole binaries in the corotating frame," *Phys. Rev. D*, vol. 88, p. 024 040, 2 2013.

[160] K. Higginbotham, B. Khamesra, J. P. McInerney, K. Jani, D. M. Shoemaker, and P. Laguna, "Coping with spurious radiation in binary black hole simulations," *Phys. Rev. D*, vol. 100, p. 081 501, 8 2019.

[161] P. Ajith *et al.*, "The NINJA-2 catalog of hybrid post-Newtonian/numerical-relativity waveforms for non-precessing black-hole binaries," *Class. Quant. Grav.*, vol. 29, M. Hannam, P. Sutton, S. Hild, and C. van den Broeck, Eds., p. 124 001, 2012, [Erratum: Class.Quant.Grav. 30, 199401 (2013)]. arXiv: 1201.5319 [gr-qc].

[162] L. F. Richardson and R. T. Glazebrook, "On the approximate arithmetical solution by finite differences of physical problems involving differential equations, with an application to the stresses in a masonry dam," *Proceedings of the Royal Society of London. Series A, Containing Papers of a Mathematical and Physical Character*, vol. 83, no. 563, pp. 335–336, 1910.

[163] B. Vaishnav, I. Hinder, F. Herrmann, and D. Shoemaker, "Matched filtering of numerical relativity templates of spinning binary black holes," *Phys. Rev. D*, vol. 76, p. 084 020, 2007. arXiv: 0705.3829 [gr-qc].

[164] D. Ferguson, K. Jani, P. Laguna, and D. Shoemaker, "Assessing the Readiness of Numerical Relativity for LISA and 3G Detectors," Jun. 2020. arXiv: 2006.04272 [gr-qc].

[165] G. A. Piovano, A. Maselli, and P. Pani, "Extreme mass ratio inspirals with spinning secondary: a detailed study of equatorial circular motion," *Phys. Rev. D*, vol. 102, no. 2, p. 024 041, 2020. arXiv: 2004.02654 [gr-qc].

[166] M. Abadi, A. Agarwal, P. Barham, E. Brevdo, Z. Chen, C. Citro, G. S. Corrado, A. Davis, J. Dean, M. Devin, S. Ghemawat, I. Goodfellow, A. Harp, G. Irving, M. Isard, Y. Jia, R. Jozefowicz, L. Kaiser, M. Kudlur, J. Levenberg, D. Mané, R. Monga, S. Moore, D. Murray, C. Olah, M. Schuster, J. Shlens, B. Steiner, I. Sutskever, K. Talwar, P. Tucker, V. Vanhoucke, V. Vasudevan, F. Viégas, O. Vinyals, P. Warden, M. Wattenberg, M. Wicke, Y. Yu, and X. Zheng, *TensorFlow: Large-scale machine learning on heterogeneous systems*, Software available from tensorflow.org, 2015.

VITA

Deborah Ferguson was born in Bloemfontein, South Africa on May 7, 1995. She spent her early years in Peshawar, Pakistan, before moving to Lexington, KY in 2001, where she remained through college. She was awarded the Singletary Scholarship from the University of Kentucky, where she engaged in several undergraduate research projects, one of which resulted in a paper. She graduated summa cum laude in 2016 as outstanding physics senior, with a Bachelor of Science degree in Physics and minors in Mathematics and Computer Science. She received the Georgia Tech Institute Fellowship, and pursued her PhD at Georgia Tech under the guidance of Deirdre Shoemaker. Her studies focused on utilizing numerical relativity in tandem with gravitational wave data to study strong field gravity. During her time at Georgia Tech, she was awarded the Amelio Award for Research Excellence and the Larry S. O'Hara Graduate Student Fellowship. She was also granted the opportunity to attend the 69th Lindau Nobel Laureate Meeting.

1. D. Ferguson, S. Gardner, and B. Yanny, "Milky Way Tomography with K and M Dwarf Stars: The Vertical Structure of the Galactic Disk," Astrophysical Journal, vol. 843, no. 2, 141, p. 141, Jul. 2017. arXiv: 1706.01900 [astro-ph.GA].

2. D. Ferguson, S. Ghonge, J. A. Clark, J. Calderon Bustillo, P. Laguna, D. Shoemaker, and J. Calderon Bustillo, "Measuring Spin of the Remnant Black Hole from Maximum Amplitude," Phys. Rev. Lett., vol. 123, no. 15, p. 151 101, 2019. arXiv: 1905.03756 [gr-qc].

3. D. Ferguson, K. Jani, P. Laguna, and D. Shoemaker, "Assessing the Readiness of Numerical Relativity for LISA and 3G Detectors," Jun. 2020. arXiv: 2006.04272 [gr-qc] (submitted).